

PhD 2005:64

Arne Fredheim

Current Forces on Net Structures

Universitetsbiblioteket i Trondheim
Teknisk hovedbibliotek
Trondheim

Trondheim, April 2005

Doctoral thesis for the degree of doktor ingeniør

Norwegian University of Science and Technology
Faculty of Engineering Science and Technology
Department of Marine Technology

 NTNU

Abstract

The trend in recent years has been that the amount of wild catch is stagnating. In this perspective the selectivity of fishing gear has become an important issue. The aim of the present work has been to develop a three-dimensional model for the flow in front and inside a net structure, such as a trawl, to be able to predict and calculate selectivity of net structures. A net consist of twines which connect in knots and make up a mesh. The diameter of a twine can be from 1 [mm] in net cages up to a few centimeters in the front part of a trawl. And similar the size of the mesh can be from 1 [cm] up to the order of a meter. Typical Reynolds number range, related to the diameter of a twine, is $O(10^2 - 10^4)$.

An examination of numerical results for the drag force on plane net structure demonstrates a strong dependency of the drag force on a net structure with both the geometry, in terms of Solidity ratio, and the Reynolds number. And in particular a non-uniform relation between the drag force and the Solidity ratio. It is evident that for increasing Solidity ratios, flow interaction will become increasingly significant. The physical design of the knot part contributes largely to this flow interaction.

The net structure is divided into discrete elements. The twines are modeled as separate cylinders between knots and the knots are modeled as separate spheres. Typically the total number of twines in a trawl could be in the order of 10^6 and it is thus impractical to model every single twine. It is assumed that for a given Reynolds number, keeping the Solidity ratio constant, the total drag on the trawl will be independent on the actual diameter and mesh opening of the net.

First each of these different elements is modeled as a set of source distributions and single point sources. The influence from the net on the fluid flow is then calculated by representing the wake generated by each element as source distributions along the structural element. To determine the strength of these sources the principle of Lagally is applied. Then a set

of equations is obtained, describing the relation between the fluid velocity and the source strength at every element. Based on this approach, a method is presented to calculate the drag force on net structures with high solidity. The method uses appropriate drag coefficients related to the geometry of the twines and the knots and account for the change in the inflow due to the presence of the net structure and at the same time changes the geometry of the net structure due to the load.

Secondly the interaction between the net elements, due to the physical generation of a wake flow behind each individual element of the net, has been studied using a time-averaged wake model. Modifications are applied to the far-field mean velocity deficit mode by Schlichting (1968). This to better describe the the near-field behavior and the added effect of the wake from many individual cylindrical elements. It is shown that the wake model by Blevins (1990) can be used. The method is verified against experiments, as means of calculating the drag on plane nets as a function of Reynolds number, Solidity ratio and angle of attack and gives reasonable good agreement. During the experiments some interesting three-dimensional effects regarding the flow around cylinders were discovered. Negative lift forces occurring on the downstream cylinder in a staggered arrangement is explained as interactions due to upstream generated vortices.

To create a three-dimensional method where the inflow on each of the cylinders is corrected due to the presence of all the other cylinders, these two models are added together. Further, a structural analysis of the net structure, using a FEM method, is included in the model. A more complete description of the problem is obtained by combining the change in the inflow due to the presence of the net structure, with a correction of the shape and geometry due to the drag load.

Results from numerical simulation of different kinds of net structures, show that the elasticity in the net structure has a significant influence on the resulting geometry and calculated results. Further, the numerical results for net cages have been compared to experimental results. Good agreement between the numerical results and the experimental result is seen. Also the resulting geometry from the experimental results was recreated satisfactory using the present method.

For three-dimensional cone shaped net structures, in contrast to net panels and net cages, the presented numerical results do not indicate a large influence on the drag force due to changes in geometry. The agreement between the numerical and experimental results for fluid velocity in front and inside of a three-dimensional net structure, compared to experimental results, was reasonably good. Quantitatively the results do not match exactly, but the characteristics of the flow are recreated. Further, based on the numerical results for the fluid velocity, pressure field in front of a cone is presented. The relative pressure gradient is shown to be minimal, and it is not likely than any fish will detect this change in pressure field neither by direct pressure sensing nor by any sound created from any shed vortices.

Acknowledgement

The current work has been carried out under supervision of Professor Odd M. Faltinsen at the Department of Marine Technology, the Norwegian University of Science and technology. I am grateful for his guidance and support and not at least his endurance to see this work through.

Geir Løland had the idea to the topic of this work and was co-supervising and getting the work on the right track the first years. I am thankful for him giving me the opportunity and for his contributions. I also want to thank a number of people, especially some of my colleagues at MARINTEK and SINTEF Fisheries and Aquaculture, which have contributed with constructive questions, fruitful discussions and interesting literature.

The last finalizing of this thesis has been inspired by several of my good colleagues, friends and not at least my family. Without their many questions about when and encouragement to (and the potential embarrassment of not), it is likely that this thesis would have never been finished.

This work has been financed by the research Council of Norway through their funding of the strategic research program “Hydrodynamical analysis of fishing tools and fish farming constructions” at MARINTEK.

Contents

1	Introduction	1
1.1	Background and motivation	1
1.2	Net structures	2
1.3	Analysis of a net structure	5
1.4	Modeling of a net structure	12
	1.4.1 Related work	12
	1.4.2 Present approach	15
1.5	Contributions	17
2	Modeling upstream effects	19
2.1	Introduction	19
2.2	Disturbance potential	20
2.3	Equation system	21
2.4	Velocities	23
2.5	Numerical solution procedure	24
2.6	Convergence	25
2.7	Non-discrete modeling	27
2.8	Verification of the upstream model	30
	2.8.1 Numerical analysis	30
	2.8.2 Results for plane nets at 90 [deg] angle of attack	31
	2.8.3 Results as a function of angle of attack	35
3	Modeling downstream effects	37
3.1	Introduction	37
	3.1.1 Forces on a circular cylinder	40
	3.1.2 The far wake mean velocity deficit model	42
3.2	Modified models	43
	3.2.1 Near field modification	43
	3.2.2 Virtual origin	44

3.2.3	Two dimensional plane wake	44
3.2.4	Virtual source position	45
3.2.5	Effect of the different models	46
3.3	Experiments	49
3.3.1	Introduction	49
3.3.2	Model setup	49
3.3.3	Discussion of the experimental results	54
3.3.4	Potential inaccuracies and errors in the experiment	60
3.3.5	Visualization	62
3.4	Drag on multiple cylinders	64
3.4.1	Added effect of several cylinders	64
3.4.2	Two cylinders	67
3.4.3	Five cylinders	69
3.4.4	Possible effects influencing the results	71
3.5	Lift on Multiple Cylinders	78
3.5.1	Introduction	78
3.5.2	Flow visualization	79
3.5.3	Results	79
4	Three Dimensional Net Structures	85
4.1	Modeling of complete structures	85
4.1.1	Introduction	85
4.1.2	General modeling	86
4.1.3	Structural modeling	87
4.2	Plane nets with elasticity	89
4.3	Net cages	91
4.3.1	Net cage elasticity and bottom weight	93
4.3.2	Experimental results	99
4.4	Cone structures	103
4.4.1	Structural analysis and end force	103
4.4.2	Drag force	104
4.4.3	Fluid velocity inside a three-dimensional net structure	106
4.4.4	Pressure field in front of a three-dimensional net structure	110
4.4.5	Other aspects related to net structures	112
5	Conclusions and Further work	113
A	Additional results from wake experiments	121
B	Description of North Sea Centre Flume Tank	129

Nomenclature

A	Enclosed area of a plane net
A_p	Projected area of a plane net
C_d	Drag coefficient
C_l	Lift coefficient
C_{dt}	Drag coefficient of twine/element
C_{dk}	Drag coefficient of knot/sphere
C_{dp}	Drag coefficient of a net based on the projected area A_p
C_{dnet}	Drag coefficient of a net
d	Diameter
d_t	Diameter of twine/element
d_k	Diameter of knot/sphere
D_1	The diameter at the front part of net panel
E_1	Hanging ratio in the cross wise direction
E_2	Hanging ratio in the longitudinal direction
f_v	Vortex shedding frequency
F_D	Drag force
F_{Dnet}	Drag force for a net
H	Heaviside function
k	Resistance coefficient
l	Length of twine element
l_m	Mesh opening
L	The length between the front and aft part of the net panel
N	Number of meshes in the longitudinal direction of a net panel
	Number of twines or cylinders
p	Pressure
q	Source strength
Q	Three-dimensional source strength
Rn	Reynolds number
s	Horizontal distance between two cylinder axis
Sn	Solidity ratio
T_1	Number of meshes at the front part of the net panel
u	Disturbance velocity or velocity in the wake
u_1	Velocity deficit
U_∞	Uniform undisturbed flow
\mathbf{u}	Disturbance velocity vector
\mathbf{U}	Velocity vector
$\overline{\mathbf{U}}$	Incoming free flow

α	Angle of attack
ϵ_0	Eddie viscosity
ϵ_τ	Virtual kinematic viscosity
Φ	Error function
2ϕ	The angle of the mesh opening of a net panel
ϕ	Velocity potential
κ	Pressure drop coefficient
λ	Half mesh size
ν	Viscosity
	$\nu = 1.14 \times 10^{-6} [m^2/s]$ for freshwater and temperature $T = 15^\circ C$.
	$\nu = 1.19 \times 10^{-6} [m^2/s]$ for saltwater and temperature $T = 15^\circ C$.
ρ	Density of water

CHAPTER 1

Introduction

1.1 Background and motivation

The resources of wild fish are limited. The trend in recent years has been that the amount of wild catch is stagnating. In this perspective the selectivity of fishing gear has become an important issue. The research so far has mainly focused on the testing of different sorting devices. Figure 1.1 illustrates a trawl with a sorting device mounted in the aft part. In addition, numerical models have been developed to study the shape and behavior of both trawls and purse seines. All of these numerical models known to the author are based on the assumption of undisturbed flow, both in front and inside the net structure. A three-dimensional net structure is however a highly flexible structure and the force acting on the structure due to the fluid flow will have an effect on the shape of the structure, and further will alter the influence of the net structure on the fluid flow.

The idea is that by knowing the flow field, it is possible to develop a method that can be used to predict and calculate selectivity of the net structure. Further, it could increase the understanding and knowledge related to selectivity of the fishing gear. The aim of the present work is to develop a three-dimensional model for the flow in front and inside a net structure, such as a trawl. The flow conditions behind the trawl are not considered.

The motivation for this work is three folded. The most obvious is to improve the input flow model for a structural analysis of a net structure to account for the effect of the trawl

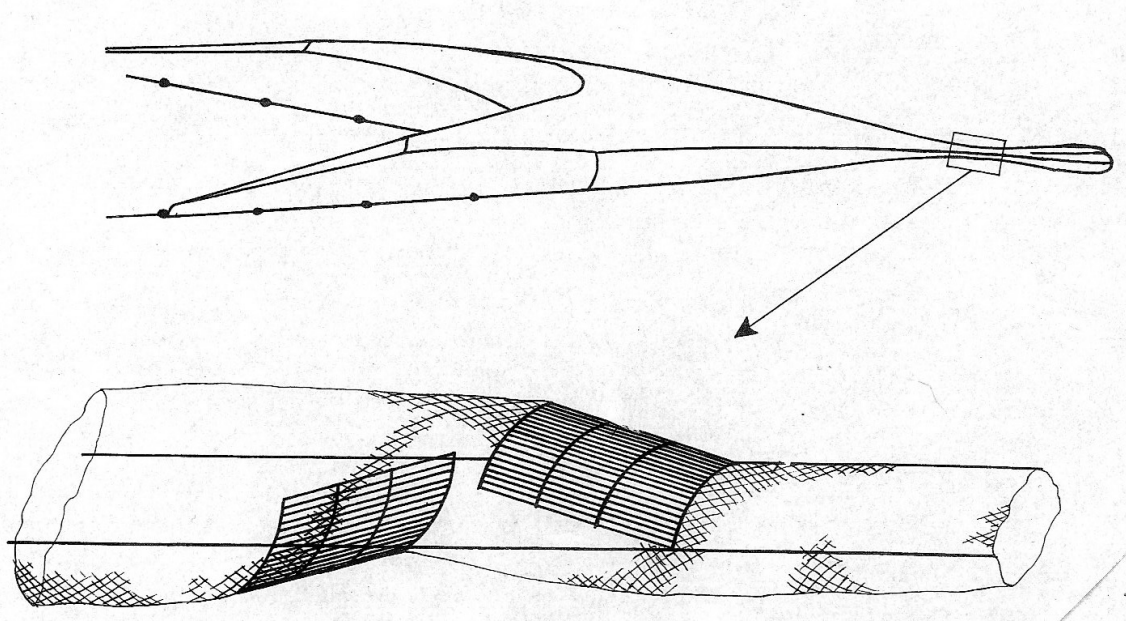


Figure 1.1: Illustration of a trawl with a sorting device.

on the inflow conditions. Secondly the possibility to study the flow conditions to be able to analyze the velocity field within the trawl due to the shape of the trawl, the solidity of the netting for the different parts of the trawl and the influence of any possible sorting devices. And finally the ability to study the pressure in front of the trawl, based on the assumption that the fish is able to detect the trawl due to an alternation of the experienced pressure field. However on what level the fish is able to detect small variations in the pressure field is unclear. It is likely that the most important method for the fish to sense the trawl is to detect it by visual means (Kim & Wardle 2003).

1.2 Net structures

Net structures comes in many different shapes and sizes, for instance net cages for aquaculture purpose, purse seines, trawls for shrimp fishing and large midwater trawls for catching of pelagic fishes. Some examples are shown in Figure 1.2. A large midwater trawl for pelagic fishing can be several hundred meters long, have a circumference of the opening part of 1000 meters and several trawls can be used together to make up double and triple trawl system. A trawl will in addition to the net consists of several other parts like warp lines, trawl doors and floats. Figure 1.3 shown a typical set-up of a trawl. A net cage will typically have a circumference of 100 meter and a depth of 15 meter.

A net consist of twines which connect in knots and make up a mesh. The diameter of a

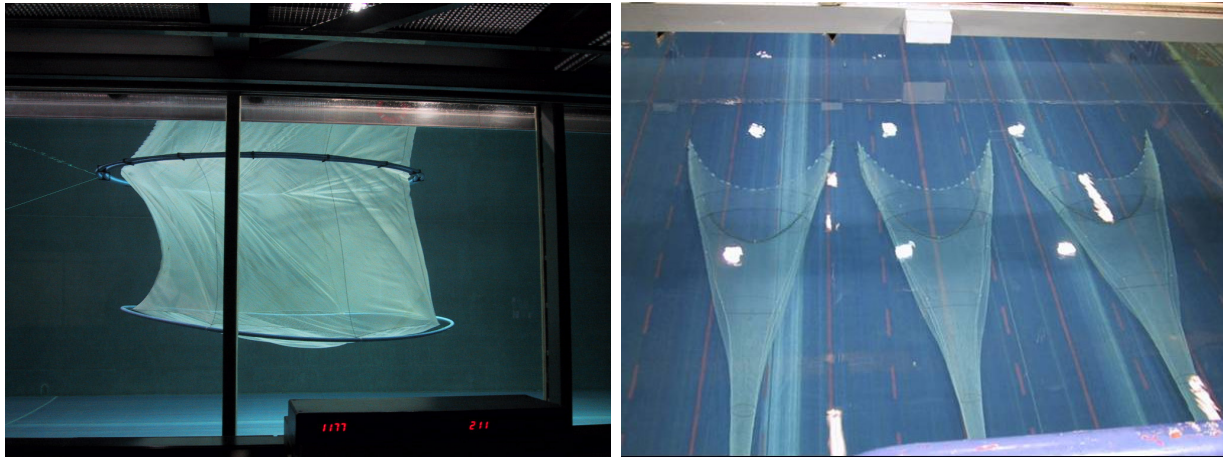


Figure 1.2: A model of a net cage for aquaculture purposes to the left and of a triple trawl for shrimp fishing to the right. Pictures from model tests in a flume tank in Hirtshals.

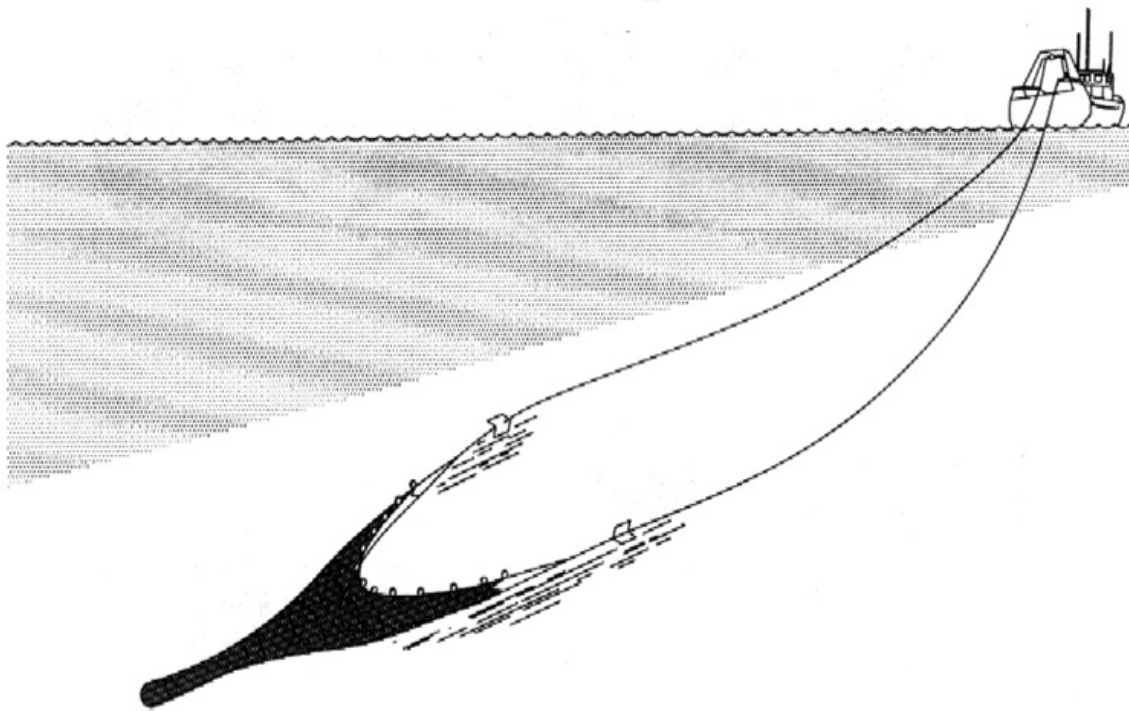


Figure 1.3: Illustration of a bottom trawl with warp lines.

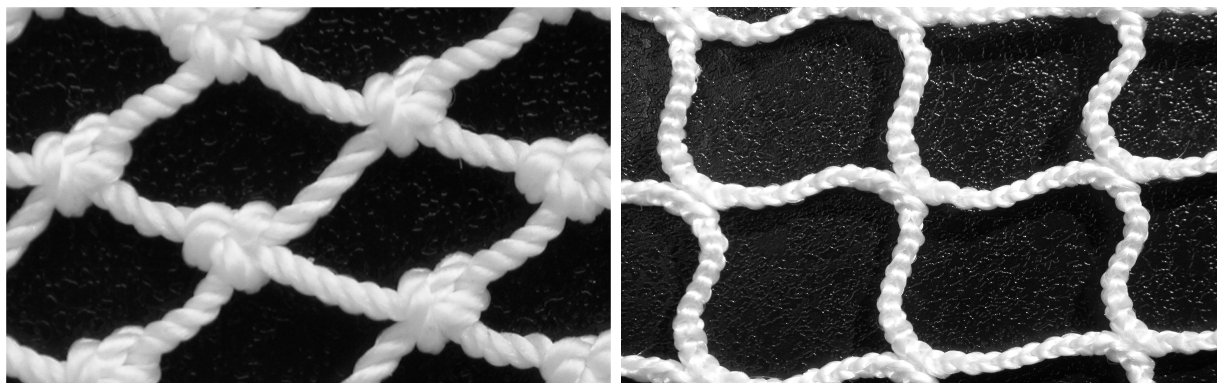


Figure 1.4: Picture of a traditional mesh with knots and diamond orientation (left) and a knotless mesh with square orientation used for aquaculture net cages (right). Twine diameter $d = 1.2 [mm]$ and halfmesh opening $\lambda = 10.0 [mm]$ and twine diameters $d = 2 [mm]$ and halfmesh opening $\lambda = 22.5 [mm]$.

twine can be from $1 [mm]$ in net cages up to a few centimeters in the front part of a trawl. And similar the size of the mesh can be from $1 [cm]$ up to the order of a meter. Typical Reynolds number range, related to the diameter of a twine, is $O(10^2 - 10^4)$.

Figure 1.4 show pictures of details of two different types of nets that are commonly used, with a square shaped and diamond shaped mesh configuration. A net panel can normally be used both with a square or diamond configuration by orienting the net to obtain the desired configuration. The nets in Figure 1.4 differ also with respect to material properties and manufacturing, which is noted as completely different knots. The nets are normally denoted knotted and knotless net type. But as seen, even though the net is denoted a knotless mesh, the connection area (knot part) have shape and physical dimensions different from an idealized knotless connection between intersecting twines.

In net cages, used for aquaculture purposes, the square mesh type is mainly used, while in trawling normally the diamond mesh type is used. In open sea fish farming a constant flow of clean water is important, thus it is favored to use a square mesh orientation of the net which assure a constant and controlled mesh opening. In trawling other aspects are important, such as the distribution of tension within the net structure and that when exposed to drag force, the opening of the meshes in the aft part of a trawl will become smaller, and even close. This also implies that there is less control of the actual opening of the meshes while trawling, which is an important aspect with regards to selectivity. Thus the geometrical flexibility of the two mesh configurations is very different. This can be qualitatively understood by just pulling on each side of a net with different types of mesh.

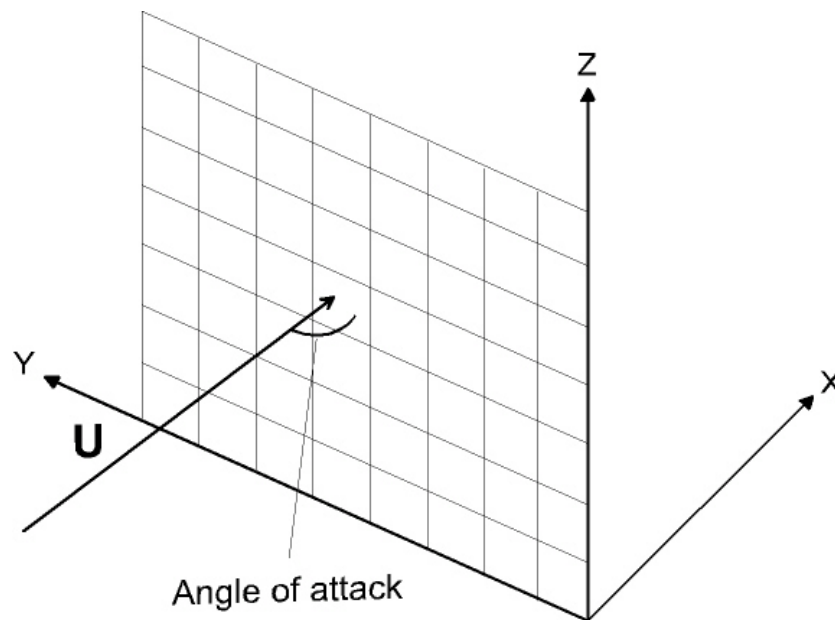


Figure 1.5: Definition of angle of attack, α , for plane net structures. It is assumed that the ambient inflow vector is restricted to be in the xy -plane.

1.3 Analysis of a net structure

Fridman (1992) defines selectivity as the property of a fishing gear to catch fish of a certain size and species from a given mixed population. This property depends mainly on the principle of the fishing method used, but it also depends on the design parameters of the fishing gear such as mesh size, loads on twines, material and thickness of twines, hanging ratios and towing speed. Second to the methods of capture, mesh size has the greatest influence on selectivity (Treshchev 1974).

There are four main parameters which are relevant when discussing the flow and drag force related to a net structure:

- the angle of attack, α , for the net panel (see Figure 1.5)
- the Solidity ratio, Sn , of the net,
- the Hanging ratios, E_1 and E_2 , of the mesh and
- the Reynolds number, Rn , of the individual twines.

The Hanging ratio describes the diamond shape of the mesh and is a function of the angle of the mesh opening. Definitions are given in Figure 1.6. In the crosswise direction of a

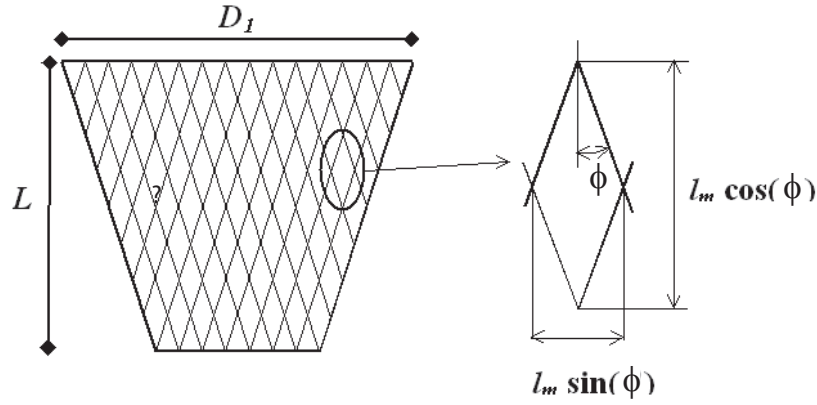


Figure 1.6: Definition of mesh properties.

net panel the hanging ratio is defined as:

$$E_1 = \frac{D_1 \pi}{T_1 l_m} = \sin \phi \quad (1.1)$$

and in the longitudinal direction as

$$E_2 = \frac{L}{NT_1 l_m} = \cos \phi \quad (1.2)$$

where D_1 is the diameter and T_1 is the number of meshes at the front part of the net panel, L is the length between the front and aft part of the net panel, N is the number of meshes in the longitudinal direction, l_m is the mesh opening and 2ϕ is the angle of the mesh opening.

The Solidity ratio, Sn , describes the ratio of the projected area of the net, A_p , over the total area, A , enclosed by the net. In general the Solidity ratio will become a function of the Hanging ratios:

$$Sn = \frac{2d}{l_m E_1 E_2} - \left(\frac{d}{l_m}\right)^2 \left(\frac{1}{E_1^2} + \frac{1}{E_2^2}\right) \quad (1.3)$$

where d is the twine diameter. For a square mesh the angle of the mesh opening 2ϕ will become equal to 90 [deg], and the Solidity ratio can be expressed as:

$$Sn = \frac{2d}{\lambda} - \left(\frac{d}{\lambda}\right)^2 \quad (1.4)$$

where λ is defined as the half mesh equal to $0.5l_m$ and is the same as the length of one side in a square mesh. Thus Sn is a ratio related to the size relation between the diameter and mesh opening of a net.

Table 1.1: Properties of the nets used for the experiments by Rudi et al. (1988).

Sn [-]	0.13	0.144	0.184	0.243	0.317
Twine diameter d_t [mm]	1.830	1.380	1.081	1.830	1.830
Half mesh size λ [mm]	29.0	19.5	12.0	15.5	12.0

The Reynolds number, which is an important parameter related to the flow around each twine and knot, is defined as:

$$Rn = \frac{U d}{\nu} \quad (1.5)$$

where ν is the kinematic viscosity and U is the incoming flow velocity. In addition while studying the detailed flow around single twines, the surface and how the twine is twisted, may matter in relation to vortex shedding.

In Figure 1.7, Figure 1.8 and 1.9 results for the drag force on net panels as a function of Solidity ratio, Sn , Reynolds number, Rn and angle of attack, α , based on experiments by Rudi, Løland & Furunes (1988), are presented. The experiments were carried out by towing plane nets, framed to keep the shape, with different properties at different velocities and angles of attack. Nets with square mesh and knots (see Figure 1.4) were used with the properties presented in Table 1.1

The results are presented as non-dimensionalized drag force coefficients, C_d , by dividing the drag force with $0.5\rho A U_\infty^2$, where A is the enclosed area of the net. The following can be seen from the results:

- There is a clear Reynolds number dependency for the drag coefficient.
- The Reynolds number dependency is increasing with increasing Solidity ratio.
- The Reynolds number dependency is decreasing with decreasing angle of attack.

The individual shape of the twine and the knot part will likely have an influence on the drag on the net. This is an important factor to consider when interpreting the results in Figure 1.7, Figure 1.8 and 1.9. The largest difference between the actual net and an idealized net structure made up of equivalent cylinders will be the knot part. A non circular shape of the twine and the knot part will tend to increase the drag coefficient, while a stranded wire type of shape as in Figure 1.4 might slightly decrease the drag coefficient (Hoerner 1965).

The change in drag coefficient of the individual parts which make up the net, partly explains the behavior seen in the experimental results by Rudi et al. (1988). As seen from

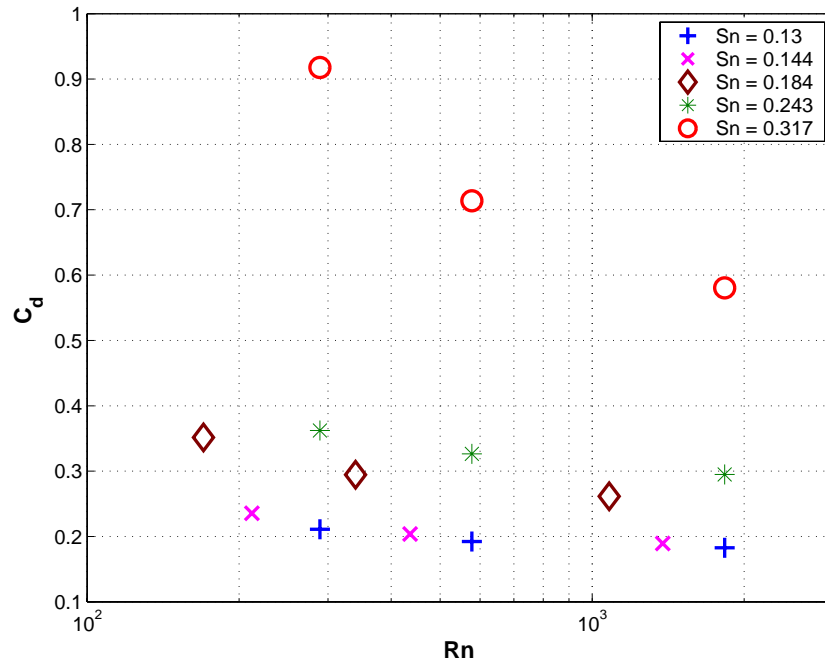


Figure 1.7: Drag coefficient for plane nets with different Solidity ratios at 90 [deg] angle of attack, as a function of Reynolds number with respect to the twine diameter d_t . (Rudi et al. 1988)

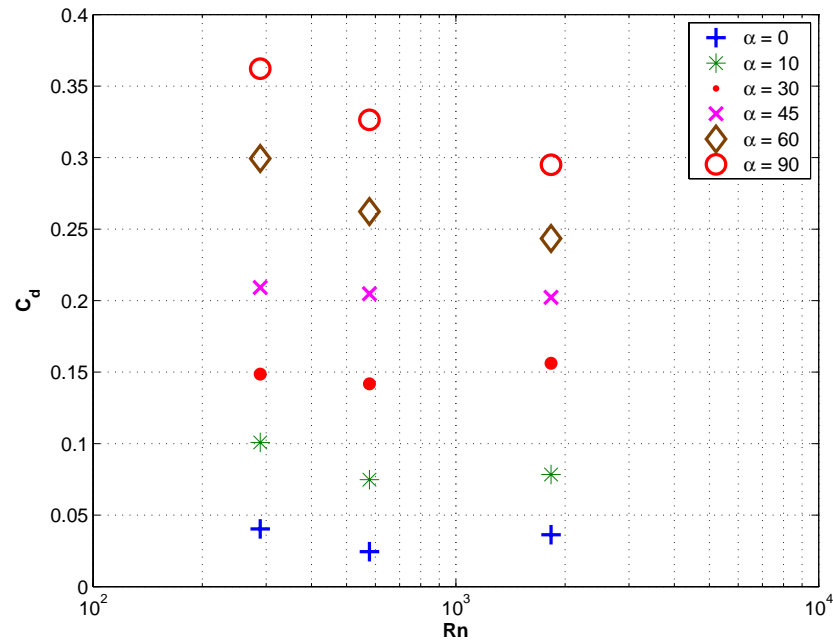


Figure 1.8: Drag coefficient for a plane net with a Solidity ratio of 0.243 at different angles of attack, as a function of Reynolds number with respect to the twine diameter d_t . (Rudi et al. 1988)

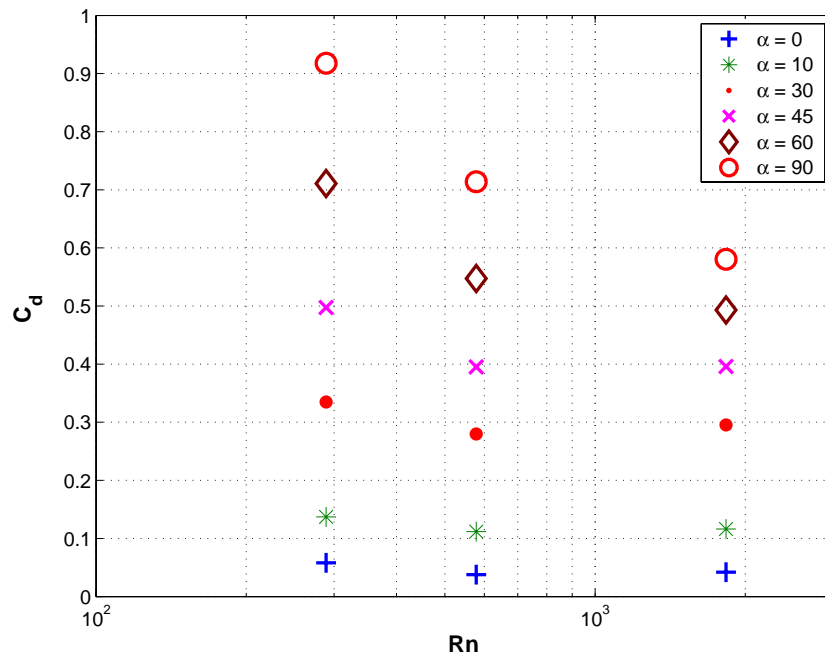


Figure 1.9: Drag coefficient for a plane net with a Solidity ratio of 0.317 at different angles of attack, as a function of Reynolds number with respect to the twine diameter d_t . (Rudi et al. 1988)

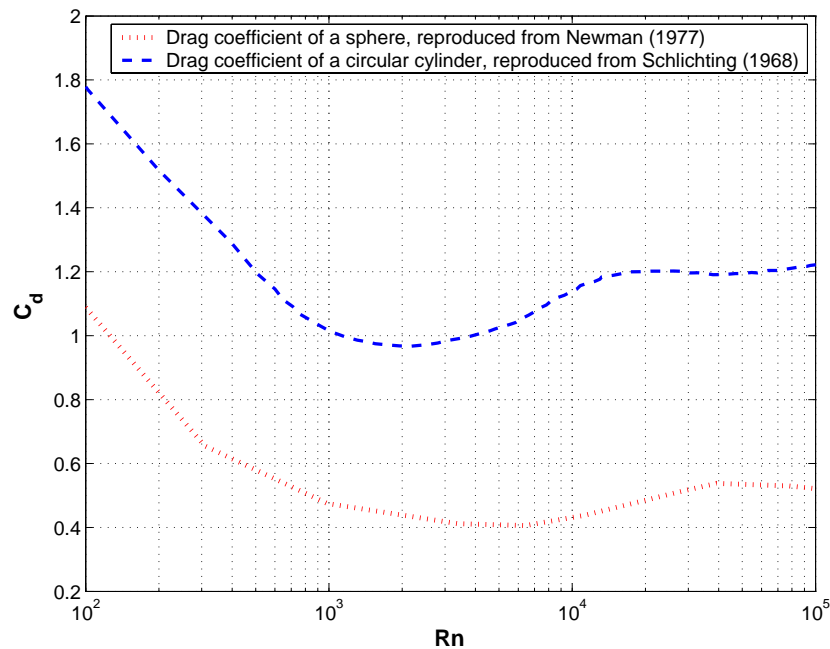


Figure 1.10: Drag coefficients of a circular cylinder and a sphere as a function of Reynolds number with respect to sphere and cylinder diameter, respectively. Reproduced from Schlichting (1968) and Newman (1977).

Table 1.2: The drag coefficient for the twine, C_{dt} , and the knot part, C_{dk} , as a function of Reynolds number with respect to the twine and knot diameter, respectively. Values taken from Figure 1.10.

Rn [-]	170	212	289	340	436	578	1081	1380	1830
C_{dt}	1.57	1.5	1.35	1.33	1.28	1.15	1.0	1.0	1.0
C_{dk}	0.85	0.8	0.7	0.62	0.6	0.55	0.5	0.45	0.45

Figure 1.10, in the relevant Reynolds number range between 10^2 and 10^4 , the drag coefficient for a cylinder varies approximately between 1.0 – 1.8 and for a sphere approximately between 0.4 – 1.1.

In Figure 1.11 the experimental results by Rudi et al. (1988) are plotted together with the ratio, R_{Cdnet} , between the drag force from the experiments and the drag force calculated as a sum of the drag forces on the individual elements, using an equivalent drag force coefficient of a cylinder for the twine and of a sphere for the knot part. The actual values used for the drag coefficient of the twine and knot part, are presented in Table 1.2 and are taken from Figure 1.10. The diameter of the knot is taken to be 150% of the diameter of the twine.

The closer R_{Cdnet} is to 1.0, the more accurate is the assumption that the drag force of the net can be calculated as a sum of the drag forces on the individual elements. The results indicate that there is no uniform relation between the drag force on the plane nets used for the experiment and the Solidity ratio. This might be due to differences in the knot part between the different nets, but unfortunately detailed knowledge of the properties of the net is not available. At the same time it is clear that the results for the highest Solidity ratio, $Sn = 0.317$, deviates the most from a value of $R_{Cdnet} = 1.0$. This indicate that the drag force on the net can not be treated only as a sum of the drag forces on individual elements, when the Solidity ratio increases above a certain value. This non-uniform relation between the drag force and the Solidity ratio is noted by several authors, for instance Koritzky (1974) and Fridman (1992), but is not explained. Thus this Solidity ratio dependency of the drag force on a net is not clearly understood.

How the flow is influenced by the knot part is not apparent. It is not enough only to consider the increased area due to the knot part to explain the increasing drag force since the effect is both a function of the Reynolds number and the Solidity ratio. It is likely that there is a flow interaction between the different parts of the net around the knot part. In later sections these aspect will be discussed further and sought explained.

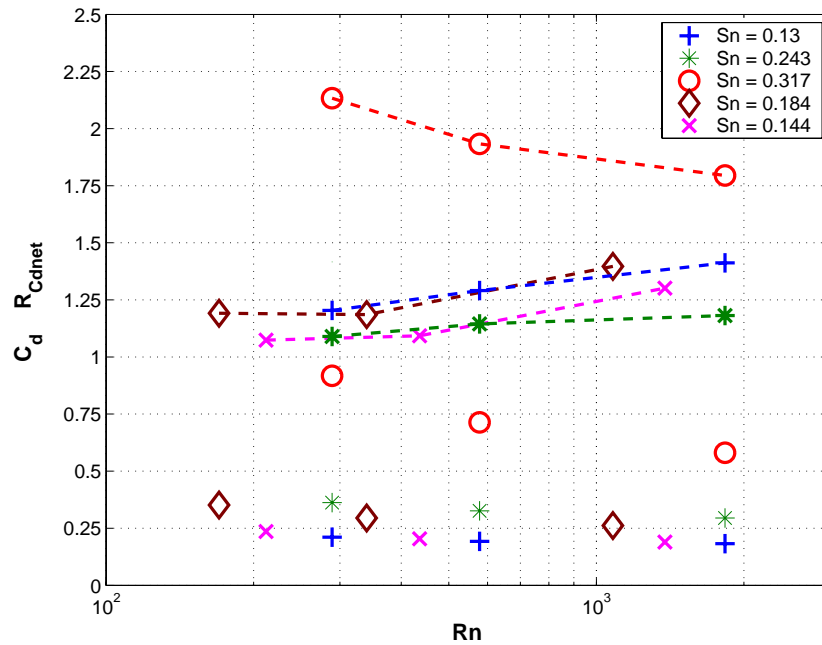


Figure 1.11: Drag coefficient for plane nets (markers) and ratios between drag for plane nets and drag calculated as sum of the drag for individual elements (markers and dashed line). Different Solidity ratios at 90 [deg] angle of attack. Results as a function of Reynolds number with respect to the twine diameter d_t . Drag coefficient for plane nets based on experimental results by Rudi et al. (1988).

1.4 Modeling of a net structure

There is in principle two main approaches to model the forces acting on a net and the behavior of a net. First to model the net as individual knots and twines, calculating the total drag on the net as sum of the drag of the individual elements and applying a structural analysis based on truss elements (Theret 1994). This approach makes it possible to account for details in the net structure and study the flow inside and around the net structure. Secondly it is possible to assume that the net is made up of surface elements, with properties accounting for the underlying twine and knot structure. Then the drag force on the net element can be given as a net drag coefficient as a function of the Solidity ratio of the net (Løland 1991, Aarsnens, Løland & Rudi 1990) or be calculated using a Computational Fluid Dynamic (CFD) approach (Vincent & Marichal 1996). A standard structural Finite Element Method (FEM) approach can be utilized to calculate the response on the structure. Calculating the drag force using a net drag coefficient is an efficient method, and even though it do not consider the details of net and consequently the flow, have shown to give good results for a limiting Reynolds number range.

1.4.1 Related work

There has historically been done some work related to permeable nets or structures, especially related to research of the flow field in flume tanks, wind tunnels and parachutes. But previous work related to investigation of the flow field around and through a net structure like for instance a trawl, is limited.

Modeling of flow around a 2D net using sources and centers of resistance

Among the earlier published works on the subject are the papers by Taylor (1944) and Taylor & Davies (1944) related to the studies of the resistance of a porous sheet to the passage of air in two dimensions and the paper by Koo & James (1973) studying the steady two-dimensional flow around a submerged screen in a parallel-sided channel.

To describe this resistance Taylor used a non-dimensional pressure drop or resistance coefficient κ , defined by:

$$p_1 - p_2 = \kappa \left(\frac{1}{2} \rho u^2 \right), \quad (1.6)$$

where p_1 is the pressure on the windward side, p_2 on the leeward side and u is the mean wind velocity through the net.

To be able to model the net, Taylor considered the sheet to be a uniform distribution of centers of resistance, each with a drag of δR which produces a wake. The flow outside of

this wake will roughly be equivalent to that which would be produced by a distribution of source strengths $\delta R/\rho u$. Thus, the resistance $\frac{1}{2}\kappa\rho u^2$ per unit area produces the same flow outside the wake (but not behind the sheet) that would be produced by a plane of sources of strength $\frac{1}{2}\kappa\rho u^2/\rho u = \frac{1}{2}\kappa u$ per unit area. Such a plane of sources would give rise to a flow away from the plate equal to $-\frac{1}{4}\kappa u$ in all directions in the plane. Further, the flow close in front of the sheet/net due to the superposition of the main stream velocity U_∞ and the source system will then become

$$u = U_\infty - \frac{1}{4}\kappa u,$$

or

$$\frac{u}{U_\infty} = \frac{1}{1 + \frac{1}{4}\kappa} \quad (1.7)$$

Using Bernoulli's theorem and assuming that κ is small, the resistance coefficient of the sheet would be given by

$$C_d(\frac{1}{2}\rho U_\infty^2) = \frac{1}{2}\kappa\rho u^2 \quad (1.8)$$

so that the drag coefficient of a flat plate sheet of porous material will become

$$C_d = \frac{\kappa}{(1 + \frac{1}{4}\kappa)^2} \quad (1.9)$$

Koo & James (1973) constructed their model by first replacing the screen with a distribution of sources and then manipulating the stream function for the flow so that the mass and momentum balances across the screen are satisfied. Consequently the model predicts a flow field which is realistic except for the expected discontinuity in velocity between the wake and external flow.

The reduction in pressure was like in Taylor (1944) expressed by the dimensionless pressure drop or resistance coefficient κ .

$$\kappa = \frac{\delta p}{\frac{1}{2}\rho(U \cos(\theta))^2} \quad (1.10)$$

When the velocity normal to the screen is sufficiently large, the pressure drop coefficient is independent of the magnitude of the velocity. This is analogous to and related to the constancy of the drag coefficient for sufficiently large Reynolds numbers for the flow around submerged bodies.

These two approaches are described more thoroughly by Løland (1991) in his PhD thesis.

A computational fluid method to calculate the flow in a cod end Looking at the cod-end of a trawl and assuming that the flow is axi-symmetric, Vincent & Marichal (1996) developed a viscous method for calculating the two dimensional flow field based on the Navier-Stokes equations and a $K - \epsilon$ turbulence model. The net was modeled as a homogeneous and permeable thin surface.

The flow is characterized and described by the tangential u_t and normal velocity u_n and the velocity at the net is decomposed into a normal and a tangential vector. Then the loss of pressure over the net is used to calculate the normal vector:

$$u_n = \bar{\alpha} \frac{\Delta p}{\rho U_\infty} \quad (1.11)$$

To calculate the tangential velocity, the Shaffman's law, expressing the relation between friction and adhesion is used:

$$u_t = \bar{\beta} \frac{\tau_{eff}^- + \tau_{eff}^+}{\rho U_\infty} \quad (1.12)$$

$$\tau_{eff} = (\mu + \mu_t) \frac{\partial u_t}{\partial t} \quad (1.13)$$

where the $+$ and $-$ indicate internal and external surface of the cod-end respectively. The coefficients $\bar{\alpha}$ and $\bar{\beta}$ are supposed to depend only on local mesh shapes, and are found by experiments.

Empirical formulation for the net drag coefficient Aarsnens et al. (1990) proposed an empirical formulation, which is based on experiments by towing plane nets with different Solidity ratios through a towing tank at different velocities and angles of attack (Rudi et al. 1988). The experiments were carried out using nets with a Solidity ratio range from 0.130 to 0.317, and the empirical formulation was "optimized" for the middle solidity ratio range and at the highest Reynolds number.

Milne (1970) proposed an analytical formulation, which is also verified against nets with a relatively low range of Solidity ratio. The formulation of Aarsnes and Løland is a third order equation with respect to Solidity ratio, while the formulation which Milne based his findings on, is a second order equation with respect to the Solidity ratio. When increasing the Solidity ratio out of the "optimum" range for the actual models, the effect on the results could be large, which might limit the validity of these models outside the Solidity ratio and Reynolds number range of the experiments.

Structural modeling In recent years some work has been done on developing structural methods and formulation for net structures and cod-ends (aft part of a trawl where the catch is collected). For a general structural analysis of the net structure, two different basic

models has been employed, either using as a set of truss elements, representing the twines (Theret 1994, Niedzwiedz 2001) or alternatively as elements with global characteristics (Prior 1998, Tronstad 2000). Theret (1994) assumes that the truss elements are stiff and calculated force balance in node points, while Niedzwiedz (2001) use elastic elements. In the presented work, a method using truss elements with elasticity is employed. This is further described in Chapter 4.1.3.

Differential equations for the geometry of the cod-end, based on an approach using a method of force balance in the connection between the individual twines, has been investigated by O'Neill & O'Donoghue (1997). O'Neill (1997) has also investigated the fluid dynamic loading on catch. And recently models and experiments for detailed analysis of the behavior of the cod-end has been developed by Dret, Priour & Chagneau (2004).

Dynamic behavior of net structures Lader, Enerhaug, Fredheim & Krokstad (2003) has developed a dynamic 3-D model, based on a similar load description as Aarsnens et al. (1990) in steady case. Bessonneau & Marichal (1998) has performed studies of the dynamics of complete trawl structures, assuming a uniform flow model. They use the truss element model for the structural analysis as well as Vincent (1999), which has developed a numerical tool to study the dynamic behavior of a trawl, based on a uniform flow approach.

1.4.2 Present approach

The objective has been to develop simplified and physically justified methods. By combining the change in the inflow due to the presence of the net structure, which is a function of the shape and geometry of the net, with a correction of the shape and geometry due to the drag load, a more complete description of the problem is obtained. Therefore a structural analysis of the net structure using a FEM method is included.

Further it is impractical to model every single twine in a net or a trawl. Typically the total number of twines could be in the order of 10^6 . In the present approach, it is assumed that the total drag on a trawl or net structure can be calculated by adding up the drag on sub parts or elements of the net structure. And that further, for a given Reynolds number, keeping the Solidity ratio constant, the total drag on the trawl will be independent on the actual diameter and mesh opening of the net. This principle is well established regarding analysis of net structures such as trawl and net cages (Paschen & Winkel 1999, Winkel & Paschen 2001).

In the present work, the three-dimensional net structure is divided into discrete elements. The twines are modeled as separate cylinders between knots, with two-dimensional properties, allowing the interaction between them to be three-dimensional. The knots are modeled

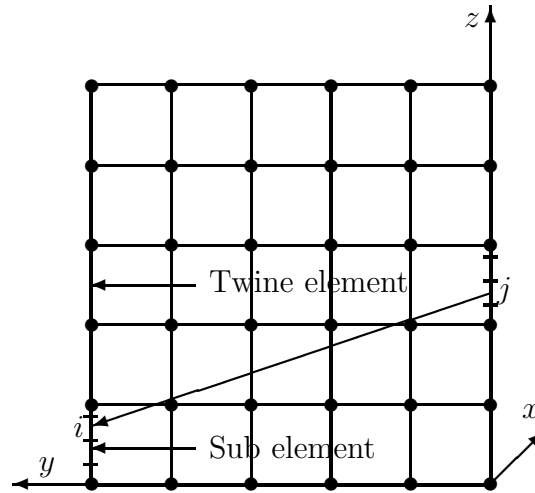


Figure 1.12: Illustration of modeling of the net

as separate spheres, with full three-dimensional properties. The modeling is illustrated in Figure 1.12. Each of the twine elements between knots can further, but do not have to, be divided into sub elements, as illustrated in the figure. The total drag on the net will then become a sum of the drag of each of the individual elements. The drag on each element is calculated as the drag on a single circular cylinder in a two-dimensional free flow, which can be expressed as

$$\mathbf{F}_c = 1/2\rho C_d dL|\mathbf{U}_{2D}|\mathbf{U}_{2D} \quad (1.14)$$

where \mathbf{U} is the inflow velocity vector in a plane orthogonal to the cylinder axis. $|\mathbf{U}|$ is the magnitude of the inflow velocity, C_d is the drag coefficient for the cylinder, d is the diameter and L is the length of the cylinder. The expression for the drag on a sphere in three-dimensional free flow will in a similar fashion become

$$\mathbf{F}_s = \pi d^2/8\rho C_d|\mathbf{U}_{3D}|\mathbf{U}_{3D} \quad (1.15)$$

where $\pi d^2/4$ is the projected area of the sphere.

First the influence from the net on the fluid flow is calculated by representing the wake generated by each element as source distributions along the structural element. To determine the strength of these sources the principle of Lagally is applied, which basically states that the force acting on a source of strength q in uniform flow is equal to the source strength times the incoming velocity times the fluid density. Thus a set of equations is obtained, describing the relation between the fluid velocity and the source strength at every element. And this leads to a model that describes the disturbance of the fluid flow in front of the net, due to the presence of the net. This is described further in Chapter 2.

Secondly the interaction between the net elements, due to the physical generation of a wake flow behind each individual element of the net, has been studied using a time-averaged

velocity deficit model. Different models have been tried out. The basis for all the models is the far field mean velocity deficit model for the flow behind a single cylinder described by Schlichting (1968). Modifications are applied, to better describe the near field behavior and the added effect on the total flow field due to the generation of the wake from the many individual cylindrical elements which make up the net. The reduced inflow for one element of the net due to the generated velocity deficit from all the proceeding elements is calculated. This makes it possible to analyze the current forces on a net structure at different angles of attack (see Figure 1.5). More about this part in Chapter 3.

Combining these two effects, together with a structural analysis, a complete model appropriate for analysis of current forces and response on three-dimensional net structures is established. Results for three-dimensional net structures are presented in Chapter 4.

1.5 Contributions

The following points summarize the new contributions from this work

- An examination of numerical results for the drag force on plane net structure demonstrates a strong dependency of the drag force on a net structure with both the geometry, in terms of Solidity ratio and the Reynolds number. And in particular a non-uniform relation between the drag force and the Solidity ratio.
- A possible method for handling the effect of several cylinders in in-line and staggered arrangement to the flow, using alternative formulations of the time averaged far wake mean velocity deficit model by Schlichting (1968) and applying them in the near field downstream of the cylinders.
- A qualitative explanation to the experienced significant mean negative lift force, acting towards the mean wake axis, on a cylinder in certain staggered arrangements. This is explained by experiments and simple theory as interaction between vortices shed from the upstream cylinder and the flow around the downstream cylinder.
- A method to calculate the drag force on net structures with high solidity. The method uses appropriate drag coefficients related to the geometry of the twines and the knots and account for the change in the inflow due to the presence of the net structure and at the same time changes the geometry of the net structure due to the load.
- The importance of including elasticity in the model to account for geometrical changes in the net structure for load calculations. The elasticity of the net structure has a direct influence on the geometry of the net structure when exposed to external force and will then have an effect on the experienced drag force.

- A method to calculate the velocity field in front and within a three-dimensional net structure, which account for elasticity of the net, variations in Solidity ratio and changes in geometry due to external loads.

CHAPTER 2

Modeling upstream effects

2.1 Introduction

This chapter will describe how the disturbance from the individual elements on the flow and the interaction effect between the elements, is modeled. The influence from the net on the fluid flow, are in this part calculated by representing the wake generated by each element as source distributions along the structural element and as point sources at the knot part. Thus implicitly it is assumed that no elements are in the wake of other elements. This implies that if some elements are in the wake of other elements, the reduced inflow due to velocity deficit in the wake at this point, is not corrected for.

The three-dimensional net structure is divided into discrete elements. First the twines are modeled as separate cylinders between knots, with two-dimensional properties, allowing the interaction between them to be three-dimensional. Later the knots are added into the model, modeling them as separate spheres, with full three-dimensional properties. The reason why inclusion of the knot part in the model were necessary is explained later. The modeling is illustrated in Figure 1.12. The cylinders and spheres are named twine elements and knot elements respectively. Each of the twine elements between knots can further, but do not have to, be divided into sub elements, as illustrated in Figure 1.12. In the following, it is not distinguish between twine elements and sub elements, if not specifically stated that sub elements are discussed. The drag on each of the elements are calculated using standard

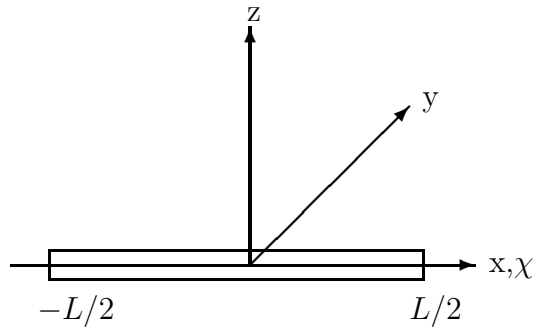


Figure 2.1: Definition of local axis system for a two dimensional slender body element.

drag formulation as described in 1.4.2. The total drag on the net will then become a sum of the drag of each of the individual elements.

2.2 Disturbance potential

The fluid is assumed to be incompressible and it is defined a time average wake behind each twine and knot. Outside of this wake, the fluid is assumed inviscid and the fluid motion irrotational, i.e. a velocity potential can be used to describe the fluid velocity, $\mathbf{U} = \nabla\phi$. This velocity potential will then satisfy the Laplace equation $\nabla^2\phi = 0$. The presence of the wake is modeled by sources centered in the twines and knots.

First a twine element between two knots is considered. The dominant far-field solution, outside the wake, of the velocity potential at point (x, y, z) due to the disturbance of the twine, can be represented as:

$$\phi_c(x, y, z, \chi) = \frac{1}{4\pi} \int_{-L/2}^{L/2} \frac{q(\chi)}{\sqrt{(x - \chi)^2 + y^2 + z^2}} d\chi \quad (2.1)$$

Where $q(\chi)$ are the source distribution along the element and definitions of the coordinates are given in Figure 2.1.

And similarly the disturbance at point (x, y, z) due the knot elements can be modeled as a three-dimensional point source:

$$\phi_s(x, y, z) = \frac{1}{4\pi} \frac{Q}{\sqrt{x^2 + y^2 + z^2}} \quad (2.2)$$

Where Q is the source strength of a point source. Since the twine element is defined as the element between two knots, the twine element and the knot element will not have the

same location. Thus the source distribution representing the twine element and the point source representing the knot element will neither have the same location.

The unknown in these equations are the source strength distribution for the twine elements and the source strength for the knot elements, respectively. To find a relation between the source strength and the drag force on the element, the Lagally's theorem is used. The Lagally's theorem (Milne-Thomson 1968) basically state that the force acting on a source of strength q in uniform flow can be expressed as:

$$\mathbf{F} = \rho q \mathbf{U} \quad (2.3)$$

Where ρ is the fluid density and \mathbf{U} is the fluid velocity vector. The theorem is valid both in two and three dimensions.

Using the standard drag formulation for the drag force acting on a cylinder (or sphere) in free flow, Equation (1.14), it is possible to establish a relation between the source strength and the fluid velocity. Thus when the source is a representation of the cylinder, the expression for the source strength becomes:

$$q = \frac{1}{2} C_d d |\mathbf{U}| \quad (2.4)$$

2.3 Equation system

With Equation (2.1), (2.2) and (2.4) the necessary relations to establish a system of equations to solve the problem is given. Equation (2.4) is then applied at the center of every element (twines, including any possible sub elements and knots) in the net structure, where \mathbf{U} will be a function of the incoming free flow $\bar{\mathbf{U}}$ and the sum of the disturbance \mathbf{u} , from all the other elements. The disturbance from each individual element is given by Equation (2.1) and (2.2). A set of equations where the unknown source strength q for a twine element i is given as a function of the influence of all the other elements (see Figure 1.12), is then established. A similar set of equations is also established for the unknown source strength Q for every knot element.

The equations for element i will then become as follows for the twine elements and knot elements respectively:

$$q_i = \frac{(C_d d l)_i}{2} \left| \bar{\mathbf{U}}_i + \sum_{j=1 \neq i}^{N_c} \mathbf{u}_{cj} + \sum_{k=1}^{N_s} \mathbf{u}_{sk} \right|_{2D} \quad (2.5)$$

$$Q_i = \frac{(C_d d^2)_i}{8} \left| \bar{\mathbf{U}}_i + \sum_{j=1}^{N_c} \mathbf{u}_{cj} + \sum_{k=1 \neq i}^{N_s} \mathbf{u}_{sk} \right|_{3D} \quad (2.6)$$

where d is the diameter of the twine or knot element, l is the length of the twine element, \mathbf{u}_{cj} is the disturbance from the twine elements j , \mathbf{u}_{sk} is the disturbance from the knot element k , N_c is the number of twine elements and N_s is the number of knot elements. The total number of elements is then $N_c + N_s = N$. Since the theorem of Lagally's is used, which directly is the relation between the flow velocity and the source strength, there is no influence from the i element on the i element itself. Due to this, the element index i is removed from the sum in the equations. For the twine element it is the decomposed two-dimensional velocity in the plane perpendicular to the element i which is used in the equation, i.e. $\bar{\mathbf{U}} = \langle \bar{U}_x, \bar{U}_y \rangle$ and $\mathbf{u} = \langle u_x, u_y \rangle$

Since the right hand side of the equations involve the scalar of the velocity vector, the following square system for the unknown source strengths of the twine elements has to be solved

$$q_i^2 = \left(\frac{(C_d dl)_i}{2} \left(\bar{U}_{xi} + \sum_{j=1 \neq i}^{N_c} u_{cxj} \right) + \frac{(C_D D^2)_i}{8} \sum_{k=1}^{N_s} u_{sxk} \right)^2 + \left(\frac{(C_d dl)_i}{2} \left(\bar{U}_{yi} + \sum_{j=1 \neq i}^{N_c} u_{cyj} \right) + \frac{(C_d d^2)_i}{8} \sum_{k=1}^{N_s} u_{syk} \right)^2 \quad (2.7)$$

and similarly for the knot elements

$$Q_i^2 = \left(\frac{(C_d dl)_i}{2} \left(\bar{U}_{xi} + \sum_{j=1}^{N_c} u_{cxj} \right) + \frac{(C_d d^2)_i}{8} \sum_{k=1 \neq i}^{N_s} u_{sxk} \right)^2 + \left(\frac{(C_d dl)_i}{2} \left(\bar{U}_{yi} + \sum_{j=1}^{N_c} u_{cyj} \right) + \frac{(C_d d^2)_i}{8} \sum_{k=1 \neq i}^{N_s} u_{syk} \right)^2 \quad (2.8)$$

For the sake of simplicity the sum of the influences from the twine and knot elements ($\sum u_{c/s}$) are denoted u and the constants are removed in the following equation. Equation (2.7) can then be expressed as:

$$q_i^2 = \left(\bar{U}_x^2 + \bar{U}_y^2 + 2\bar{U}_x u_x + 2\bar{U}_y u_y + u_x^2 + u_y^2 \right) \quad (2.9)$$

This equation consists of one part due to the undisturbed uniform flow, one part solely due to the disturbance and one term including both the uniform velocity and the disturbance. If it is assume that uniform flow is of $O(1)$ and that the disturbance is of $O(\epsilon)$, where ϵ is a small parameter, the three parts will be of $O(1)$, $O(\epsilon^2)$ and $O(\epsilon)$, respectively. It would then be tempting to remove all terms of $O(\epsilon^2)$. But this would result in a model with no interaction between the elements for a flat net in the yz -plane with a uniform flow in the x -direction, at a 90 [deg] angle of attack. Thus terms of $O(\epsilon^2)$ are kept in the further formulation. If it is necessary to keep this term, is not obvious. This will be further discussed in Section 2.8.1.

2.4 Velocities

The unknown source strengths q_i and Q_i are solved by introducing the disturbance from the other elements as the velocity in Equation (2.7). The velocities are then given by differentiating the disturbance potentials given in Subsection 2.2. In a local coordinate system for the twine element j as given in Figure 2.1, the x,y, and z-velocities (index c indicates twine element) becomes:

$$\frac{\partial\phi}{\partial x} = u(x, y, z; \chi)_{cx} = \frac{1}{4\pi} \int_{-l/2}^{l/2} \frac{q(\chi)(x - \chi)}{(x^2 - 2x\chi + \chi^2 + y^2 + z^2)^{3/2}} d\chi \quad (2.10)$$

$$\frac{\partial\phi}{\partial y} = u(x, y, z; \chi)_{cy} = \frac{1}{4\pi} \int_{-l/2}^{l/2} \frac{q(\chi)y}{(x^2 - 2x\chi + \chi^2 + y^2 + z^2)^{3/2}} d\chi \quad (2.11)$$

$$\frac{\partial\phi}{\partial z} = u(x, y, z; \chi)_{cz} = \frac{1}{4\pi} \int_{-l/2}^{l/2} \frac{q(\chi)z}{(x^2 - 2x\chi + \chi^2 + y^2 + z^2)^{3/2}} d\chi \quad (2.12)$$

and the disturbance from the knot elements which are given in global coordinate system becomes (index s indicates sphere elements):

$$u(x, y, z)_{sx} = \frac{1}{4\pi} \frac{Qx}{(x^2 + y^2 + z^2)^{3/2}} \quad (2.13)$$

$$u(x, y, z)_{sy} = \frac{1}{4\pi} \frac{Qy}{(x^2 + y^2 + z^2)^{3/2}} \quad (2.14)$$

$$u(x, y, z)_{sz} = \frac{1}{4\pi} \frac{Qz}{(x^2 + y^2 + z^2)^{3/2}} \quad (2.15)$$

In general the integrals has to be solved numerically for a given distribution of $q(\chi)$ along the element. But if it is assumed that the source strength is constant over the element, it is possible to solve Equation (2.10), (2.11) and (2.12) for the velocities in x-,y- and z-direction analytically. When the element is situated along the x-axis the solution is as follows:

$$u(x, y, z)_{cx} = \frac{q}{4\pi} \frac{\left(\sqrt{x^2 + xl + l^2/4 + y^2 + z^2} - \sqrt{x^2 - xl + l^2/4 + y^2 + z^2} \right)}{\sqrt{x^2 - 2xl + l^2/4 + y^2 + z^2} \sqrt{x^2 + 2xl + l^2/4 + y^2 + z^2}} \quad (2.16)$$

$$\begin{aligned} u(x, y, z)_{cy} &= \frac{-q}{4\pi} \frac{y}{\sqrt{x^2 - xl + l^2/4 + y^2 + z^2}} \\ &\quad + \frac{q}{4\pi} \frac{y}{\sqrt{x^2 + xl + l^2/4 + y^2 + z^2}} \\ &\quad + \frac{1}{4\pi} \frac{1}{\sqrt{-l/2 - x + \sqrt{x^2 - xl + l^2/4 + y^2 + z^2}}} \\ &\quad + \frac{1}{4\pi} \frac{1}{\sqrt{-l/2 - x + \sqrt{x^2 + xl + l^2/4 + y^2 + z^2}}} \end{aligned} \quad (2.17)$$

$$\begin{aligned}
u(x, y, z)_{cz} &= \frac{-q}{4\pi} \frac{z}{\sqrt{x^2 - xl + l^2/4 + y^2 + z^2}} \\
&\quad + \frac{q}{4\pi} \frac{z}{\sqrt{x^2 + xl + l^2/4 + y^2 + z^2}} \\
&\quad + \frac{1}{-l/2 - x + \sqrt{x^2 - xl + l^2/4 + y^2 + z^2}} \\
&\quad + \frac{1}{-l/2 - x + \sqrt{x^2 + xl + l^2/4 + y^2 + z^2}}
\end{aligned} \tag{2.18}$$

Assuming a constant source distribution does not limit the generality in the further discussion. The possibility of using a different source distribution will be discussed later. Finally, Equations (2.13), (2.14), (2.15), (2.16), (2.17), (2.18), (2.10), (2.11) and (2.12) together with (2.7) and (2.8), are all the necessary equations to solve the problem.

2.5 Numerical solution procedure

The resulting equation system for the unknown source strength is non-linear and to solve for the unknown source strength an iterative solution scheme has to be applied. A very common scheme to use is the Newton-Raphson iterative method. This method involves solving an ordinary $\mathbf{Ax} = \mathbf{B}$ equation system for each iteration step.

For each of the elements, the relation can be expressed as follows:

$$F_i(q_1 \dots q_{N_c}; Q_1 \dots Q_{N_s}) = F_i(\mathbf{q}) = 0 \tag{2.19}$$

And with a Taylor expansion around \mathbf{q} :

$$F_i(\mathbf{q} + \delta\mathbf{q}) = F_i(\mathbf{q}) + \sum_{j=1}^N \frac{\partial F_i(\mathbf{q})}{\partial q_j} \delta q_j + O(\delta\mathbf{q}^2) = 0 \tag{2.20}$$

And for all the $N_c + N_s$ equations together:

$$\mathbf{F}(\mathbf{q} + \delta\mathbf{q}) = \mathbf{F}(\mathbf{q}) + \mathbf{J}\delta\mathbf{q} + O(\delta\mathbf{q}^2) = 0 \tag{2.21}$$

where \mathbf{J} is the Jacobian of the equation system. The solution to be solved for every iteration step is then:

$$\mathbf{J}\delta\mathbf{q} = -\mathbf{F}(\mathbf{q}) \tag{2.22}$$

where the solution of the equation is $\delta\mathbf{q}$. For every step the source strength on the right hand side is $\mathbf{q}_{new} = \mathbf{q}_{old} + \delta\mathbf{q}$.

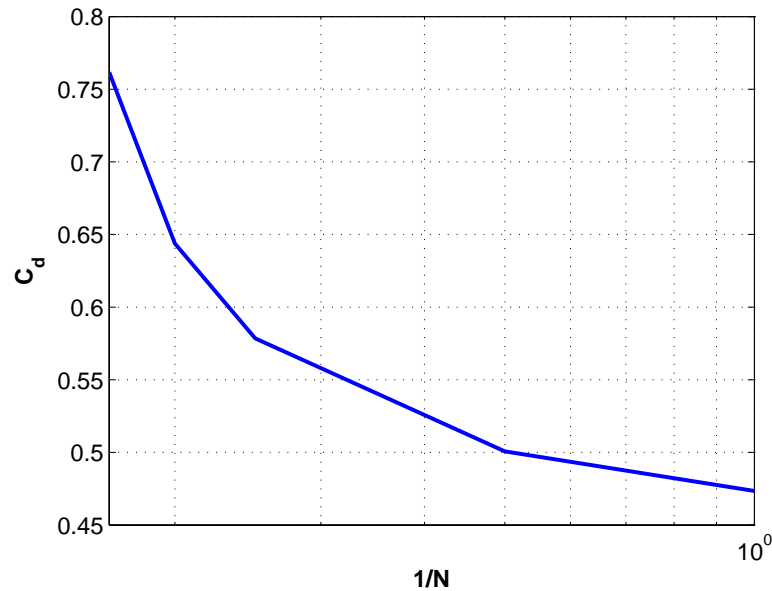


Figure 2.2: Net drag coefficient (-) for a square net with 2x2 twines and without knots, as a function of no. of elements. Uniform flow perpendicular to the net plane.

2.6 Convergence

If the number of sub elements which each of the twine elements are divided into (refer to Subsection 2.1 and Figure 1.12) are increased, it is expected that the result should converge towards an asymptotic value, as the system is more accurately described. As previously mentioned, at first the model only included the twines. This actually led to a divergence in the result as the number of sub elements increased. This is shown in Figure 2.2, where the net drag coefficient for a simple square net with 2x2 twines increase as the number of sub elements along the twines are increased. While increasing the number of sub elements, the size of each sub element decreases. Then at the corners (the knots) where the twines intersect, the distance between the center of the elements and thereby the distance between the singularities in to the source formulation, become very small. This led to large influences between the elements and the results actually diverge.

While adding the knot elements to the description, allowing for modeling the knots, this problem is solved. The twine elements and thereby the singularities in the corners, will then be separated by the physical size of the knot element. In Figure 2.3 results with the knots included are presented. As seen the results for the net drag coefficient for the net are converging as the number of elements is increased. In Figure 2.4 similar results are presented for a net with a 5x5 twines. For all these calculations a drag coefficient of 1.2, a diameter of 0.3 [m] for both the twines and the knots and an uniform velocity of 1.0 [m/s] is used. The results are non-dimensionalized with by dividing the drag force with

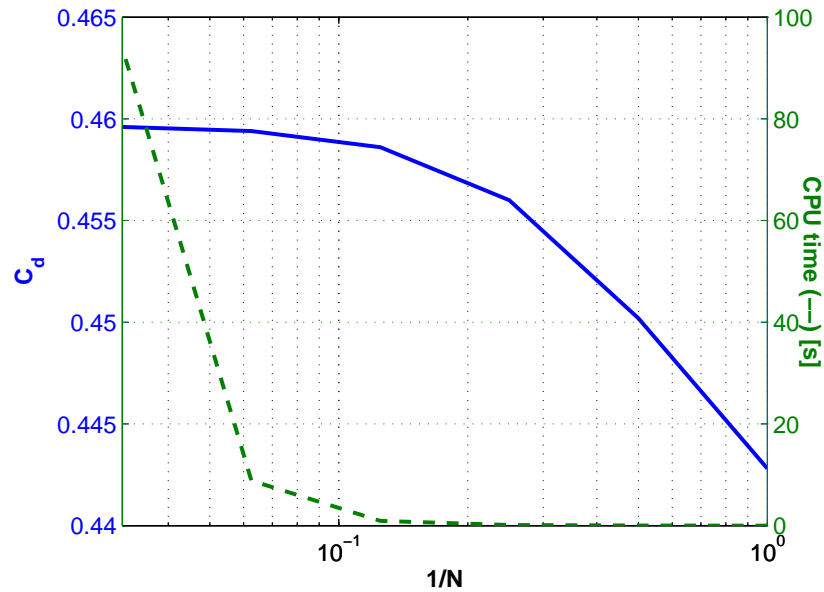


Figure 2.3: Net drag coefficient (-) and CPU time (- -) for a square net with 2x2 twines and with knots, as a function of no. of elements. Uniform flow perpendicular to the net plane.

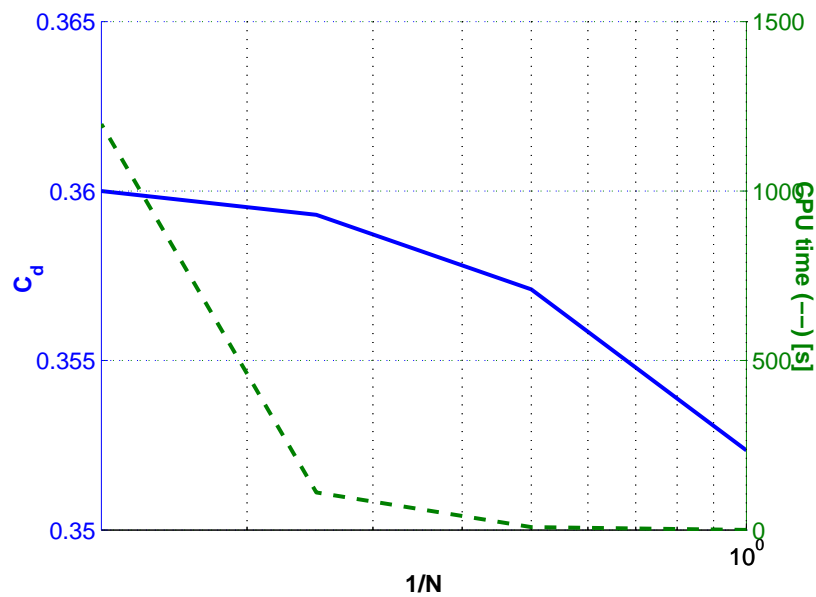


Figure 2.4: Net drag coefficient (-) and CPU time (- -) for a square net with 5x5 twines and with knots, as a function of no. of elements. Uniform flow perpendicular to the net plane.

$0.5\rho A U_\infty^2$, where A is the enclosed area of the net.

It is also noted from Figures 2.3 and 2.4 that the CPU time increase dramatically with increasing number of elements. Due to the iterative solution procedure described in Section 2.5 the CPU time is proportional with N^3 . Thus an alternative description of the source distribution $q(\chi)$ has been sought. The idea is that by using a more complex description of the source distribution, less sub elements is needed and hopefully the required CPU time will decrease.

2.7 Non-discrete modeling

Motivated by the shape of the discrete source distribution presented in Figure 2.5 for the twine elements and Figure 2.6 for the knot elements, two different approaches have been tried out, to represent the source distribution over the net as a Fourier series and as a B-splines distribution. The idea was to represent the source distribution across the complete twine (not divided into sub elements) and possibly even the complete net structure, described only by a few parameters.

Then instead of assuming constant source strength over each individual twine element, the source distribution along each complete twine could be on the following form:

$$q(\chi) = a_0 + \sum_{n=1}^{\infty} (a_n \cos(nx) + b_n \sin(nx)) \quad (2.23)$$

This is a standard Fourier series representation and can be found in standard mathematical textbooks, like for instance Kreyszig (1993). In this type of expression it is not the unknown $q(\chi)$ which are sought, but the unknown coefficients a_n and b_n . Further, it could also be possible to use one single two dimensional Fourier series to describe the source distribution over the net plane:

$$q(\chi, \eta) = a_0 + \sum_{m=1}^{\infty} \sum_{n=1}^{\infty} (a_{mn} \cos(mx) \cos(ny) + b_{mn} \sin(mx) \sin(ny)) \quad (2.24)$$

Another similar and possible approach could be to represent the source distribution by using B-splines.

$$P(t) = \sum_{i=1}^{n+1} B_i N_{i,k}(t), \quad t_{min} \leq t < t_{max}, \quad 2 \leq k \leq n+1 \quad (2.25)$$

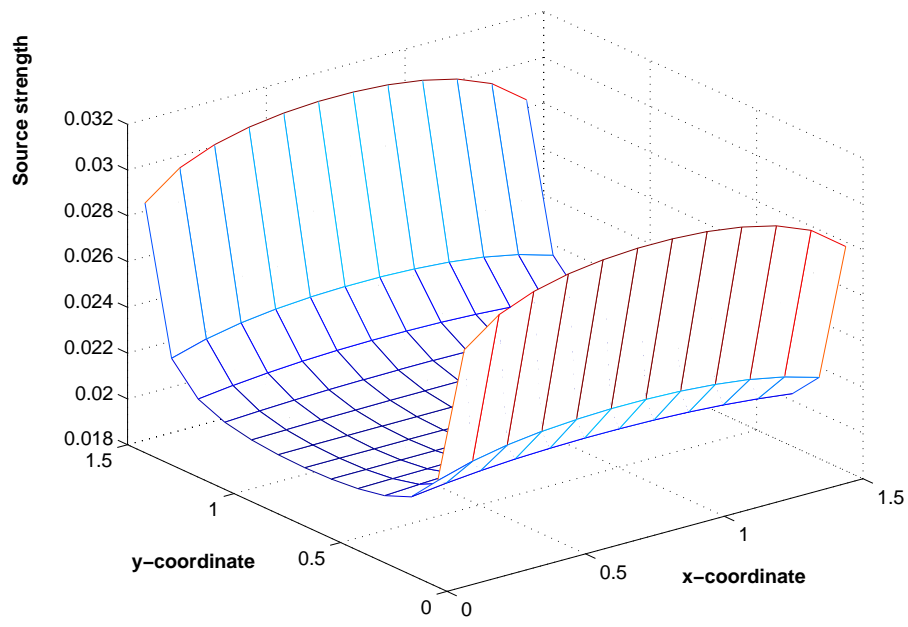


Figure 2.5: Source strength distribution for the twine elements along the twines parallel to the y-axis. A net made up of 13 by 13 twines is used.

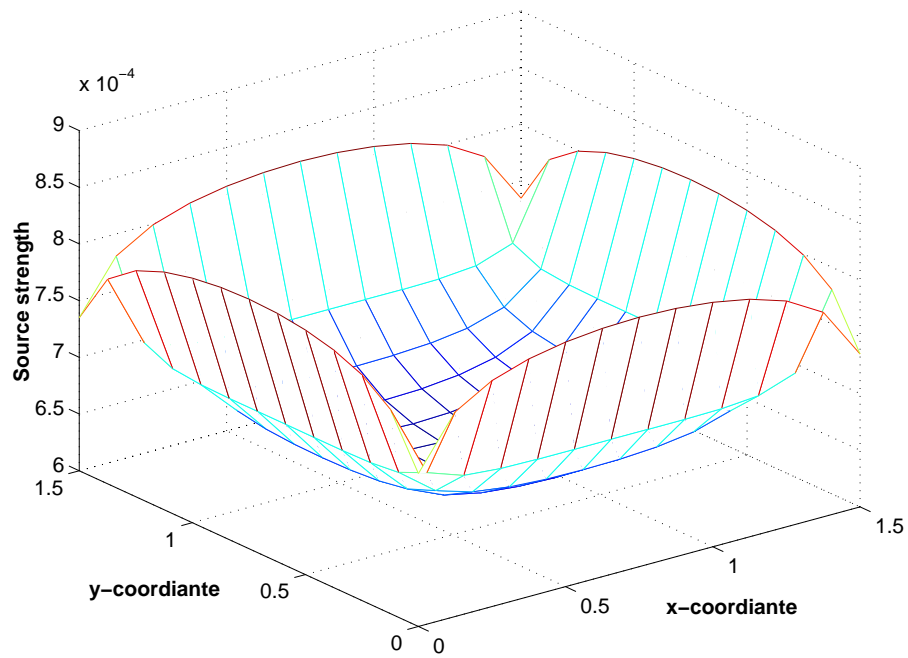


Figure 2.6: Source strength distribution for the knot elements. A net made up of 13 by 13 twines is used.

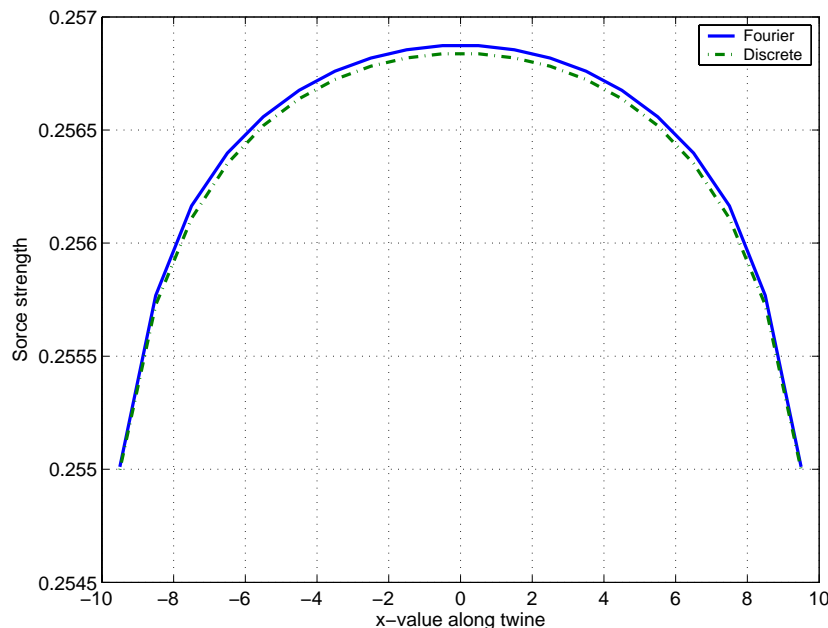


Figure 2.7: Comparison between Fourier and discrete solution of the source strength. The solution is based on 20 discrete elements and 6 Fourier components.

Equation (2.25) shows the basic formulation of a B-spline. $P(t)$ is the position vector along the B-spline curve as a function of the parameter t , B_i are the position vector of the $n + 1$ defining polygons vertices and $N_{i,k}$ are the normalized B-spline basis functions. A good textbook describing the principle behind B-splines is Rogers & Adams (1990). This approach has been used in other marine hydrodynamic application with success (e.g. Maniar 1995), to be able to solve complicated problems in a robust and efficient manner.

In Figure 2.7 a comparison between the discrete distribution using 20 elements and the source strength represented by a 6 component Fourier series is shown. The physical size of the net is 20 by 20 [m], which is modeled using 21 by 21 twines, with a diameter of 0.05 [m]. The drag coefficient is 1.0 and the magnitude of the uniform flow is 1.0 [m/s]. As seen there is a good agreement between the two solutions.

The downside is that it is no longer possible to solve the integral for the velocities analytically, but rather it has to be solved by numerical integration. So even though it is possible to get a good representation of the source distribution using the Fourier series representation with significantly fewer unknowns, due to the numerical solution of the integrals needed to solve Equation (2.10), (2.11) and (2.12), the overall task become more time consuming. Thus the discrete formulation is preferred.

2.8 Verification of the upstream model

2.8.1 Numerical analysis

The proposed method is dependent on two main parameters, the Solidity ratio and the Reynolds number. The Solidity ratio is a function of the physical dimensions of the net structure, including the diameter of the twine and knots. The Reynolds number is also dependent of the diameter of the twines and knots, but also on the inflow velocity. In addition the Reynolds number determine the appropriate drag coefficient of the twine and knot to use (Figure 1.10). Thus the resulting flow field and the net drag force is both depending on the physical dimensions of the net structure and the fluid velocity it self. Simplified this relation can be expressed as follows:

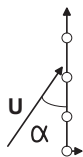
$$F_{Dnet} = f(C_d(d, U), d, U^2) \quad (2.26)$$

$$U = f(C_d(d, U), d, U) \quad (2.27)$$

Due to the functional dependency of fluid velocity as seen in Equation (2.27), the net drag force has a non-linear dependency of the drag coefficients and the diameters of the twines and knots. Further, the four parameters, diameter of the knot, diameter of the twiner, drag coefficient of the knot and drag coefficient of the twine all directly influence the drag force, but also the flow field and thereby the inflow velocity, by which the drag force is quadratically dependent.

As discussed in Section 1.3 there is no uniform relation between the drag force and the Solidity ratio for a net structure. This non-uniform relation is partly due to the Reynolds dependency of the drag coefficient for the individual parts of the net, i.e. the knots and the twines, as seen i Figure 1.10. But as discussed, it is also likely that there is a flow interaction between the different parts which make up the net. This interaction has an increasing importance with increasing Solidity ratios and contributes to the non-uniform relation between the drag force and Solidity ratio.

It could be expected that this interaction effect is due to the interaction that can occur between parallel cylinders in free flow. Even for a relatively high Solidity ratio, say $Sn = 0.5$, any parallel twines will be several diameters a part and will be too far apart to influence each other (Zdravkovich 1985). Thus an influence of the flow due to interaction between parallel twines will not occur when the angle of attack, α (definition in margin and Figure 1.5), is larger than approximately 30 [deg] (this is further discussed in Section 3.2). This lead to the conclusion that the main factor that contribute to the non-uniform relation between the net drag coefficient and the Solidity ratio, is an interaction effect related to the knot part.



The assumed increased in the net drag force due to the knot part of the net, is also

supported by results presented in Hoerner (1965). Hoerner indicates that an increase in the drag force, called interference drag, occur due to corners and junction between struts. This interference drag can give an increase in the drag force of up to 20 – 30% and is dependent both on the shape of the structure and the Reynolds number. Further, the relative area of the knot part compared to the total projected area of the net will increase with increasing Solidity ratio. Thus an increasing influence on the drag force is expected.

Two aspects are to be considered. First the drag force on the knot part as an individual element of the net structure and how to account for this based on its shape and physical dimensions. And secondly how the knot part influences the inflow condition and thereby all other elements of the net structure. To account for the influence on the flow due to the knot part, the knot is modeled as a sphere, and handled in the same matter as a twine element.

Both the physical size of the knot part and its drag coefficient is given as an input to the numerical model presented. The diameter of the sphere needs to reflect the physical properties of the net, and will likely be in the $O(150-200\%)$ of the diameter of the twine. It is not clear what values of the drag coefficient to use for the knot part. According to Figure 3.26 in Hoerner (1965) the drag coefficient for a three-dimensional circular and square plate, at Reynolds number between $10^2 - 10^6$, changes from approximately 2.0 to 1.17 with a local maximum of approximately 3.0. Similar the drag coefficient of a three-dimensional cube at Reynolds numbers between $10^4 - 10^6$ is 1.05. Further, the drag coefficient of a blunt body is largely dependent on any possible rounding radius of its shape. Justified by this discussion and the numerical results presented, depending on the Solidity ratio and geometry of the knot part, it could be correct to use a drag coefficient in the range of 1.0 – 2.0 when modeling the knot part as sphere.

For the twine, either looked up on as a stranded wire or as a cylinder, it is possible to find suitable experimental results for appropriate drag coefficients. According to Hoerner, with a suitable rounding radius, the drag coefficient for a two-dimensional blunt body drops to the level with a circular cylinder. Thus using a circular cylinder is most likely a good approximation for the twines.

2.8.2 Results for plane nets at 90 [deg] angle of attack

The proposed model are sought verified against the experimental results by Rudi et al. (1988) as presented in see Section 1.3 (Figure 1.7, 1.8 and 1.9). Numerical results for the total drag force of a plane net as function of the Solidity ratio, angle of attack and Reynolds number are presented.

In Figure 2.8, 2.9 and 2.10 the experimental results by Rudi et al. (1988) for $Sn = 0.130$,

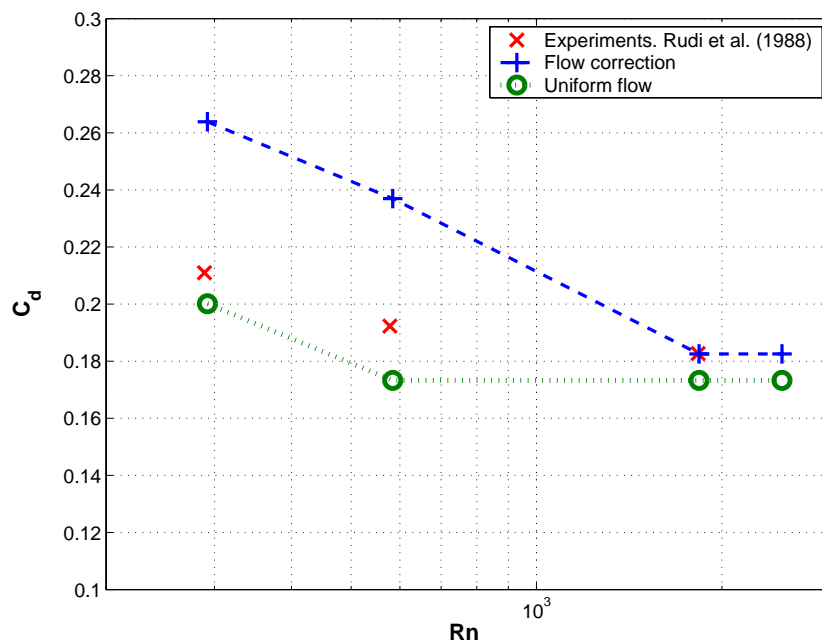


Figure 2.8: Drag coefficient for a plane net with $Sn = 0.130$ as a function of Reynolds number (with respect to the twine diameter d_t) at 90 [deg] angle of attack. The knot diameter is equal to 150% of the twine diameter, C_{dt} for the twine is Rn dependent and C_{dk} for the knot is 1.5.

$Sn = 0.243$ and $Sn = 0.317$ are presented together with different numerical results for the drag coefficient of a plane net. The results are presented as non-dimensionalized drag force coefficients, C_{dnet} , by dividing the drag force with $0.5\rho AU_\infty^2$, where A is the enclosed area of the net. These numerical results are obtained by calculating the drag as a sum of the drag of equivalent cylinders and spheres and as a sum of the drag of equivalent cylinders and spheres, including upstream correction. Dimensions used for the numerical models were half mesh size $\lambda = 75.0 [mm]$ and twine diameter $d_t = 4.8 [mm]$, $d_t = 9.1 [mm]$ and $d_t = 11.9 [mm]$ for $Sn = 0.130$, $Sn = 0.243$ and $Sn = 0.317$, respectively.

Due to the non-uniform relation between the drag force on the net and the Solidity ratio the different methods gives variable agreement with the experiments, depending on the Solidity ratio. For $Sn = 0.243$ the sum of the individual elements, with a drag coefficient for the knot part, $C_{dk} = 1.0$, and without any flow correction, gives good agreement. For $Sn = 0.13$, with, a higher $C_{dk} = 1.5$, the sum of the individual elements gives relatively good agreement. In both cases the flow correction over-predicts the results. Looking at Figure 1.11 this is expected since the ratio $R_{C_{dnet}}$ for both cases are not to far from 1.0 and it is closest to 1.0 for $Sn = 0.243$. And finally for $Sn = 0.317$, which have the lowest $R_{C_{dnet}}$ ratio, it is the results obtained with flow correction that gives the best agreement. This is not only expected by considering $R_{C_{dnet}}$, but also due to the fact the results for $Sn = 0.317$ is the most Reynolds number dependent and thus a flow interaction model is

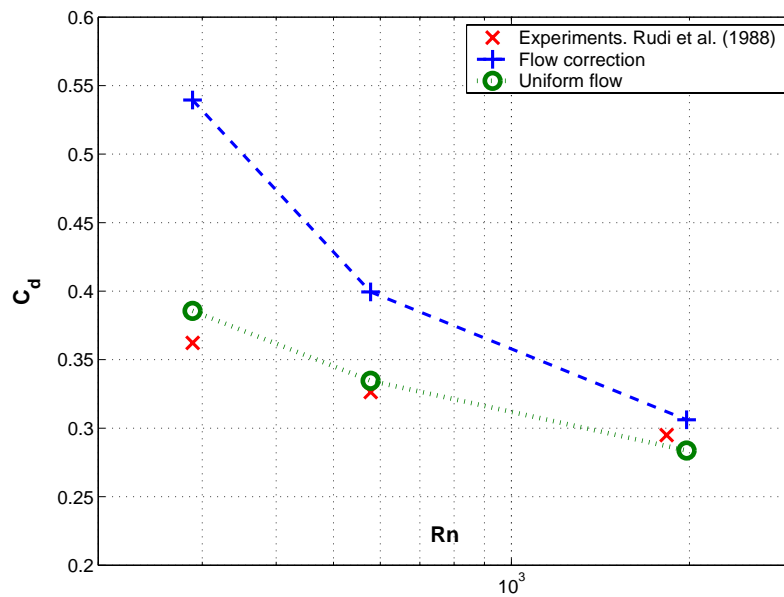


Figure 2.9: Drag coefficient for a plane net with $Sn = 0.243$ as a function of Reynolds number (with respect to the twine diameter d_t) at 90 [deg] angle of attack. The knot diameter is equal to 150% of the twine diameter, C_{dt} for the twine is Rn dependent and C_{dk} for the knot is 1.0.

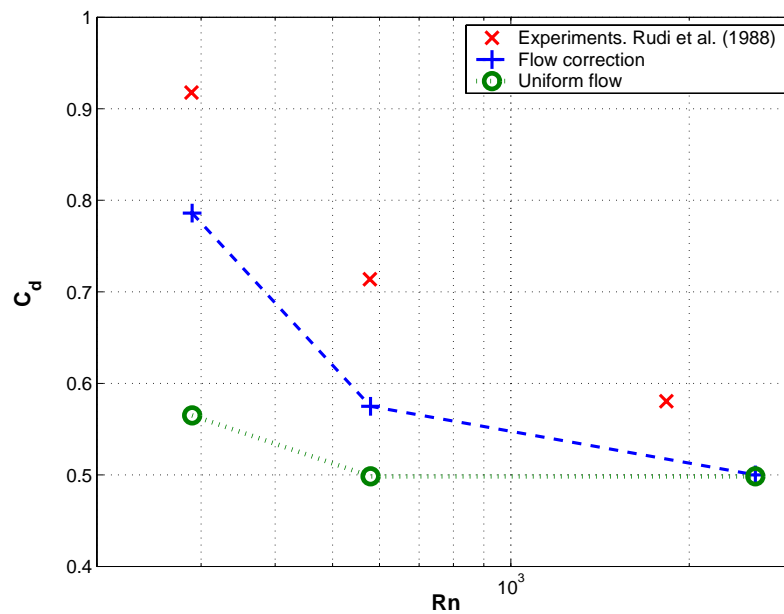


Figure 2.10: Drag coefficient for a plane net with $Sn = 0.317$ as a function of Reynolds number (with respect to the twine diameter d_t) at 90 [deg] angle of attack. The knot diameter is equal to 150% of the twine diameter, C_{dt} for the twine is Rn dependent and C_{dk} for the knot is 2.0.

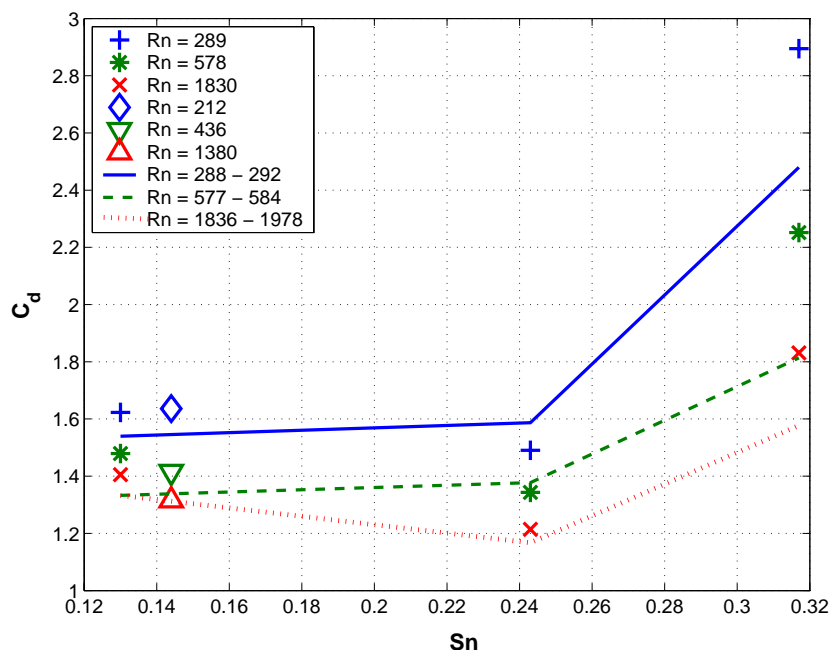


Figure 2.11: Drag coefficient for a plane net with at different Reynolds numbers (with respect to the twine diameter d_t), as a function of Solidity ratio at 90 [deg] angle of attack. Markers indicate experimental results (Rudi et al. 1988) and lines numerical results.

expected to give better results.

In Figure 2.11 the experimental results by Rudi *et al.* are plotted together with the same numerical results as in Figure 2.8, 2.9 and 2.10. The results are presented as non-dimensionalized drag force coefficients, C_{dp} , by dividing the drag force with $0.5\rho A_p U_\infty^2$, where A_p is the projected area of the net. For $Sn = 0.13$ and $Sn = 0.243$ it is the results based on uniform flow which are shown and for $Sn = 0.317$ the results with upstream correction. Presenting the results by non-dimensionalized with the projected area, A_p , instead of the enclosed area, A , removes the inherited Solidity ratio dependency of the drag coefficient, C_{dnet} . It is clear from the figure that at a certain Solidity ratio, there is a strong increase in the drag force. At the same time it seems like the drag coefficient, C_{dp} , tend towards an asymptotic value, when $Sn \rightarrow 0$, independent of Solidity ratio. The Reynolds dependency of the drag force is also decreasing, as previously commented. Unfortunately results for lower and higher Solidity ratios are not available. This could contribute to a better understanding of the physics involved.

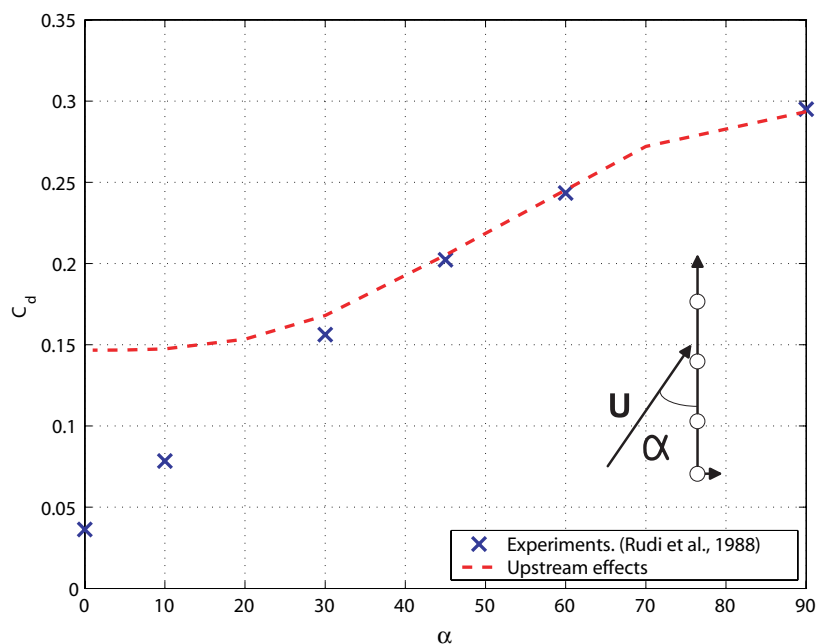


Figure 2.12: Drag coefficient for a plane net as a function of angle of attack, α (definition in figure). The Solidity ratio of the net is 0.243.

2.8.3 Results as a function of angle of attack

In Figure 2.12 the non-dimensional net drag force at different angles of attack is presented. The results by Rudi et al. (1988) are based on the same assumptions as described earlier, with the dependency of angle of attack also derived from experiments. The results presented here are based on a net with a Solidity ratio of 0.243, a drag coefficient for the twines and knots of 1.0 and the magnitude of the uniform velocity, $U_\infty = 1.0$ [m/s]. The results are non-dimensionalized using $0.5\rho A U_\infty^2$ using the enclosed area, A , of the net. Thus the net drag coefficient are dependent on the angle of attack.

The numerical results are obtained using the presented upstream model. The curve representing the numerical results is fitted to the experimental results at the 90 [deg] angle of attack. The argument for this is to make it easier to study the change in the trend for the net drag coefficient between the numerical and experimental results as a function of angle of attack, and not the absolute value of the drag force.

From the results it is evident that the asymptotic value for the results including upstream effects, when the angle of attack approaches zero, is approaching a non zero value which is much larger than the experimental result. This asymptotic value is approximately equivalent to the sum of the drag on each of the vertical cylinders modeling the vertical twines of the net with no correction of the inflow velocity on the elements. The drag on the

horizontal twines of the net will be equal to zero, since the decomposed velocity vector in the local coordinate system of the horizontal twine elements will be equal to zero.

Down to an angle of attack of approximately 25 [deg] the trend compare relatively well, but at lower angles the two curves divide. The reason for this is clear, since there is nothing in the existing model that account for the flow reduction that will occur in the wake behind a cylinder in free flow. When one cylinder is situated in the wake of another, there will be a reduction in the inflow velocity on the preceding cylinder, and thereby a reduction in the drag force. Thus it is clear that it is necessary to include a model of the velocity in the wake behind the different parts of the net, when the net is situated at an angle of attack different from 90 [deg].

A model that accounts for the reduced inflow due to the velocity deficit in the wake behind a cylinder in flow and the added effect of several cylinders situated in a row behind each other with respect to the inflow direction is presented in the next chapter. This model is based on the formulation by Schlichting (1968) and is modified to account for the added effect of several cylinders in the flow field and their individual position in the generated wake field.

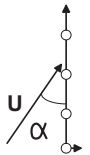
Another aspect that will most likely have an effect for a flexible net structure exposed to current load is the deformation of the net structure. Due to the nature of a net structure, it will not be possible during experiments to avoid some deformation of the net itself, which again will not only have an influence on inflow of the net and thereby the resulting drag force, but also on the “effective” angle of attack. Deformation of the net has not been accounted for so far, but will be introduced in later chapters.

CHAPTER 3

Modeling downstream effects

3.1 Introduction

In a two-dimensional net at low angles of attack (Definition in Figure 1.5 and figure in margin) or in a three-dimensional net structure, the different parts or twines of a net will be situated downstream of each other. This will create a situation with possible shadow effects. Thus when different parts of a net structure is situated downstream of each other, the velocity deficit in the wake due to the separated flow around each twine, could be an important factor that it is necessary to account for. In this chapter the focus will be on elements of the net structure in the wake of each other. The objective is to develop simplified and physically justified methods. To proceed, a wake formulation which is possible to combine with and implement in to the existing potential flow model, is needed.



As already describe, the Reynolds number is an important factor while describing the flow around a circular cylinder and inside and around a net structures. The flow field can be categorized by the Reynolds number and be divided into different regimes according as presented in Figure 3.1. Typical Reynolds number range for a net structure, with respect to the diameter of a twine, is typically $O(10^2 - 10^4)$. Thus normally in the subcritical regime, with a completely turbulent wake.

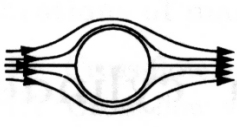
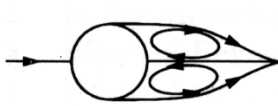
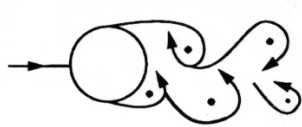
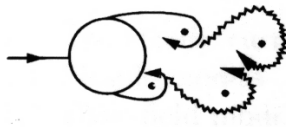
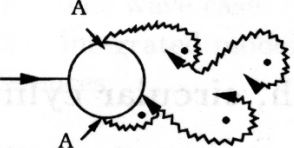
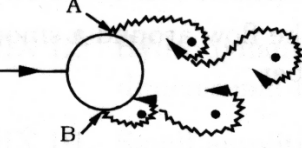
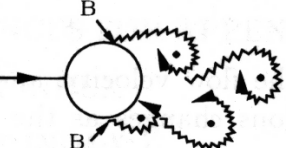
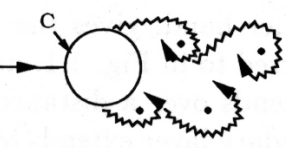
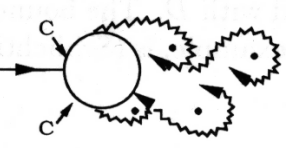
a)		No separation. Creeping flow	$Re < 5$
b)		A fixed pair of symmetric vortices	$5 < Re < 40$
c)		Laminar vortex street	$40 < Re < 200$
d)		Transition to turbulence in the wake	$200 < Re < 300$
e)		Wake completely turbulent. A: Laminar boundary layer separation	$300 < Re < 3 \times 10^5$ Subcritical
f)		A: Laminar boundary layer separation B: Turbulent boundary layer separation; but boundary layer laminar	$3 \times 10^5 < Re < 3.5 \times 10^5$ Critical (Lower transition)
g)		B: Turbulent boundary layer separation; the boundary layer partly laminar partly turbulent	$3.5 \times 10^5 < Re < 1.5 \times 10^6$ Supercritical
h)		C: Boundary layer com- pletely turbulent at one side	$1.5 \times 10^6 < Re < 4 \times 10^6$ Upper transition
i)		C: Boundary layer comple- tely turbulent at two sides	$4 \times 10^6 < Re$ Transcritical

Figure 3.1: Regimes of flow around a smooth circular cylinder in steady current. (Sumer & Fredsøe 1997).

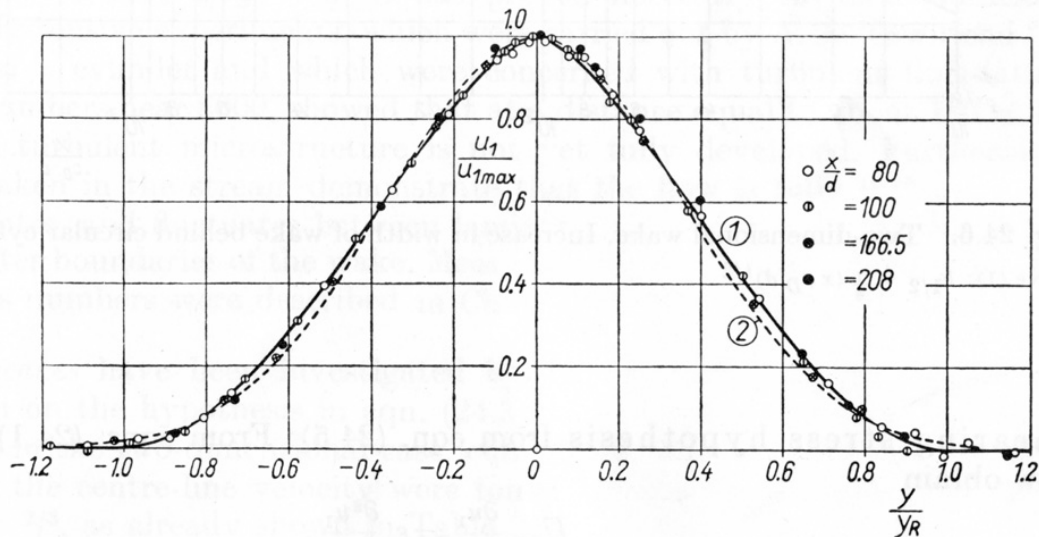


Figure 3.2: Experimental (dots) and numerical (solid and dashed) results by Schlichting (1968).

There exist different mathematical models which in a quantitative fashion describe the wake behind a cylinder. Roughly these can be divided into laminar and turbulent models and are often of a very complex nature and based on the Navier-Stokes equations. Using an approach like this, calculating the wake behind the twines in a net structure (or every cylinder in the model) using Navier-Stokes equations, would be nearly impossible due to the required CPU time and data storage. Further, CFD methods for this type of a flow in combination with a net structure have clear physical limitations, due to for instance the non-uniform surface of the twines. Thus using a detailed and time consuming CFD method seem inexpedient.

One possible model for calculating the velocity deficit behind one cylinder is the well known “far wake mean velocity deficit” model presented by Schlichting (1968). This is a model which as a function of x - and y -coordinates (the x - axis pointing in the flow direction and the y - axis perpendicular to the body axis) give the mean velocity in the wake behind a body. Schlichting’s formula agrees well with experiments in the far-field wake, but gives too large velocity deficits and a too narrow wake region in the near-field wake. Far field is typically a distance of 80 – 100 diameters downstream. Results from the experiments and calculations by Schlichting are presented in Figure 3.2.

In Figure 3.3 an illustration of several cylinders situated downstream of each other is shown, together with the definition of the spacing, s , between two cylinder axis or twines. Typically two twines could be situated only a few diameters, d , apart, say typically $s = 5d$. Thus to be able to get good results in the near-field wake, which is the range of interest

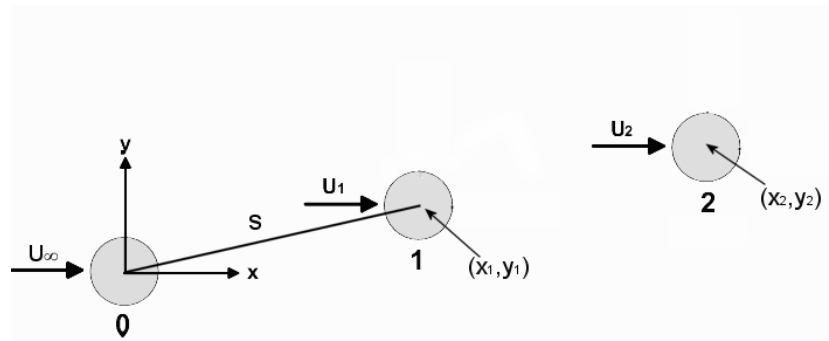


Figure 3.3: Illustration of several cylinders in a wake flow. s is the distance between two cylinder axis. .

in this case, different modifications of the original formulation have been tried out. In addition the problem involves not only the wake behind one cylinder, but several cylinders which in principle is “randomly” placed in the wake of each other. It is not apparent how to sum the contributions from each of the cylinders into one velocity deficit, relevant for the influence in the downstream cylinders. This is discussed further in Section 3.4.

The calculated inflow velocity at each of the cylinders will be used to calculate the drag force on the cylinder or the system of cylinders making up the net structure. Due to limited numerical results related to velocity deficit in wakes behind several cylinders, verification of the different numerical results will be done using the drag force. Verification will be sought using both a few number of cylinders and plane net structures.

To further investigate the near field velocity deficit, two different experiments have been conducted. First five rigid equidistant aluminum cylinders in a row, was towed at different angles of attack, velocities and spacings between the cylinders. The total in-line and perpendicular force on the grid were measured. The diameter of the cylinder were $d = 4.0$ [cm] and they were towed with a draught $h = 0.8$ [m] and a speed of $0.2 - 1.0$ [m/s]. The experiment is presented in Section 3.3.

Secondly a small set-up was made, to study the flow field around a cylinders situated in the wake of another cylinder. The flow field were visualized an filmed. No measurements were conducted. Further description in Section 3.5.

3.1.1 Forces on a circular cylinder

The forces acting on the cylinder in the in-line direction can be divided into friction force and pressure force (form drag). The time integrated lift force averaged over a cycle $[0, 2\pi]$,

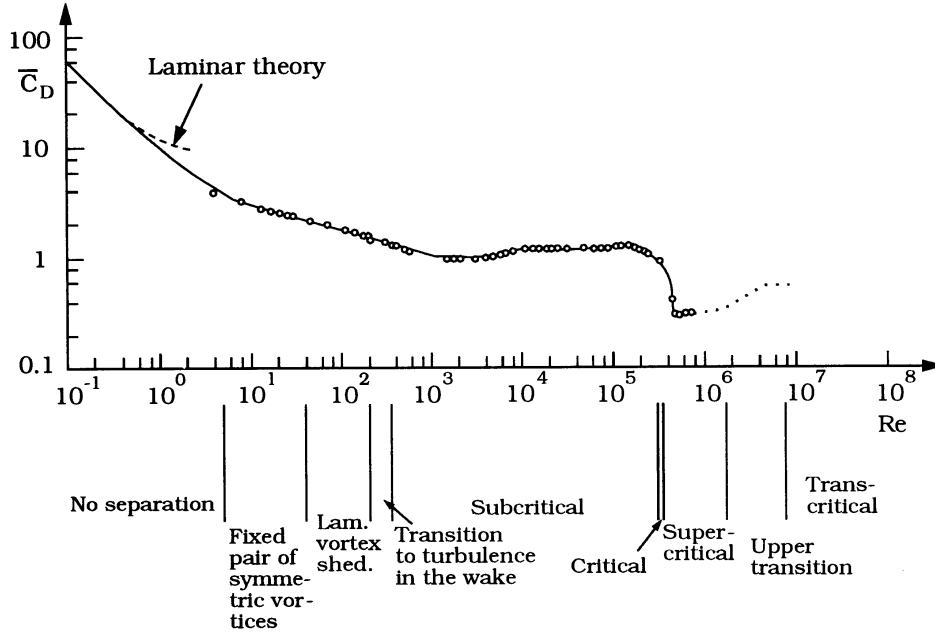


Figure 3.4: The drag coefficient of a circular cylinder as a function of flow regimes and Reynolds number with respect to cylinder diameter. (Sumer & Fredsøe 1997).

will be equal to zero. The general expression for the in-line mean drag force, F_D , is

$$F_D = \int_0^{2\pi} (\bar{p} \cos(\phi) + \bar{\tau}_0 \sin(\phi)) r_0 d\phi \quad (3.1)$$

By making the expressions non-dimensional the equation can be written in the following form

$$\frac{F_D}{1/2d\rho U^2} = \int_0^{2\pi} \left[\left(\frac{\bar{p} - p_0}{\rho U^2} \right) \cos(\phi) + \left(\frac{\bar{\tau}_0}{\rho U^2} \right) \sin(\phi) \right] d\phi \quad (3.2)$$

since both the pressure and the friction part of the force is dependent on the Reynolds number, it is then possible to express the non-dimensional mean drag force as a Reynolds dependent drag coefficient, denoted C_d .

This lead to the well-known expression

$$F_D = \frac{1}{2} \rho C_d(Rn) d U^2 \quad (3.3)$$

where the drag coefficient has a complex functional relation with the flow regime and Reynolds number. This relation is illustrated in Figure 3.4.

3.1.2 The far wake mean velocity deficit model

In relation to studies of free turbulent flow, Schlichting (1968) derived an expression for the mean velocity deficit in the far wake. Free turbulent flow is defined as turbulent flow not confined by any solid walls and is divided into free jet boundaries, free jets and wakes. A wake is formed behind a body which is being dragged through fluid at rest, or behind a body which has been placed in a stream of fluid. There will be a drag force acting on the body, which in turn is related to a loss of momentum, and i.e. the velocities in the wake region becomes smaller than in the uniform flow.

Since the region in which a solution is sought do not extend far in a transversal direction relative to the main direction of the flow, and that the transverse gradients are large, the problem can be view as being of a boundary layer nature. For a two-dimensional incompressible flow, the boundary layer equations are (two-dimensional Navier-Stokes equations:

$$\frac{\partial u}{\partial t} + u \frac{\partial u}{\partial x} + v \frac{\partial u}{\partial y} = \frac{1}{\rho} \frac{\partial \tau}{\partial t} \quad (3.4)$$

$$\frac{\partial u}{\partial x} + \frac{\partial v}{\partial y} = 0 \quad (3.5)$$

τ denotes the turbulent shearing stress and is important for the development of the simplified equations. The pressure term of the Navier-Stokes equations are removed with the argument that in the wake region far behind the body, as a first approximation, the pressure will remain constant.

In order to be able to integrate the boundary layer equations, it is necessary to express the shearing stress in terms of the parameters of the main flow. To do this Schlichting used Prandtl's mixing length hypothesis. Based on two different descriptions of Prandtl's mixing length hypothesis, he could developed two models for the two-dimensional turbulent free wake behind a single body

$$\tau = \rho l^2 \left| \frac{\partial u}{\partial y} \right| \frac{\partial u}{\partial y}, \quad (3.6)$$

$$\tau = \rho \epsilon_\tau \frac{\partial u}{\partial y} = \rho \chi_1 b (u_{max} - u_{min}) \frac{\partial u}{\partial y} \quad (3.7)$$

where l is the mixing length, b denotes the width of the mixing zone, χ_1 is an empirical constant and ϵ_τ is the virtual kinematic viscosity. The virtual kinematic viscosity is assumed constant over the whole width and hence independent of y . Further based on certain assumptions the virtual kinematic viscosity also is independent of x and can be viewed as an empirical parameter denoted ϵ_0 .

Schlichting derived the following expression for the velocity deficit:

$$\frac{u_1}{U_\infty} = \frac{1}{4\pi} C_d d U_\infty \sqrt{\frac{\pi U_\infty}{\epsilon_0 x}} \exp\left(-\frac{y^2 U_\infty}{4\epsilon_0 x}\right) \quad (3.8)$$

Based on measurements, Schlichting suggested the following value for the empirical parameter ϵ_0 :

$$\epsilon_0 = 0.0222 U_\infty C_d d \quad (3.9)$$

By inserting Equation (3.9) into Equation (3.8) the velocity deficit behind a single cylinder in a turbulent wake can be written as

$$\frac{u_1}{U_\infty} = 0.95 \sqrt{\frac{C_d}{\left(\frac{x}{d}\right)}} \exp\left(\frac{-(\frac{y}{d})^2}{0.0888 C_d \left(\frac{x}{d}\right)}\right) \quad (3.10)$$

3.2 Modified models

The velocity in the wake behind a cylinder of diameter d , calculated using Equation (3.10) at different x/d values are shown in Figure 3.5. For the presented results, origin is located in the center of the cylinder, the x-axis is pointing in the flow direction and the y-axis is perpendicular to the cylinder axis, while d is the diameter of the cylinder. As mentioned this equation show good agreement for large x/d ratios, but at smaller ratios the model give to large velocity deficits and a to narrow wake region. To be able to get good results at smaller x/d ratios, but still do not have to solve the complete Navier-Stokes equations, different modifications of the original formulation have been tried out. In the following U_∞ is the undisturbed uniform flow in the positive x-direction, C_d is the drag coefficient, d the diameter and the cylinder axis corresponds to $x = 0$ and $y = 0$.

First four different modifications will be presented. Then the effect and results of the different modifications in addition to the original model by Schlichting, will be discussed. And one model will be selected for further verification and discussion.

3.2.1 Near field modification

Based on measurements in turbulent flow close to a cylinders, Pfeil & Eifler (1975) developed a modification of Schlichting's Equation (3.10). They based their development on the same assumptions as Schlichting and in brief ended up with a model for small distances where the constants in Equation (3.10) are modified with the following result

$$\frac{u_1}{U_\infty} = 0.919 \sqrt{\frac{C_d}{\left(\frac{x}{d}\right)}} \exp\left(\frac{-(\frac{y}{d})^2}{0.0949 C_d \left(\frac{x}{d}\right)}\right) \quad (3.11)$$

The reduction of the first constant result in a smaller velocity deficit, while the increase in the second constant give a more wider wake, which is a wanted effect.

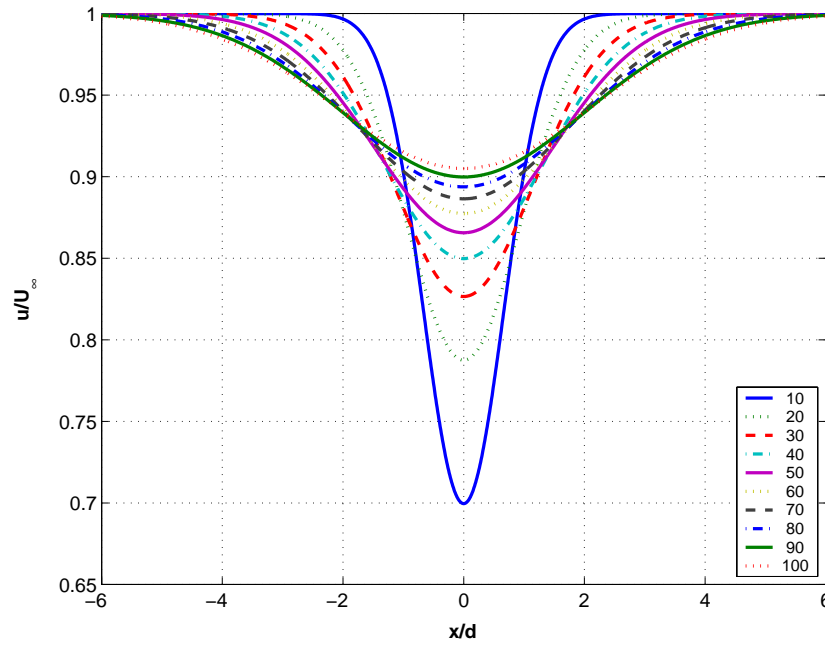


Figure 3.5: Velocity deficit downstream of a single cylinder calculated using Schlichting at different distances x/d downstream of the cylinder. Properties: $d = 1.0$ [m], $U_\infty = 1.0$ [m/s] and $C_d = 1.0$.

3.2.2 Virtual origin

Blevins (1990) also added a virtual distance to the formulation, naming it a virtual origin of the wake. Further the constants in Schlichting's formula were modified. The time-averaged velocity deficit u_1 in a turbulent wake behind a single cylinder according to Blevins, then becomes

$$\frac{u_1}{U_\infty} = 1.02 \sqrt{\frac{C_d}{6 + (\frac{x}{d})}} \exp\left(\frac{-(\frac{y}{x})^2}{0.0767 C_d (6 + (\frac{x}{d}))}\right) \quad (3.12)$$

Blevins presents a constant of 1.2 instead of 1.02 as used in Equation (3.12). However using conservation of fluid momentum and expressing the drag force in terms of C_d and u_1 , shows that this must be a misprint.

3.2.3 Two dimensional plane wake

In his PhD thesis, Løland (1991) investigated the wake behind a screen. By modifying the boundary condition at $x = 0$, to include the physical dimension of the cylinder Løland got the following requirement

$$u_1(x = 0, y) = C^* H(d/2 - |y|) U_\infty \quad (3.13)$$

Where H is the Heaviside function and has a value of 1 when the argument is positive and is equal to zero otherwise. The constant C^* is similarly to the previous constant C_1 , used in the derivation of the formulation by Schlichting, related to the drag on the body and the conservation of momentum. Thus at $x = 0$

$$F_D = \rho U_\infty \int_{-\infty}^{\infty} u_1 dy = \rho U_\infty \int_{-d/2}^{d/2} C^* H(d/2 - |y|) U_\infty dy = \frac{1}{2} \rho C_d d U_\infty^2 \quad (3.14)$$

and consequently

$$C^* = \frac{1}{2} C_d \quad (3.15)$$

Using this boundary condition together with the governing equations and derivation as in section 3.1.2, the following expression is obtained

$$u_1(x, w) = \frac{1}{2} \int_{-\infty}^{\infty} C^* \frac{\sin(wd/2)}{w} \exp\left(-\frac{w^2 \epsilon_0}{U_\infty} x\right) \exp(iwy) dw \quad (3.16)$$

Solving this integral for w , the velocity deficit behind a circular cylinder according to Løland becomes

$$\frac{u_1}{U_\infty} = \frac{C_d}{4} \left\{ \Phi \left(\frac{\frac{1}{2} + (\frac{y}{d})}{\sqrt{0.0888 C_d (\frac{x}{d})}} \right) + \Phi \left(\frac{\frac{1}{2} - (\frac{y}{d})}{\sqrt{0.0888 C_d (\frac{x}{d})}} \right) \right\} \quad (3.17)$$

where Φ is the error function

$$\Phi(z) = \frac{4}{\sqrt{\pi}} \int_0^z e^{-z'^2} dz' \quad (3.18)$$

3.2.4 Virtual source position

Huse (1992) introduced a “virtual source position” into the expression (3.10), which is actually an increase in the distance from a point in the wake to the origin of the wake. The origin is moved a distance x_v upstream of the cylinder, which is determined by the requirement that the width of the wake at the cylinder position (referred to the new origin) is equal to the diameter of the cylinder. This requirement leads to $x_v = 4d/C_d$. When this correction is inserted into Equation (3.10) the following result is obtained

$$\frac{u_1}{U_\infty} = 0.95 \sqrt{\frac{C_d}{(\frac{4}{C_d}) + (\frac{x}{d})}} \exp \left(\frac{-(\frac{y}{d})^2}{0.0888 C_d \left((\frac{4}{C_d}) + (\frac{x}{d}) \right)} \right) \quad (3.19)$$

At large x/d ratios the added distance x_v is small compared to the total distance, thus the correction do not violate the original behavior at large distances.

3.2.5 Effect of the different models

In Figure 3.6, 3.7 and 3.8, results from the different models are presented, with different combinations of the parameters, x/d and y/d . The drag coefficient $C_d = 1.16$ for all the numerical results. From Figure 3.6 it is evident that, compared to the original model by Schlichting, all the modified models have smaller velocity deficits and wider wakes, and further that there is a clear distinction between the three models, “Virtual origin”, “Virtual source position” and “Plane wake” which all alter the origin of the wake, and the two models, “Schlichting” and “Near field modification”, where only the coefficients of the equation are altered. It is also evident that among the modified models it is the “Virtual origin” by Blevins, that give both the largest velocity deficit and the widest wake.

Figure 3.7 show results for different x/d values along the x-axis, when $y/d = 0$. As the results illustrate, after approximately 20 diameters, there is nearly no difference between either of the models. All the models have the same asymptotic behavior and i.e. the original behavior of the model by Schlichting is not altered in the far wake region. From this figure it is also evident that the smaller the x/d , the larger is the differences between the five models, and especially between the models that alter the origin of the wake and the two other models. This is natural since the origin of the models are not the same and that the original model by Schlichting and the “Near field modification” will become singular at $x/d = 0$.

Figure 3.8 show numerical results for the different models as a function of x/d , for different y/d ratios. This figure further illustrates the two-dimensional behavior of the models. At $y/d = 0.25$ the velocity deficit is smaller for the modified models, while for increasing y/d , the velocity deficit becomes larger for the modified models, thus giving rise to a wider wake.

Based on these numerical results, the “Plane wake” (Løland 1991), “Virtual origin” (Blevins 1990), together with the original formulation by Schlichting (Schlichting 1968), is chosen for further analysis and discussion. The “Virtual origin” is chosen because it is the model which give both the largest velocity deficit and the widest wake. The “Virtual source position” (Huse 1992) have only slightly less velocity deficit and a more narrow wake than the “Virtual origin”. But the two models are also similar in its form. The “Virtual source position” is thus not considered for further discussion. The “Plane wake” have not as large velocity deficit, nor as wide a wake as the other two models, but it is derived in a different matter. Due to this is the “Plane wake” model consider to be interesting for further analysis and discussion. The formulation by Schlichting is chosen because it is the original model and is thus relevant as a reference.

At the end it is important to emphasize that all the presented numerical models are based on a far field approximation. Using them in a near field analysis is of course to stretch

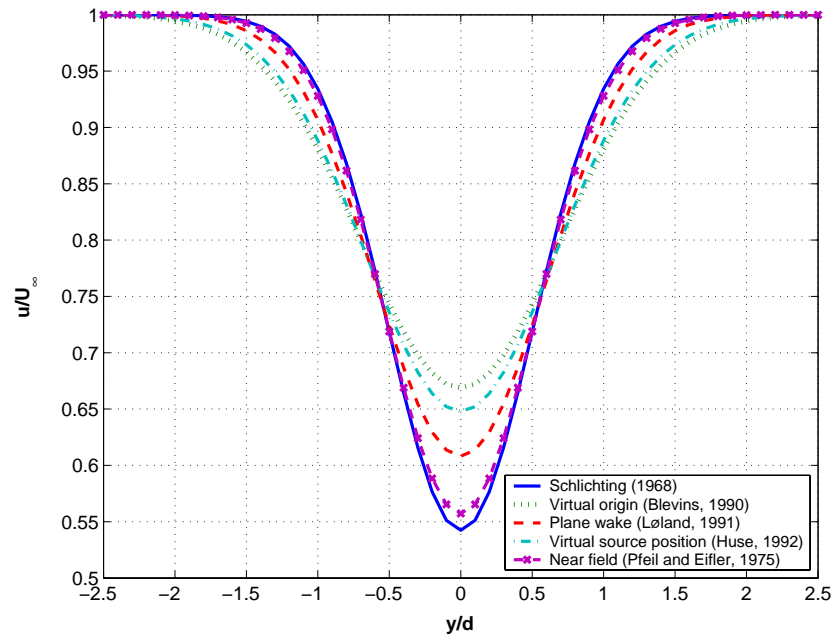


Figure 3.6: Velocity deficit downstream of a single cylinder calculated using different velocity deficit models. Properties: $x/d = 5$, $d = 4.0$ [cm], $U_\infty = 0.5$ [m/s] and $C_d = 1.16$.

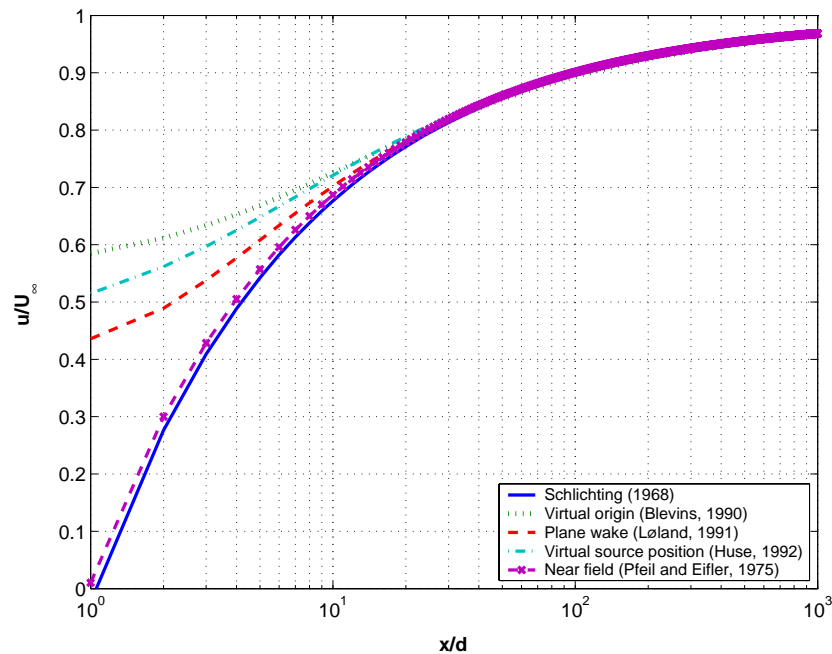


Figure 3.7: Velocity deficit downstream of a single cylinder, calculated using different velocity deficit models. Properties: $y/d = 0$, $d = 4.0$ [cm], $U_\infty = 0.5$ [m/s] and $C_d = 1.16$. Logarithmic x-axis.

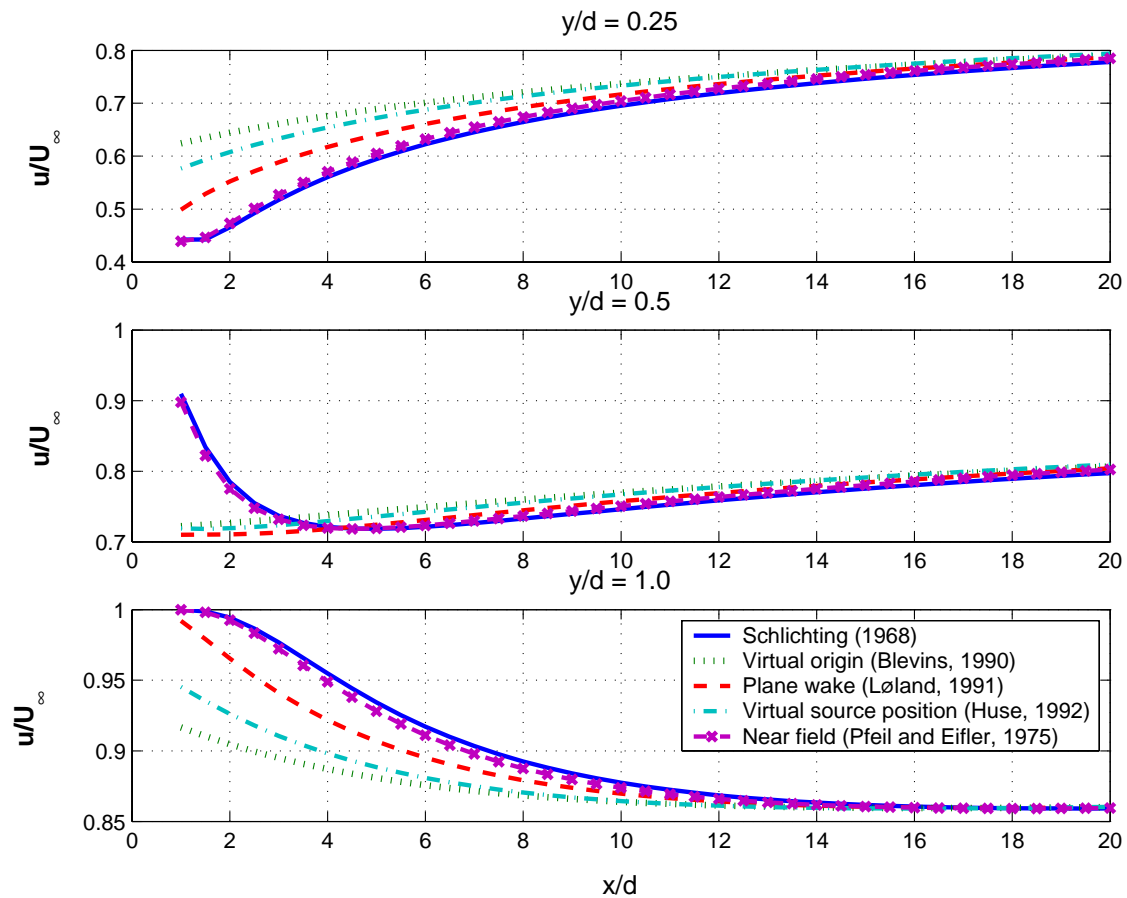


Figure 3.8: Velocity deficit downstream of a single cylinder at different y/d ratios, calculated using different velocity deficit models. Properties: $d = 4.0$ [cm], $U_\infty = 0.5$ [m/s] and $C_d = 1.16$. Note different scales on the y-axis.

their validity and therefore will evidently introduce uncertainties related to the answers obtained.

3.3 Experiments

3.3.1 Introduction

To verify the wake model used to calculate the velocity deficit behind several cylinders, an experiment was conducted to measure the total force acting on a set of cylinders inclined at different angles to the flow.

It was not possible to directly measure the velocity in the wake between the different cylinders, due to limitations in equipment and laboratory facilities. Instead the total force on the cylinders at different angles was measured and compared to the drag calculated by the different wake models.

3.3.2 Model setup

A model with five cylinders were used. The model and setup is shown in Figure 3.9. To measure the force on the row of cylinders, two strain gauges were used, situated at 90 degree angle to each other. The five vertical cylinders were attached to one horizontal cylinder. The middle vertical cylinder were fixed to the frame, while the other vertical cylinders could be moved along the horizontal cylinder, to allow for a horizontal variation of the spacing, s , between them. The model frame was attached to a towing carriage. The strain gauges were allowed to rotate with the cylinders such that one strain gauge would always measure the force along the horizontal cylinder. This direction is defined as 'in-line', while the direction perpendicular to the in-line direction is defined as the 'perpendicular' one.

The horizontal cylinder was 3.5 meter long and made of steel, while the vertical cylinders were made of aluminum. Dimensions for the vertical cylinders are presented in Table 3.1.

The experiments were carried out in a towing tank at the Marine Technology Center at the Norwegian University of Science and Technology (NTNU), in Trondheim, Norway. The properties for the towing tank is presented in Table 3.2.

Test program Three different parameters were changed during the experiment, the angle of attack α , the horizontal spacing s between two cylinder axis (definitions in Figure 3.3) and finally the towing speed U_∞ . Figure 3.3 gives an overview of the different combinations of parameters which were tested. The horizontal spacing is given as number of cylinder diameters d .

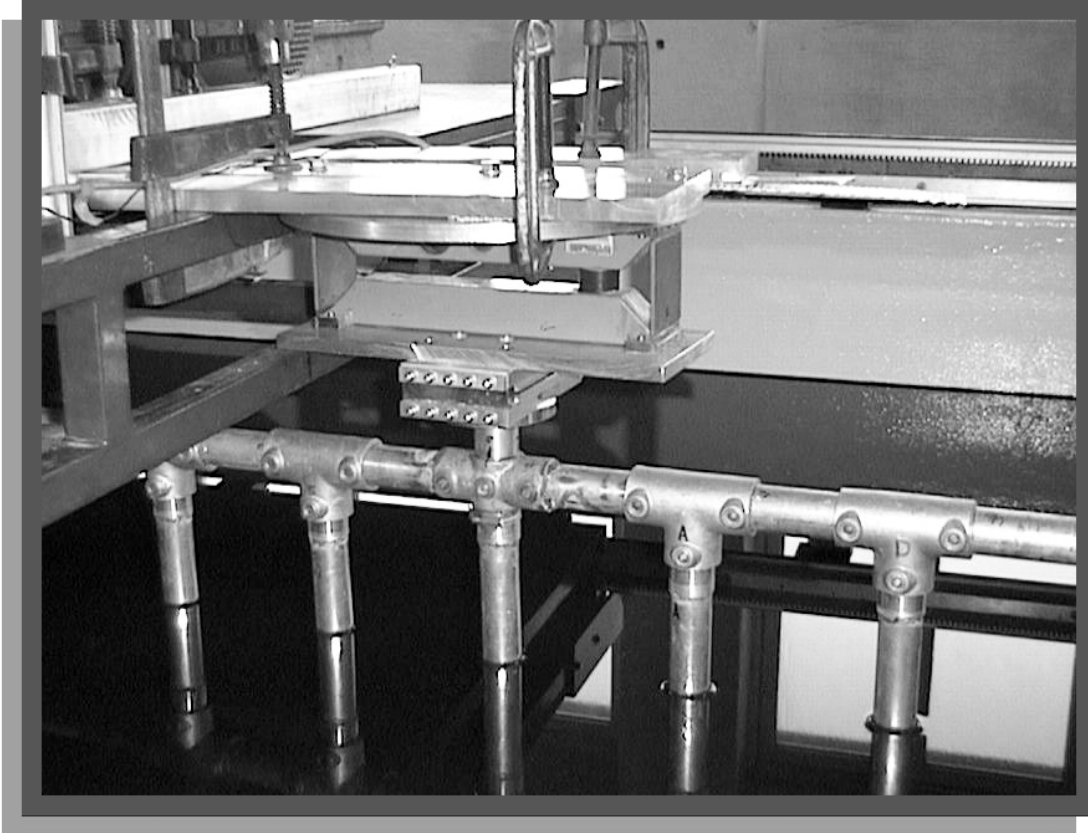


Figure 3.9: The experimental model and setup for measurements of forces on a row of cylinders.

Table 3.1: Dimensions for the vertical aluminum cylinders used in the experiment.

Height [m]	1.0	Draught [m]	0.8
Thickness [mm]	4.0	Diameter [cm]	4.0

Table 3.2: Properties for the towing tank.

Length [m]	25.0	Carriage type	Open bay
Width [m]	2.8	Driving motors	1 DC with gear
Depth [m]	1.0	Power system	Thyristor controlled
Wheel base [m]	3.0	Total weight [kg]	200.0
Max acceleration [m/s^2]	1.0	Speed range [m/s]	0.05 - 1.75

Table 3.3: Combination of parameters for the experiment.

Spacing s [-]	Towing speed U_∞ [m/s]	Angle of attack α [deg]
5	0.250	-5 ... 45, 90
	0.375	-5 ... 45, 90
	0.500	-5 ... 45
7.5	0.250	-5 ... 45, 90
	0.375	-5 ... 45, 90
	0.500	-5 ... 45, 90
	0.750	-5 ... 45, 90
10.0	0.375	0 ... 20, 35, 45, 90
	0.500	0 ... 20, 35, 45, 90

For each combination of the parameters were at least three runs conducted. The measurements were sampled at 100 Hz and the time series were later analyzed to give mean values for the velocity, the in-line force and the perpendicular force.

For the earliest tests an analog filter of 14 Hz where used on the signal. This filter was later removed, and no analog filtering where performed. The time-series has later been analyzed using digital filters.

The test for $s = 7.5d$ and some of the test done with $s = 5d$, were carried out with a gear ratio of 45 : 30 for the towing carriage. later it was noted that this gave an unsteady motion of the towing carriage. The gear ratio was changed to 15 : 60, which gave a more steady motion of the model setup during the experiments. Due to time limitations, it was not possible to redo the experiments for $s = 7.5d$.

Eigenfrequency of the model To determine the eigenfrequency of the system, a decay test was performed for the in-line and the perpendicular direction. The decay tests were conducted in water. The results were then analyzed by Fourier transformation to give the results presented in Figure 3.10 and Figure 3.11. As seen from the results, the eigenfrequency for the first vibration mode of the setup is equal to 6.8 Hz and 7.6 Hz, for the in-line and the perpendicular direction, respectively.

Strouhal numbers While measuring the forces on cylinders in flow, vortex shedding from the cylinder surface will be an issue that has to be considered. Vortex shedding will actuate sidewise motion of the model setup, which will influence the measurements. The vortex shedding frequency is dependent on the incoming flow velocity and the cylinder diameter. The Strouhal number describes the relation between theses parameters and shedding frequency, and is defined by $St = f_v d / U$, where f_v is the vortex shedding frequency

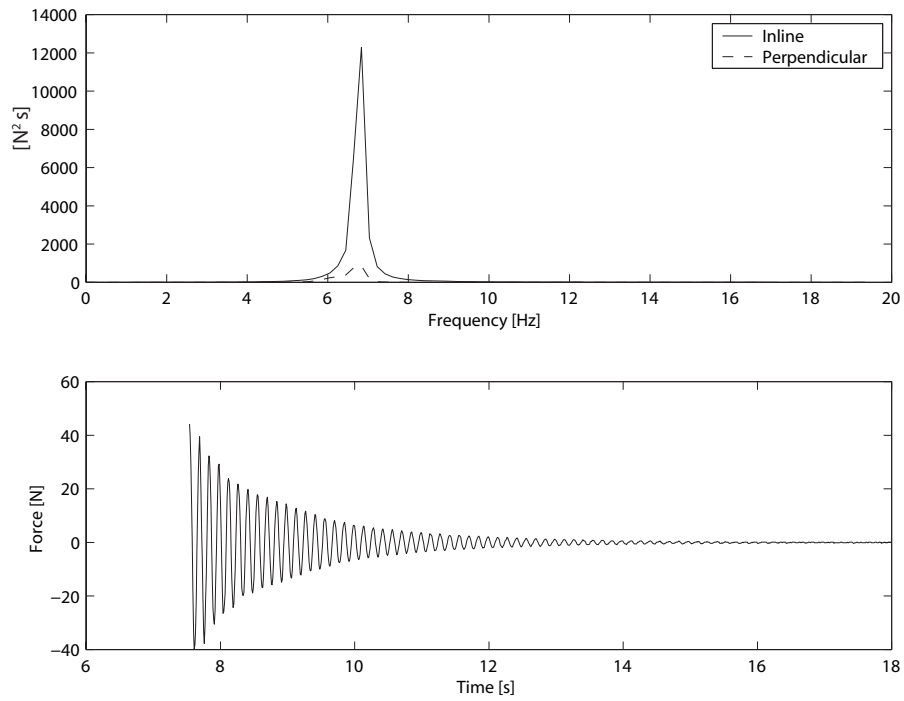


Figure 3.10: Results for the decay test in the in-line direction.

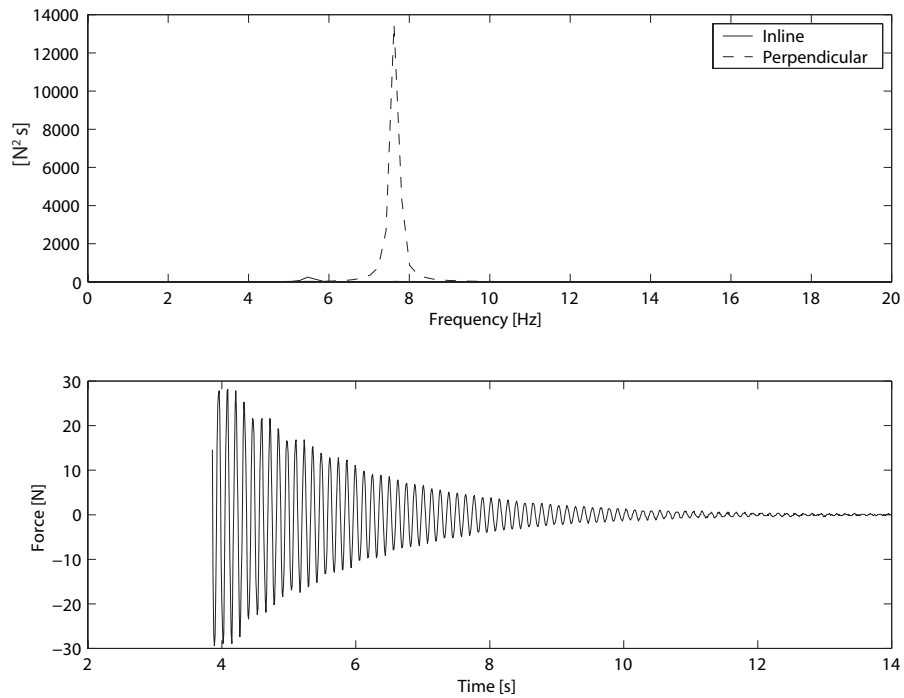


Figure 3.11: Results for the decay test in the perpendicular direction.

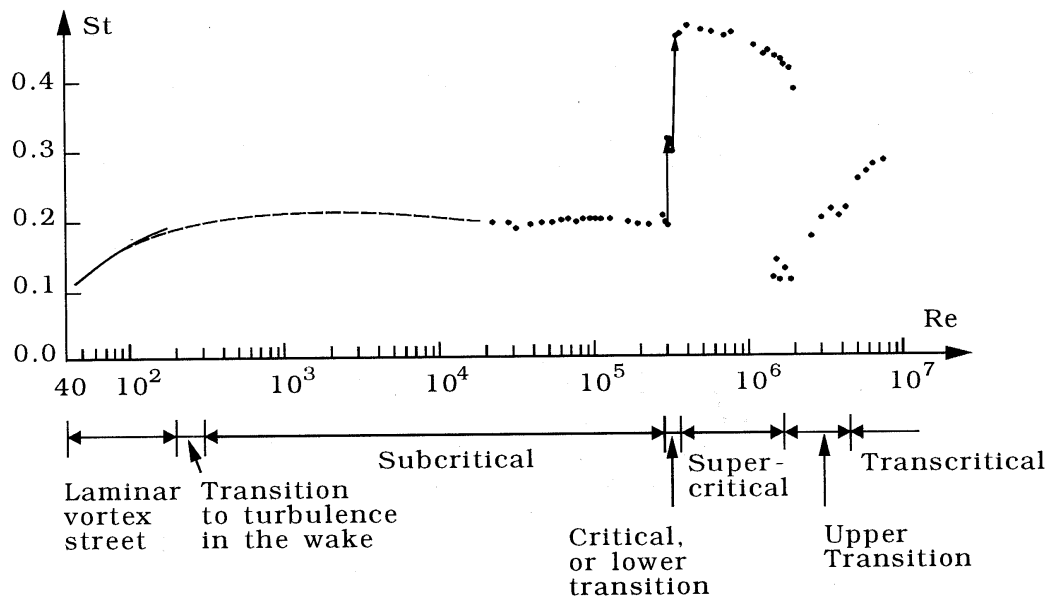


Figure 3.12: The Strouhal number for a smooth circular cylinder as a function of the Reynolds number. Experimental data: Solid curve: Williamson (1989). Dashed curve: Roshko (1961). Dots: Schewe (1983).

Table 3.4: The vortex shedding frequency f_v for some velocities.

Velocity [m/s]	0.25	0.375	0.5	0.75	1.0
f_v	1.25	1.88	2.50	3.75	5.0

and U is the fluid velocity. The Strouhal number is flow dependent. Figure 3.12 show the relation between the Strouhal number and the Reynolds number Re . For subcritical flow, which is the range of interest, the Strouhal number is approximately 0.2.

In table 3.4 are listed the calculated vortex shedding frequency for the velocities relevant to the experiments.

In Figure 3.13 an example of results from a Fourier analysis of a measurements series with $s = 5d$ and two different velocities, $U_\infty = 0.375$ [m/s] and $U_\infty = 0.5$ [m/s], is presented. In the perpendicular direction the eigenfrequency of the model setup can be recognized. A peak in the frequency power specter at approximately twice the vortex shedding frequency is also recognized. The values are 3.76 and 5.0 for $U_\infty = 0.375$ [m/s] and $U_\infty = 0.5$ [m/s] respectively.

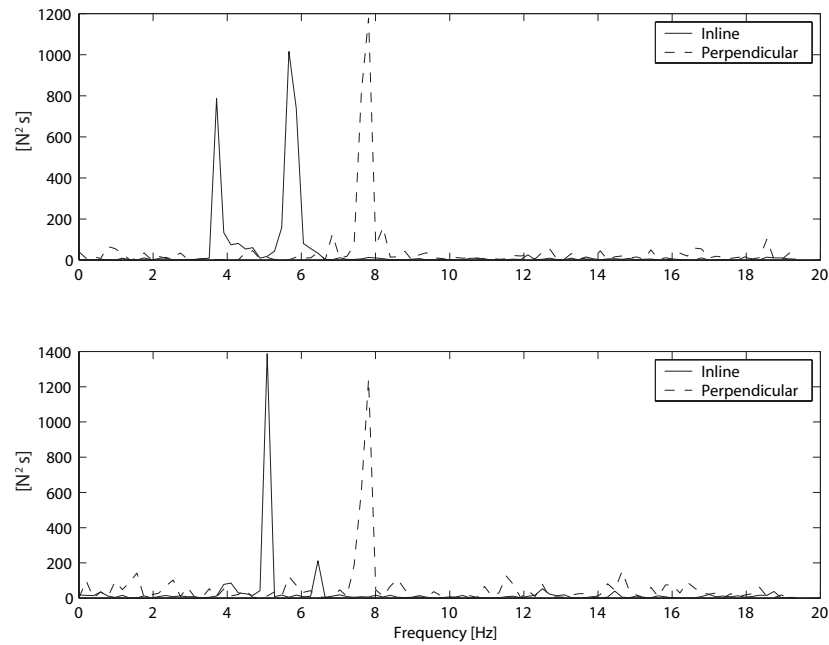


Figure 3.13: Example of a FFT analysis of measurement series. $s = 5d$ for $U_\infty = 0.375$ [m/s] (upper) and $U_\infty = 0.5$ [m/s] (lower).

Cylinder drag coefficients As a part of verifying the setup a single cylinder were tested at different towing speeds. The results are presented in Table 3.5. Further is the results for the drag coefficient presented in Figure 3.14 together with results for the drag coefficient of a circular cylinder taken from Schlichting (1968). As seen from the figure, the drag coefficient from the experiments is lower than the experimental results presented by Schlichting, especially for the two highest velocities, $U_\infty = 0.5$ [m/s] and $U_\infty = 1.0$ [m/s]. The reason for a smaller drag coefficient is likely to be due to the three-dimensional effects that will be present in the experiment. It is likely that there will be three-dimensional effects due to the cylinder penetrating the free surface, the cylinder not being attached at the submerged end and the opening at the submerged end. For $U_\infty = 0.5$ [m/s] and $U_\infty = 1.0$ [m/s] the drag coefficient is approximately equal to 1.1. This drag coefficient is chosen to be used in the evaluation of the experiments. As a comparison, in the last column of the table the calculated drag force on the cylinder using $F_d = 1/2\rho dhU^2$ is given. The drag force is calculated using the measured velocity and with a drag coefficient of 1.1.

3.3.3 Discussion of the experimental results

In this section figures with results for drag and lift will be presented. Figures of the in-line and perpendicular results as well as tables with detail results are presented in Appendix A.

Table 3.5: Results from test with single cylinder.

Velocity U_∞ [m/s]	Measured velocity [m/s]	Rn [-]	Measured drag force [N]	Drag coefficient C_d [-]	Calculated drag force F_d [N]
0.25	0.251	8807	1.046	1.038	1.109
0.375	0.378	13263	2.656	1.162	2.515
0.50	0.506	17754	4.552	1.111	4.506
1.0	0.982	34456	17.150	1.112	16.972

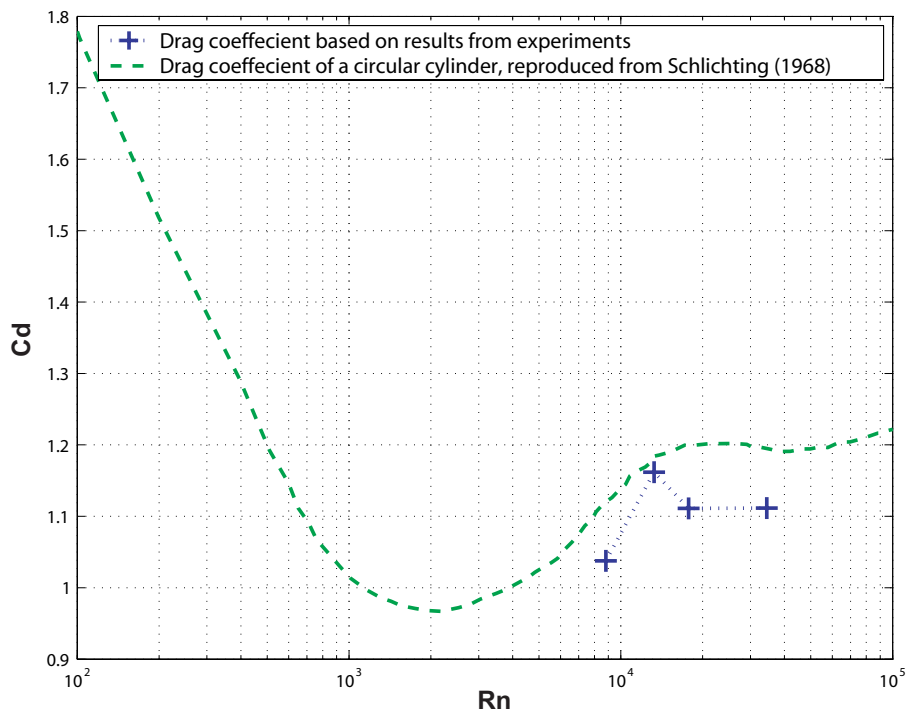


Figure 3.14: Comparison between the drag coefficient of a circular cylinder calculated from the experiments and the drag coefficient presented in Schlichting (1968), as a function of Reynolds number with respect to the cylinder diameter. Logarithmic x-axis.

All the results are presented as non-dimensionalized force coefficients, denoted grid force coefficients, by dividing the forces by $1/2\rho dhU^2 N$, where N is number of cylinders and U is the measured velocity. The drag force is defined as the force in the towing direction and the lift force is perpendicular to it. The drag and lift grid force coefficients are calculated values, based on transformation of the in-line and perpendicular forces, while the in-line and perpendicular coefficients are normalized directly from the measured values. The drag grid force coefficient is denoted, C_d , and the lift grid force coefficient, C_l . All presented results are averaged values from several runs.

The wake angle is defined to be the angle of attack for the model to the flow direction, where the wake of one cylinder no longer are influencing the incoming flow of the cylinder behind it, i.e. the angle when the force on the system of cylinders is equal to the sum of the forces of the five individual cylinders in uniform flow.

In Figure 3.15, 3.16 and 3.17 the different results are grouped together with respect to spacing, s , between the vertical cylinders, and results for different towing speeds are presented in the same figure. In Figure 3.18, 3.19 and 3.20 the different results are grouped together with respect to the towing speed, U_∞ , and results for different spacings are presented in the same figure.

The forces on the cylinders at the lowest towing speed $U_\infty = 0.25$ [m/s] were so small (approximately $2.5[N]$) that it was difficult to measure them, especially for the smallest angles, where the forces will be at the lowest. This is the reason why the in-line force is not zero at zero degree angle. This lead to results that vary a lot and are not conclusive. The results are nevertheless presented here since qualitatively they fit with the results from the other towing speeds.

Two main basic observations:

- From the first three figures it is seen that there is very little difference in the measured grid force coefficients as a function of U_∞ . The small variation seen is likely to be due to measurements inaccuracies. Based on these results, it can be concluded that the grid force coefficients is independent of the towing speed, both in magnitude and with respect to the shape of the grid drag force “coefficient curve”, which are related to the wake angle behind a cylinder.
- On the contrary, the presented grid force coefficients in the last three figures differ a lot, both in magnitude and shape of the grid drag force “coefficient curve”. These results indicate a strong dependency of the spacing s between the cylinders.

These observations are as expected and are qualitatively in agreement with the theory of Schlichting (1968) and the results obtain by using Equation (3.10), where the wake

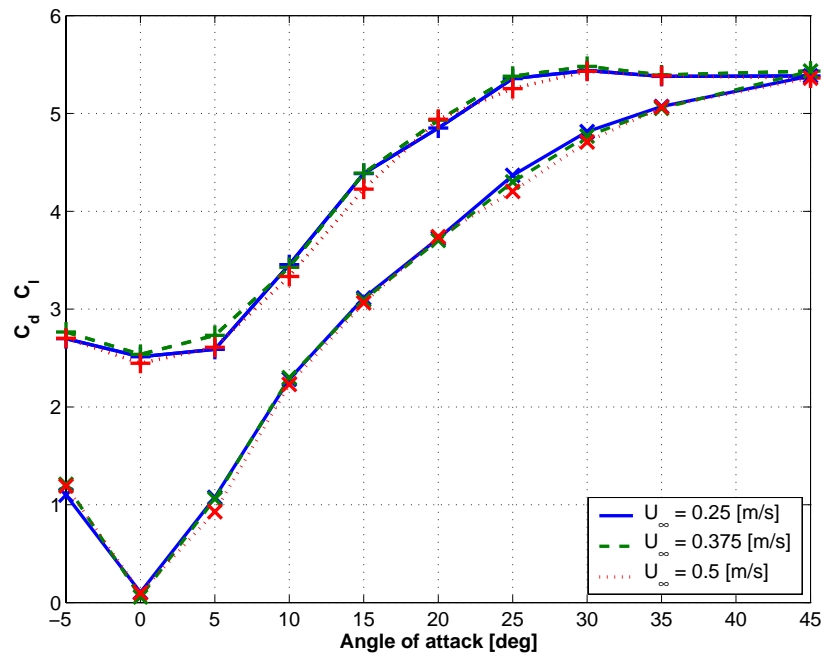


Figure 3.15: Drag, (+) and lift (\times) grid coefficient from the experiments as a function of angle of attack, α at different velocities. Five cylinders in a row with spacing $s = 5d$.

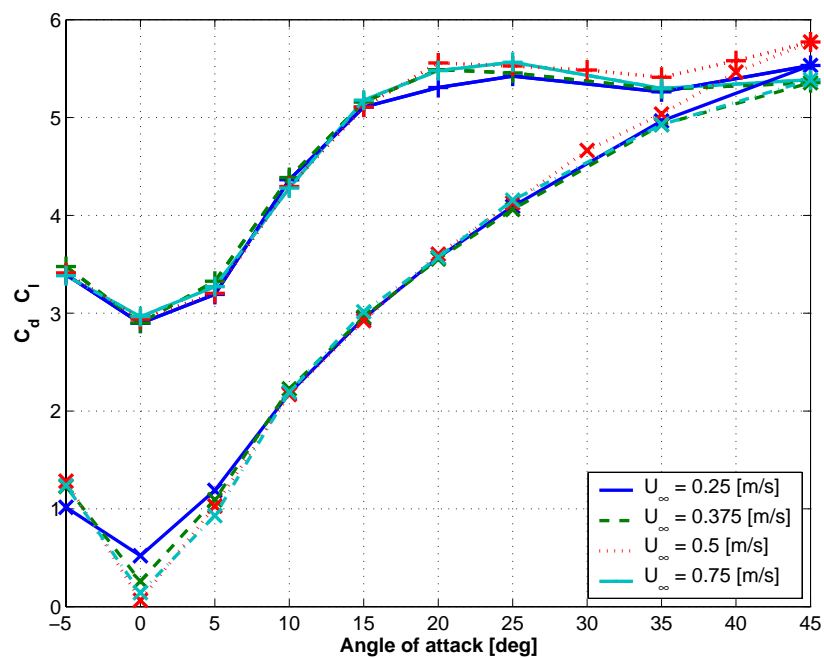


Figure 3.16: Drag (+) and lift (\times) coefficient from the experiments as a function of angle of attack, α at different velocities. Five cylinders in a row with spacing $s = 7.5d$.

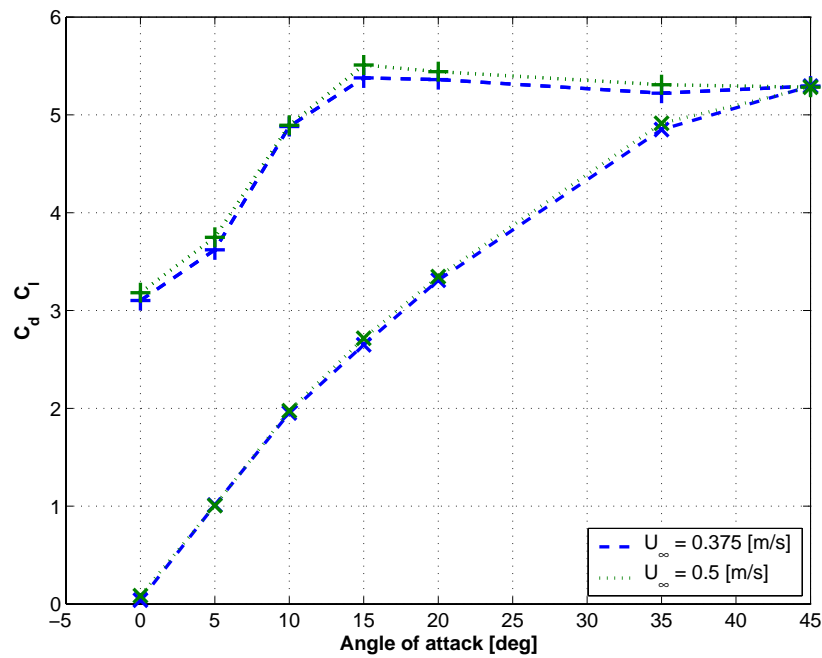


Figure 3.17: Drag (+) and lift (x) coefficient from the experiments as a function of angle of attack, α at different velocities. Five cylinders in a row with spacing $s = 10d$.

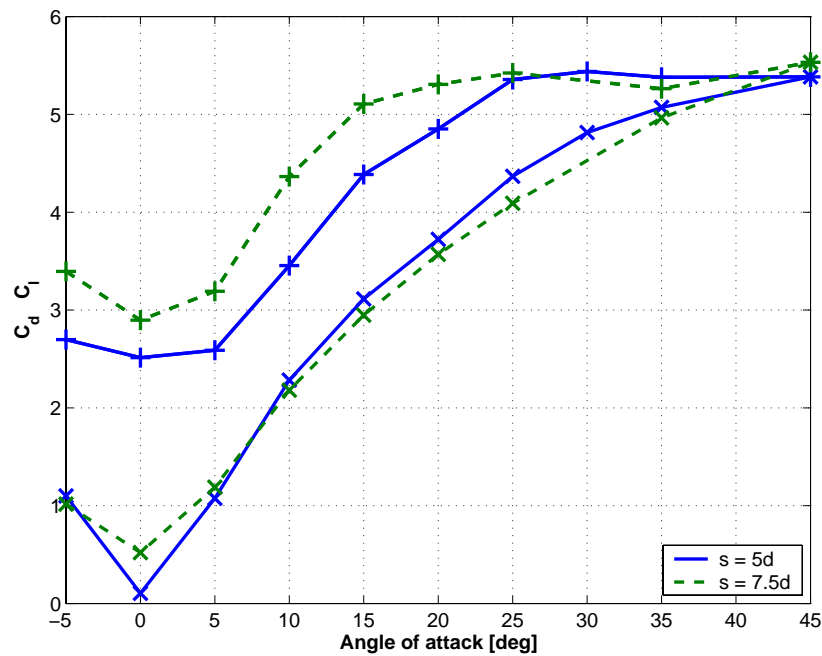


Figure 3.18: Drag (+) and lift (x) coefficient from the experiments as a function of angle of attack, α at different spacings, s . Five cylinders in a row with with $U_\infty = 0.25$ [m/s].

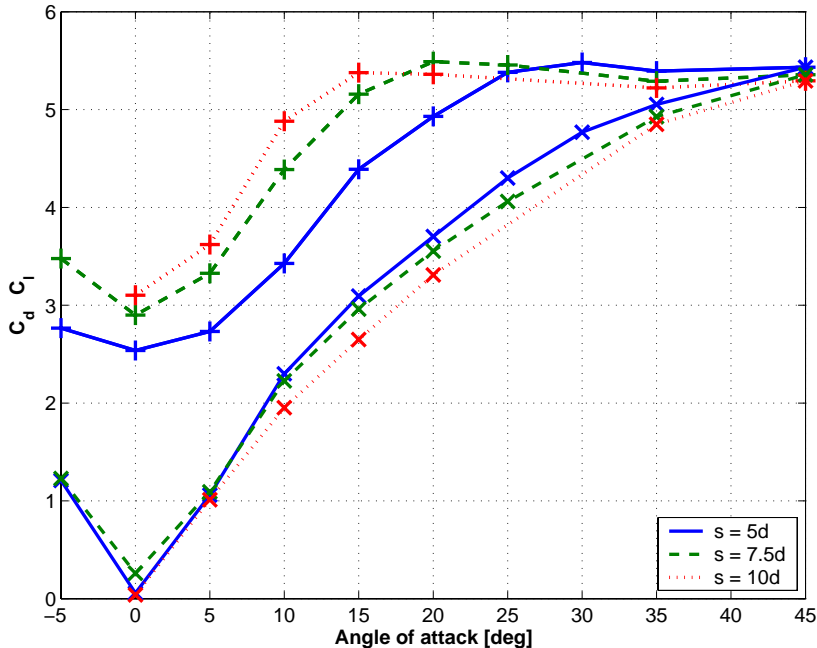


Figure 3.19: Drag (+) and lift (x) coefficient from the experiments as a function of angle of attack, α at different spacings, s . Five cylinders in a row with with $U_\infty = 0.375$ [m/s].

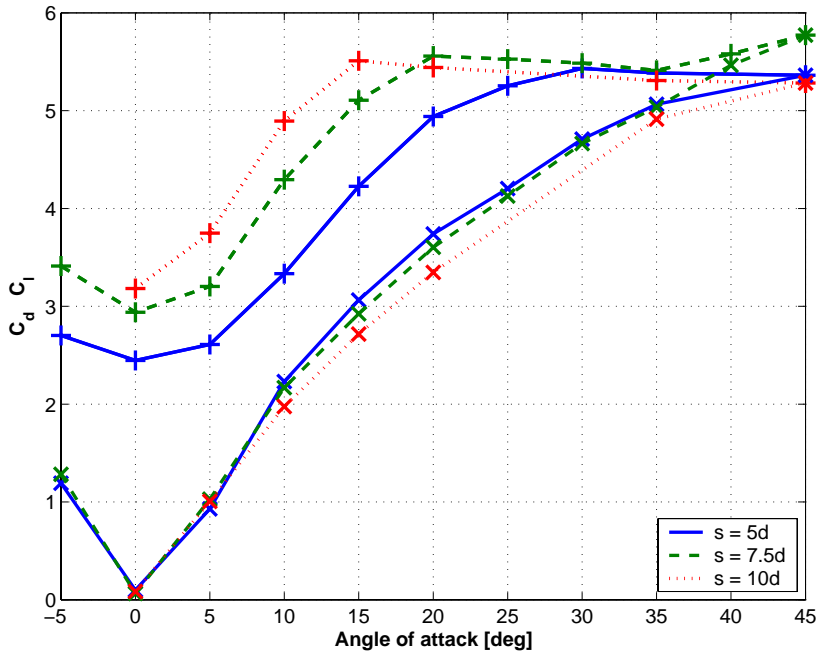


Figure 3.20: Drag (+) and lift (x) coefficient from the experiments as a function of angle of attack, α at different spacings, s . Five cylinders in a row with with $U_\infty = 0.5$ [m/s].

reduction factor and spreading of the wake are independent of the incoming flow velocity, but vary as a function of the space coordinates x and y .

From all the figures it is evident that the results for the drag force coefficient approach an asymptotic value, which is approximately equal to a 5.5. This corresponds to a single cylinder drag coefficient of 1.1, which is equal to the measured value for a single cylinder as described in Subsection 3.3.2. The grid lift force coefficient approaches the same value at an angle of attack of 45 [deg], but will decrease to zero at an angle of attack of 90 [deg]. Thus a grid drag coefficient of approximately 5.5 (see Table 3.3.2) indicate that there is no flow interaction between the different individual cylinders in the setup affecting the total drag and lift force on the grid. Using this as an indicator, it is seen from the figures that for a spacing of $s = 10d$, the wake angle is approximately 15 [deg], for a spacing of $s = 7.5d$, the wake angle is approximately 20 [deg] and finally for a a spacing of $s = 5d$, the wake angle is approximately 25 [deg]. In other words, the wake angle decreases for increasing spacing s , along with a left shift in the grid drag force “coefficient curve”. Further, for a given angle of attack the grid drag force coefficient is increasing with increasing spacing, while the grid lift coefficient is decreasing with increasing spacing.

3.3.4 Potential inaccuracies and errors in the experiment

Surface roughness The drag coefficient of a cylinder in free flow can be affected by the surface roughness of the object exposed to the flow. This effect is illustrated in Figure 3.21. As seen from the figure, the effect on the drag coefficient due to the surface roughness is seen as a left shift of the transition from subcritical to supercritical flow, and an increase in the drag coefficient in the supercritical flow regime. The presented results for grid force coefficients are with a maximum towing speed of $U_\infty = 0.5[m/s]$, corresponding to a maximum Reynolds number of 1.8×10^4 . Thus it is expected that any surface roughness of the cylinders used in the experiments will not affect the measured forces.

Effect due to cylinder close to wall Due to the limited space in a towing tank, it is possible to experience effects on the results related to the bottom and side walls in the towing tank. At an angle of attack of 90 [deg] and the largest spacing the outermost cylinder will be a distance of 60[cm] or $15d$ from the side walls of the towing tank. As seen from Table 3.3.2, in the experiments there is a range in Reynolds number from approximately 0.8×10^4 to 3.5×10^4 . In Figure 3.22 are presented different experimental results for drag coefficient for a cylinder near a plane wall, at relevant Reynolds numbers. As seen from the figure, to experience any near wall effects in this Reynolds number range, the cylinder has to be closer than one diameter from the wall. Thus no effects due to the cylinders being close to the wall is expected this in the results.

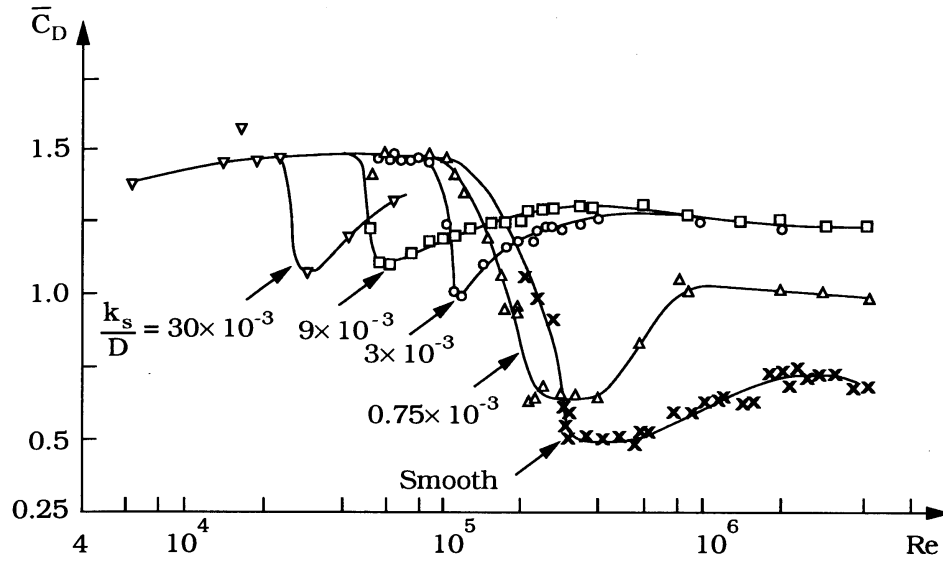


Figure 3.21: Experimental results for the drag coefficient of a cylinder in free flow with different surface roughness as a function of Reynolds number. (Sumer & Fredsøe 1997).

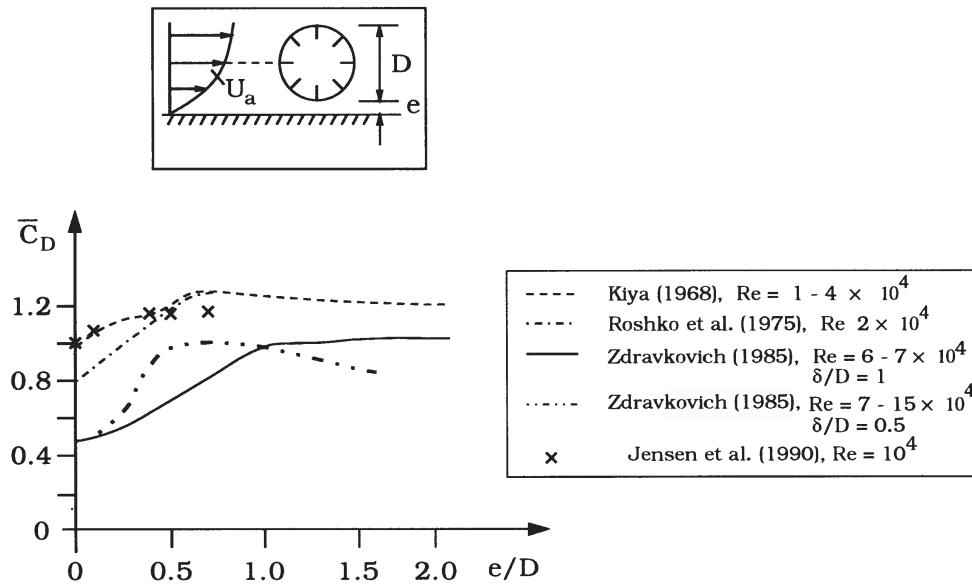


Figure 3.22: Drag coefficient for a cylinder near a plane wall. In the figure δ is the boundary layer thickness of the approaching flow. (Sumer & Fredsøe 1997).

The cylinders are towed vertical and the distance from the edge of the cylinder to the bottom of the towing tank is $5d$. Thus since the distance is larger than one diameter, no effects due to the bottom are either expected.

Effects due to generation of waves When towing the cylinder there will be generated waves due to the free surface. The width of the cylinder compared to draft is very small. Thus it is expected that the added resistance due to generation of waves will be negligible compared to the drag force on the cylinder. This is also seen from the experimental results as the grid drag coefficient is nearly independent of the towing speed, while added resistance due to generation of waves will be speed dependent.

3.3.5 Visualization

Some simple means of illustrating any three-dimensional effect were tried out. Syrup mixed with a color substance was smeared on the upstream part of a single cylinder. While towing the cylinder at constant speed the syrup let out a stream of color, which could be filmed using strong light and underwater camera. Figure 3.23 show an example of the visualization. Using this simple technique some qualitative description of the three-dimensional flow and effects influencing the results, could be obtained.

From the figure a cross flow around the cylinder bottom can be noted. Thus a flow velocity which is respectively downwards and upwards at the upstream and downstream side of the cylinder is created. This will lead to narrowing of the vertical height of the wake. Further there is a contraction of the vertical extension of the wake of the wake with increasing distance downstream. The consequence for a downstream cylinder will be that the lower part of the cylinder sees an undisturbed incident flow. The influence of this effect on the results are discussed further in Subsection 3.4.4.

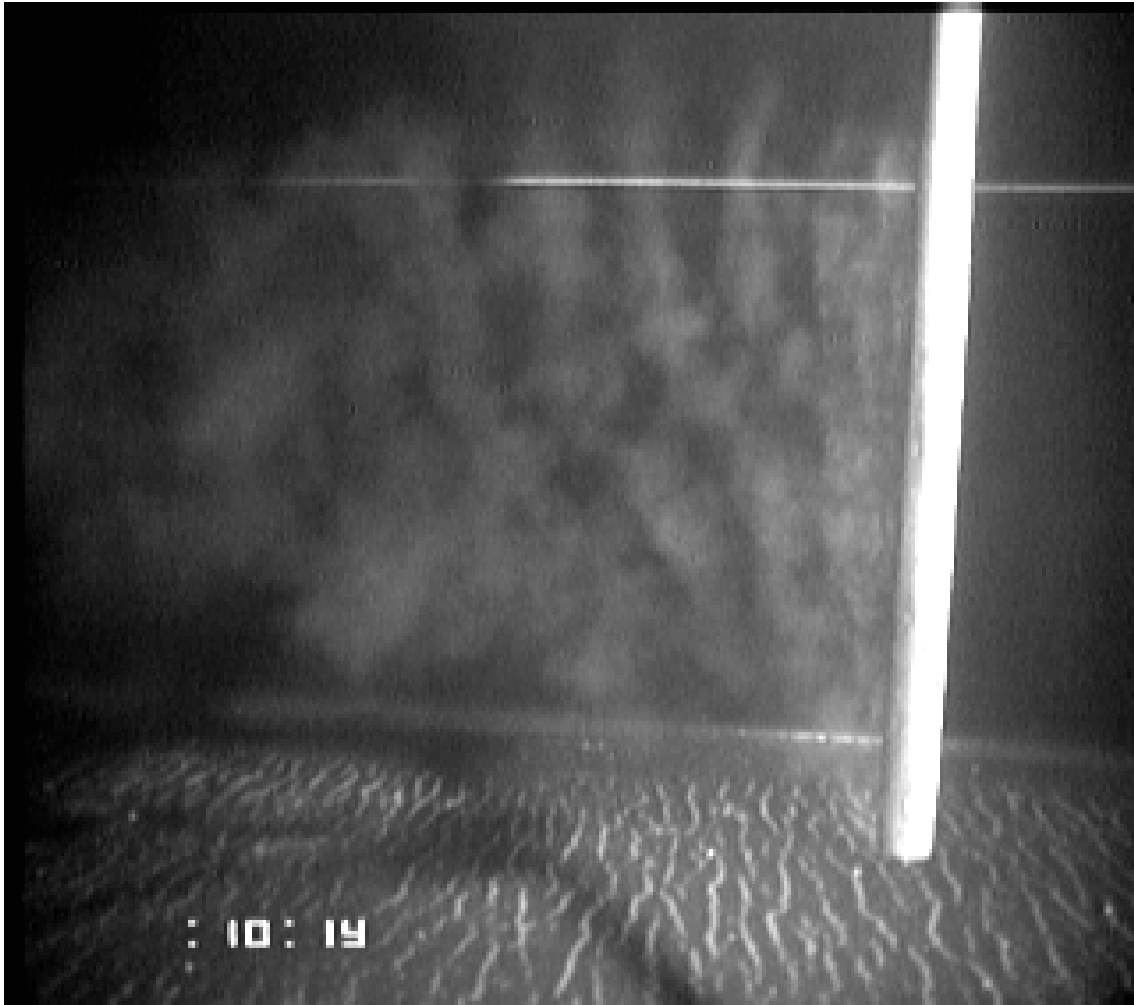


Figure 3.23: Visualization of three dimensional flow behind a single cylinder, towed at constant speed.

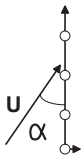
3.4 Drag on multiple cylinders

3.4.1 Added effect of several cylinders

As previously mentioned there is no established theory or method on how to sum the contribution and influence from several cylinders in-line in a undisturbed flow, to make up a proper model for the velocity in the wake behind such a system of cylinders. According to Zdravkovich (1985) there are uncertainties related to how several cylinders interact and generate a total wake field. Zdravkovich presents in his paper results regarding the wake region behind clusters of cylinders in different arrangements and also results for the flow behind two and three cylinders in a in-line arrangement. Zdravkovich concludes that introducing a third cylinder actually produces a new kind of flow, not equal either to the flow behind one, two or three cylinders. Based on this Zdravkovich further states that it is not possible to generalize results for one or two cylinder into N number of cylinders.

Zdravkovich defines two basic kinds of flow interference regimes between two parallel cylinders, “Proximity interference” and “Wake interference”, where the first type is related to cylinders in side by side arrangements and the second type is related to the downstream cylinder in a tandem or staggered arrangement. In the paper Zdravkovich presents a figure (Figure 3.24) defining the different regions of flow interference as a function of y/d and x/d ratios. As previously, the axes are defined with origin in the center of the cylinder, the x-axis is pointing in the flow direction (longitudinal direction) and the y-axis is perpendicular to the cylinder axis (transversal direction). Two observations from this figure: For a side by side arrangement, the two cylinders has to be closer than 4 diameters apart to have a interference and that a x/d ratio of 5 corresponds to wake interference region with a “width” of approximately $y/d = 1.5$. This last observation is in accordance with the results obtained using the mean velocity deficit models presented in Section 3.2 and in Figure 3.6. Based on this results it is likely that a net structure will experience wake interference at some angle of attack, but interference between parallel twines at a angle of attack, α , of 90 [deg] is not likely.

A cylinder downstream will experience a wake field which is a result of the generated wake of all the preceding cylinders. The effect of all the preceding cylinders is added linearly. Then the mean velocity experienced by cylinder N , adding the velocity deficit due to all



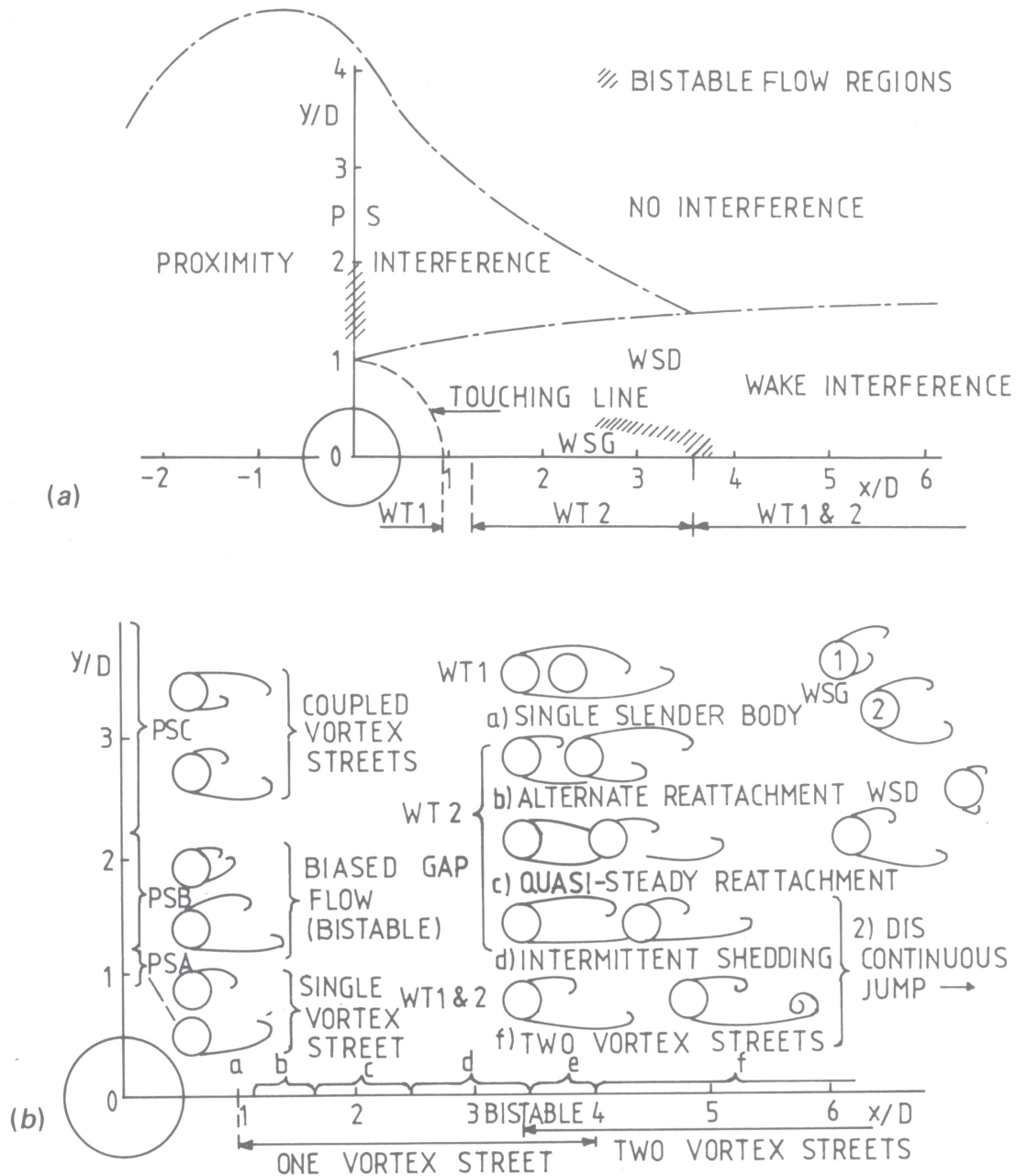


Figure 3.24: (a). Regions of flow interference categories and (b) interference flow regimes (schematic). PSA, PSB and PSC are different parts of the area described as PS in (a). WT1, WT2, WSD and WSG are explained in (a). (Zdravkovich 1985)

the proceeding N cylinders (including cylinder 0), can be expressed as:

$$\begin{aligned}
U_1 &= U_\infty - U_\infty 0.95 \sqrt{\frac{C_d}{\left(\frac{x_1-x_0}{d}\right)}} \exp\left(\frac{-\left(\frac{y_1-y_0}{d}\right)^2}{0.0888 C_d \left(\frac{x_1-x_0}{d}\right)}\right) \\
U_2 &= U_\infty - U_\infty 0.95 \sqrt{\frac{C_d}{\left(\frac{x_2-x_0}{d}\right)}} \exp\left(\frac{-\left(\frac{y_2-y_0}{d}\right)^2}{0.0888 C_d \left(\frac{x_2-x_0}{d}\right)}\right) - \\
&\quad U_1 0.95 \sqrt{\frac{C_d}{\left(\frac{x_2-x_1}{d}\right)}} \exp\left(\frac{-\left(\frac{y_2-y_1}{d}\right)^2}{0.0888 C_d \left(\frac{x_2-x_1}{d}\right)}\right) \\
U_3 &= U_\infty - U_\infty 0.95 \sqrt{\frac{C_d}{\left(\frac{x_3-x_0}{d}\right)}} \exp\left(\frac{-\left(\frac{y_3-y_0}{d}\right)^2}{0.0888 C_d \left(\frac{x_3-x_0}{d}\right)}\right) - \\
&\quad U_1 0.95 \sqrt{\frac{C_d}{\left(\frac{x_3-x_1}{d}\right)}} \exp\left(\frac{-\left(\frac{y_3-y_1}{d}\right)^2}{0.0888 C_d \left(\frac{x_3-x_1}{d}\right)}\right) - \\
&\quad U_2 0.95 \sqrt{\frac{C_d}{\left(\frac{x_3-x_2}{d}\right)}} \exp\left(\frac{-\left(\frac{y_3-y_2}{d}\right)^2}{0.0888 C_d \left(\frac{x_3-x_2}{d}\right)}\right) \\
U_N &= U_\infty - \sum_{i=0}^N \left\{ U_i 0.95 \sqrt{\frac{C_d}{\left(\frac{x_N-x_i}{d}\right)}} \exp\left(\frac{-\left(\frac{y_N-y_i}{d}\right)^2}{0.0888 C_d \left(\frac{x_N-x_i}{d}\right)}\right) \right\} \quad (3.20)
\end{aligned}$$

The original far wake mean deficit model by Schlichting is used in the equation. Notations refer to Figure 3.3. In this expression, for a given cylinder N , the velocity deficit from each of the preceding cylinder is added as they were independent. The mean inflow velocity on each of the cylinders is a function of the proceeding cylinders and relates to the undisturbed flow U_∞ independently of the number of cylinder or arrangement of the cylinders.

An optional simple model for calculating the effect of several cylinders in-line, could be to assume a new flow region for every cylinder. Then the “undisturbed” inflow velocity to every region is equal to the inflow velocity experienced by the cylinder N . Thus assuming that for every region Equation (3.10) can be used by only changing the velocity U_0 to U_{N-1} . Then the mean velocity experienced by cylinder N , can be expressed as:

$$U_N = U_\infty \prod_{i=1}^N \left\{ 1 - 0.95 \sqrt{\frac{C_d}{\left(\frac{x_i-x_{i-1}}{d}\right)}} \exp\left(\frac{-\left(\frac{y_i-y_{i-1}}{d}\right)^2}{0.0888 C_d \left(\frac{x_i-x_{i-1}}{d}\right)}\right) \right\} \quad (3.21)$$

If the distance between the cylinders are constant in x- and y-direction, Δx and Δy say, the relative width and magnitude of the different wake zones are in this scheme identical. The problem can then be expressed with this simple equation:

$$U_N = U_\infty \left\{ 1 - 0.95 \sqrt{\frac{C_d}{\left(\frac{\Delta x}{d}\right)}} \exp\left(\frac{-\left(\frac{\Delta y}{d}\right)^2}{0.0888 C_d \left(\frac{\Delta x}{d}\right)}\right) \right\}^N \quad (3.22)$$

The results using these two different methods are quite close. However, Equation (3.21) implies an assumption of a new flow situation starting from the center of every cylinder, which clearly will not be physically correct. Due to this it is believed that using Equation (3.20) is more physically correct, and this equation will be used in the further discussion.

Replacing the model by Schlichting in Equation (3.20) with the model by Blevins (1990), the mean inflow velocity of cylinder N becomes:

$$U_N = U_\infty - \sum_{i=0}^{N-1} \left\{ U_i 1.02 \sqrt{\frac{C_d}{6 + \left(\frac{x_N - x_i}{d}\right)}} \exp\left(\frac{-(y_N - y_i)^2}{0.0767 C_d \left(6 + \left(\frac{x_N - x_i}{d}\right)\right)}\right) \right\} \quad (3.23)$$

Figure 3.25 show calculated inflow velocity on individual cylinders in a straight row of 100 cylinders, at four different angles of attack, using Equation (3.23). It is evident that the model has a strong dependency on angle of attack. For a angle of attack of 15 [deg], the calculated mean inflow velocity for the downstream cylinders are nearly undisturbed after only 10 cylinders. With a spacing between the cylinders of 5 times the diameter ($x/d = 5$) of the cylinder, an angle of attack of 15 [deg] actually corresponds to a transversal distance of only 1.3 diameters ($y/d = 1.3$). Thus there is a transversal open space between the two cylinders of only 0.3 diameters. Further the inflow velocity seems to reach an asymptotic value, even when the row of cylinders are situated at an angle of attack to the flow of 0 [deg].

3.4.2 Two cylinders

In Figure 3.26 the calculated drag coefficient on the downstream cylinder in a staggered arrangement at $x/d = 5$ is presented, with the Reynolds number $Rn = 1.75 \times 10^4$. In the same figure, measurements by Price & Paidoussis (1984) at Reynolds number $Rn = 5.3 \times 10^4$ and by Herfjord, Holmås, Leira, Bryndum & Hanson (2002) at $Rn = 2.0 - 6.0 \times 10^4$, are presented. d has been used as a characteristic length in Rn . The calculated results are not sensitive to Reynolds number.

A relatively large variation in the measured C_d -values in a rather limited Reynolds number range where the flow on the upstream cylinder is in the subcritical flow regime with laminar boundary layer, is noted. This variation could be due to the turbulence in the incoming flow on the downstream cylinder, generated by the upstream cylinder. This affects the boundary layer flow and the separation points of the downstream cylinder and then reduces the drag coefficient. Figure 14.18 in Zdravkovich (1997) shows that the turbulence intensity of the incident flow can decrease C_d as much as 50% for a Reynolds number as low as 2.0×10^4 . Clearly, it is not possible to show this dependency with a time averaged velocity deficit model. However, as seen from the figure, the presented results using either the “Virtual

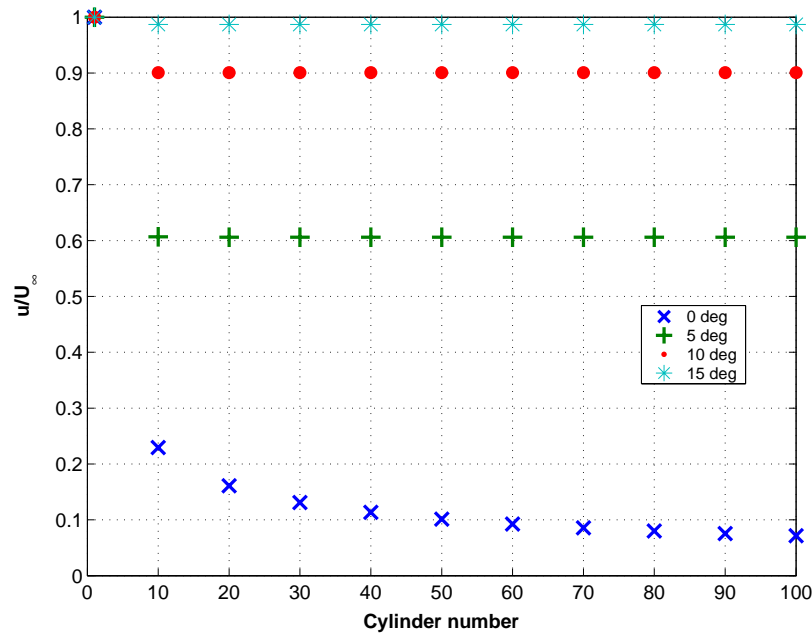


Figure 3.25: Inflow velocity on individual cylinders, with 100 cylinders in a row, at different angles of attack. The results are obtained using the “Virtual origin” model (Blevins 1990). Properties: $d = 4.0$ [cm], $U_\infty = 0.5$ [m/s] and distance between cylinders five times the diameter.

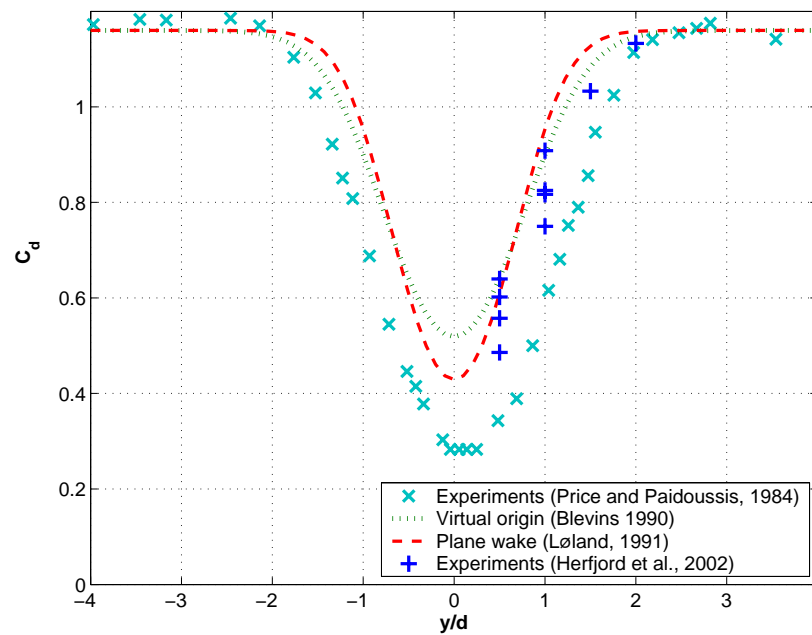


Figure 3.26: Drag coefficient for a single cylinder in the wake of another cylinder as a function of transversal distance y/d , at a distance $x/d = 5$. $Rn = 2 - 6 \times 10^4$ with respect to one cylinder diameter.

origin” or “Plane wake” models, are otherwise quite consistent with the experiments by Herfjord et al. (2002).

Figure 3.27 shows comparisons between results obtained using the present method with the “Virtual origin” model, and measurements by Herfjord et al. (2002) for $y/d = 0.5$ and 1 as a function of x/d . The “Virtual origin” model gives reasonable predictions for x/d as low as 4.0 for $y/d = 0.5$ and even lower for $y/d = 1.0$. The results for $y/d = 0.5$ are consistent with tandem cylinders, where abrupt changes in C_d occur at $x/d = 3.8$ (Okajima 1979). Herfjord et al. (2002) also presented numerical CFD results for $y/d = 0.5$ and $y/d = 1.0$ based on solving 2D unsteady laminar Navier-Stokes equation with FEM at $Re = 200$. Even though Herfjord et al. (2002) assume laminar flow and the present method use a turbulent wake model, their results agree well with our results.

For low y/d ratios the velocity deficit model do not predict the low drag force on the second cylinder as seen from the experiments. Two or more cylinders in a staggered arrangement give a very complicated flow pattern. Previous results (e.g. Zdravkovich 1985) show a large dependency for the measured properties of the second cylinder on the placement in the wake (both in the longitudinal and transversal direction) and Reynolds number. In some instance it is possible to get negative drag on the second cylinder.

3.4.3 Five cylinders

Figure 3.28 presents numerical and experimental results for the drag coefficient of five cylinders in a row, when the distance s between the axis of two cylinders near by each other is $5d$. The experimental results are from the experiments presented in Section 3.3. The numerical results are based on the model by Schlichting (1968), and the modified models “Virtual origin” (Blevins 1990) and “Plane wake” (Løland 1991). Figure 3.28 shows good agreement in general, but the numerical results by the mean velocity deficit models are too “steep” compared to the experiments. At an angle of attack of 0 [deg] the calculated drag forces are slightly too low. The results obtained using the “Virtual origin” have the best agreement. Further with increasing angle of attack until approximately 30 [deg], the calculated values are too high, again with the model by Blevins giving the best agreement. Both the models “Plane wake” and “Virtual origin” agree slightly better with the experiments than the original model by Schlichting.

It is apparent that the models overestimate the velocity reduction for angle of attack close to zero and thus calculates too low drag forces at small angle of attack. At the same time the width of the wake is calculated to be too narrow, giving rise to the too high drag forces as a function of angle of attack. The influence of turbulence intensity in the incident flow on the downstream cylinders is believed unimportant in this case.

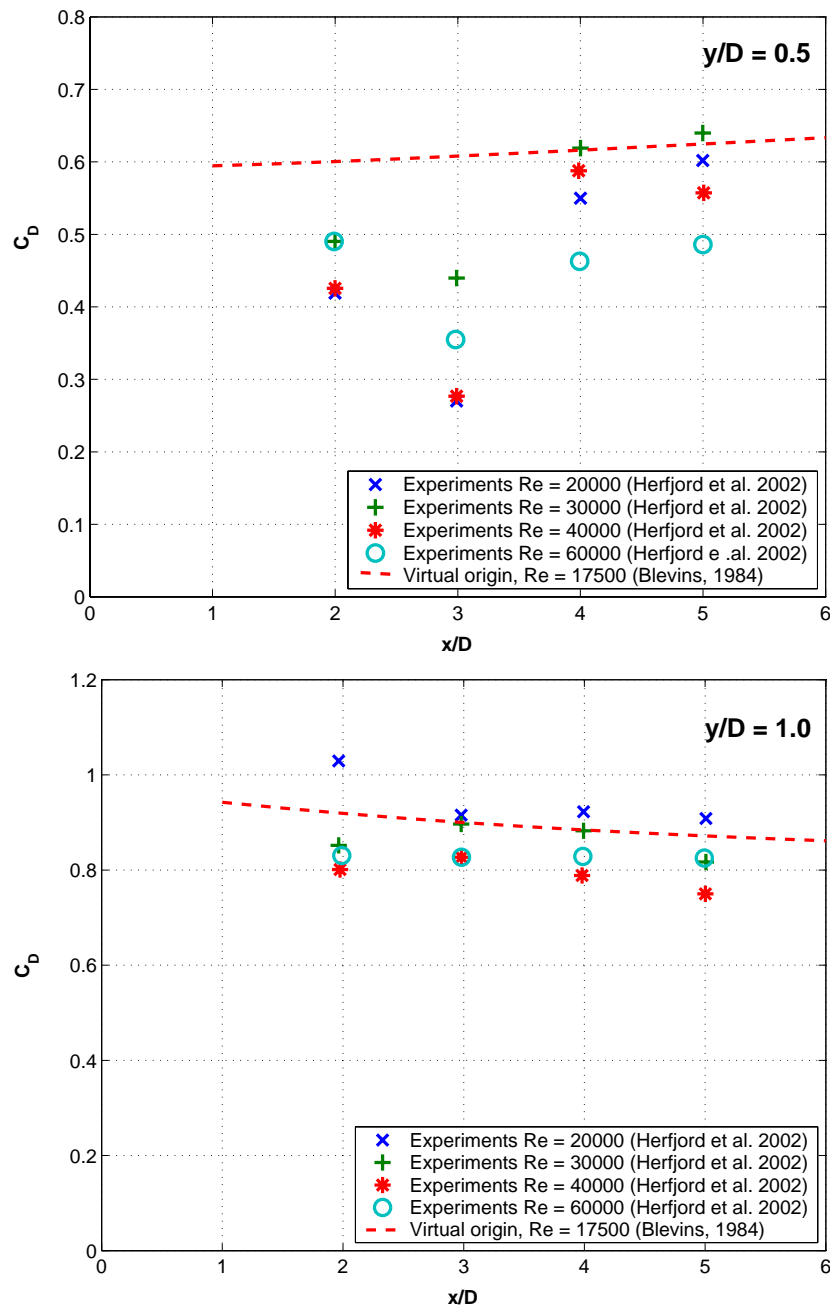


Figure 3.27: Drag coefficient for a single cylinder in the wake of another cylinder as a function of x/d at two different transversal distances y/d . Reynolds number, Re , with respect to one cylinder diameter.

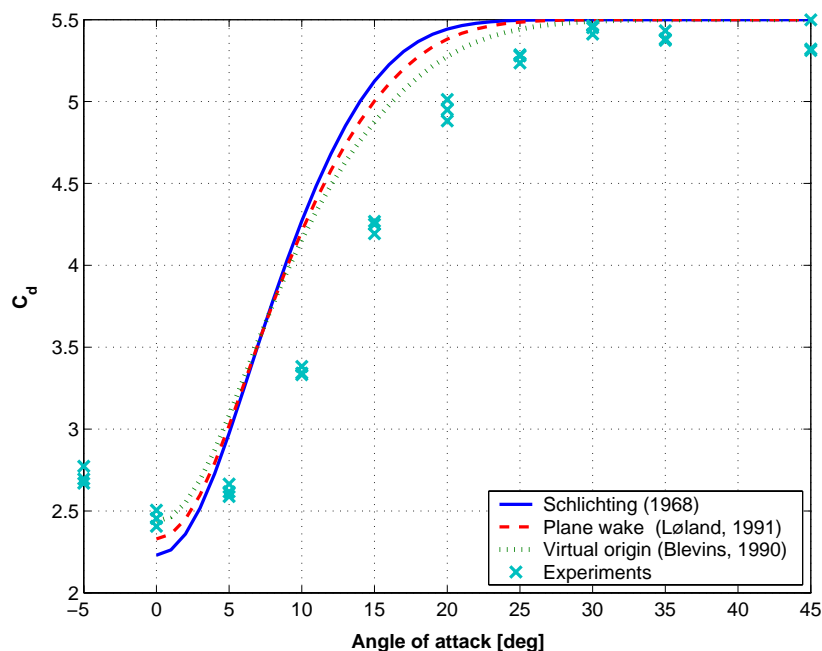


Figure 3.28: Drag coefficient for five cylinders in a row as a function of angle of attack α . $s = 5d$ and the uniform velocity is 0.5 [m/s].

3.4.4 Possible effects influencing the results

Three dimensional effect in experiments

In Figure 3.29 the wake behind a cylinder towed at constant speed is shown as described in Section 3.3. As seen from the figure, there is a cross flow around the cylinder bottom. This cross flow introduces a velocity field which is downwards and upwards at the upstream and downstream side of the cylinder, respectively. The effect of this cross flow on the measurements is not entirely understood. But it is likely that shedding of vortices are influenced and thus that the vertical height of the effective wake region behind the cylinders becomes smaller. It can also from the picture seem like there is a further contraction of the vertical extension of the wake with increasing distance downstream.

The consequence for a downstream cylinder is that the lower part of the cylinder sees an undisturbed incident flow. The result is that the drag force on a downstream cylinder will be higher compared to an idealistic 2D situation and thus compared to our numerical model assuming a velocity deficit over the whole height of the downstream cylinder. This may influence the calculated results in Figure 3.28 by a order of 10% and could explain some of the discrepancies at low angles of attack. But since this effect is actually increasing the drag force in the experiments, it will not explain all of the discrepancy. Results were

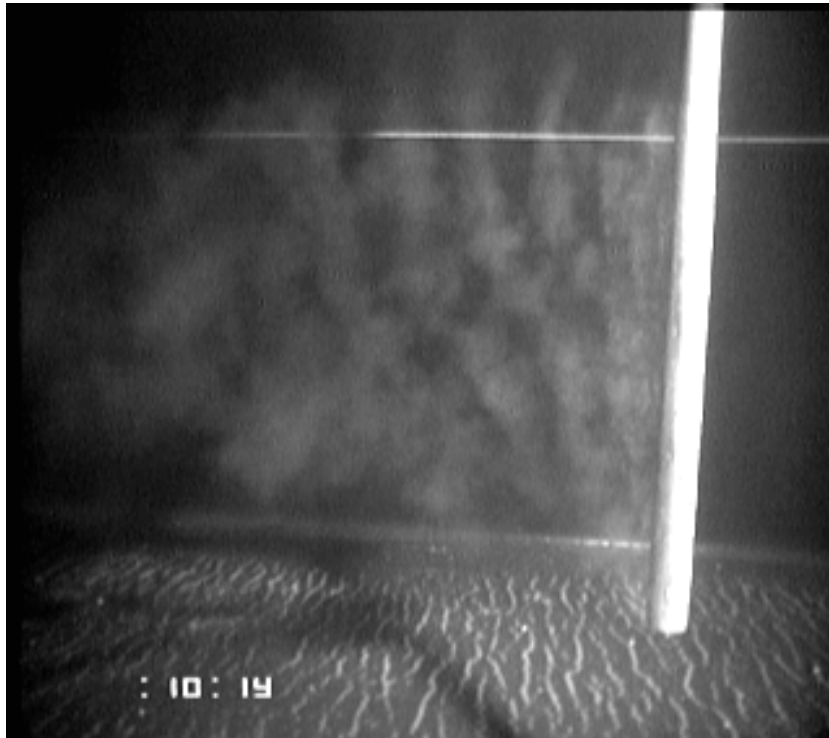


Figure 3.29: Visualization of three dimensional flow behind a single cylinder, towed at constant speed.

a possible correction for this effect is included, is presented in Figure 3.32.

By modeling the influence from the cylinder as a distribution of sources and dipoles (the free surface is accounted for by image sources and dipoles) a similar behavior as seen from the experiments can be observed. This could qualitatively be used to explain the effect, but do not give any quantitative results. This is illustrated in Figure 3.30, where streamlines in a plane parallel to the cylinder axis are drawn. The results are calculated using a 3D model.

Variation in velocity over the horizontal cross-section of the cylinder

From Figure 3.6, where the velocity profile at a distance $x/d = 5$ behind the cylinder is plotted, another important aspect can be seen. A large variation in the velocity behind a cylinder in cross-wise direction as a function of y/d is evident. Thus for a cylinder placed in the wake of another cylinder, at for instance $y/d = 0.5$ (corresponding to an angle of attack of approximately 6 [deg] at $x/d = 5$), where the sides of a cylinder with diameter d would be at $y/d = 0.0$ and $y/d = 1.0$, there will be a relatively large transversal variation in the velocity across the width of the cylinder. In addition, due to the physical size of

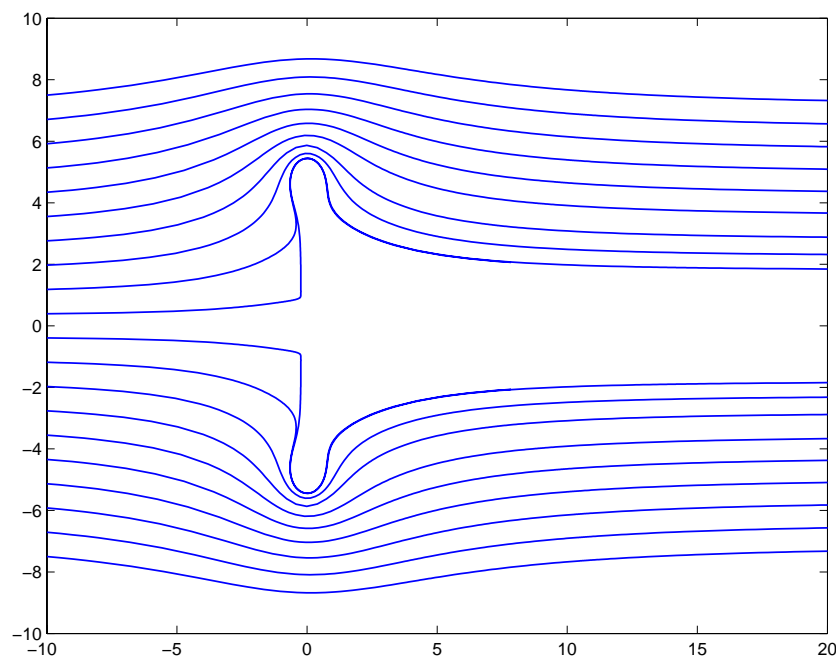


Figure 3.30: Streamlines around a cylinder in current modeled by means of dipole- and source distribution

the downstream cylinder, there will be a longitudinal geometrical discrepancy in where to calculate the inflow velocity. If for instance the second cylinder is situated five diameters behind the first cylinder, then the radius of that cylinder will amount to ten percent of the distance between the two objects. Further, the drag force is used as the comparative parameter in the presented figures, any error due to incorrect mean inflow velocity will be squared.

In Table 3.6 results for the velocity at different positions related to the center of a downstream cylinder placed in the wake of another cylinder, are presented. From the results it is evident that there is large variations in the mean “inflow” velocity on the downstream

Table 3.6: Calculated velocity at different positions related to the center of a downstream cylinder placed in the wake of another cylinder at a distance $x/d = 5$. Uniform flow, $U_\infty = 1.0$ [m/s]. U_{ref} is the calculated velocity at the center of the downstream cylinder. The model of Schlichting is used.

y/d	Center	x-0.5d		y-0.5d		y+0.5d	
	U_{ref} [m/s]	U [m/s]	U/U_{ref}	U [m/s]	U/U_{ref}	U [m/s]	U/U_{ref}
0	0.575	0.552	0.960	0.758	1.318	0.758	1.318
0.5	0.758	0.760	1.003	0.575	0.759	0.955	1.260
1.0	0.955	0.963	1.008	0.758	0.794	0.997	1.044

cylinder, depending on where on the cylinder it is calculated. The largest difference between the velocity calculated at the center of the downstream cylinder and the edge of the cylinder is in the cross-wise direction, with a difference of up to 32% for $y/d = 0$. The difference between center and $x/d = 4.5$ for $y/d = 0$ is only 4%. For $y/d = 0.5$ the decrease in velocity at $y - 0.5d$ and the increase in velocity at $y + 0.5d$ is of the same magnitude and equal to 24% and 26% respectively. While for $y/d = 1.0$, the decrease in velocity at $y - 0.5d$ and the increase in velocity at $y + 0.5d$ is equal to 21% and 4%, respectively.

Let us not be concerned directly with the difference in magnitude of the velocity, but rather the influence of this geometrical dependency of the velocity on the calculated drag force. If the variation across the cylinder width is closely linear and the minimal changes in the longitudinal direction are discarded, the effect of the velocity difference on the “inside” and “outside” of the cylinder will not have any or limited effect on the calculated drag force for the downstream cylinder.

This is only the situation for certain transversal position, when the width of the cylinder is either completely within the wake region of the upstream cylinder or completely outside of the wake region. The effect will be added up when considering several cylinders in a row. However, it is not clear how to actually account for this effect and at which point the incoming flow should be calculated. Another important discussion is where on the cylinder the largest contribution to the drag force is got, i.e. referring to the displaced area. If the function for a circle is differentiated, it is seen that the curve is relative flat from the origin up to 0.6 or 0.7 times the radius of the cylinder. This show that it will not be correct only use the velocity calculated on the “inside” and “outside”, but rather a distribution across the edge of the cylinder.

This point is more apparent when several cylinders are considered. If the inflow velocity on the cylinders are calculated at the center of the cylinder y_c and at the edge $y = y_c + / - d/2$, the resulting drag force get a small shift upwards for low y/d ratios and for increasing ratios the calculated drag actually gets smaller.

In Figure 3.31 and 3.32 results were velocity variation across the width of the cylinders and correction for three-dimensional effects is included, are presented.

As seen from the figures, there is a shift in the resulting numerical results towards a higher angle of attack is seen due to the correction for the velocity variation across the width of the cylinders. I.e. for a given angle of attack, there is a decrease in the grid drag coefficient. The effects, as expected, are largest at lower angle of attack. Including a correction for the three-dimensional effect lead to a shift upwards for the numerical results at the lowest angle of attacks.

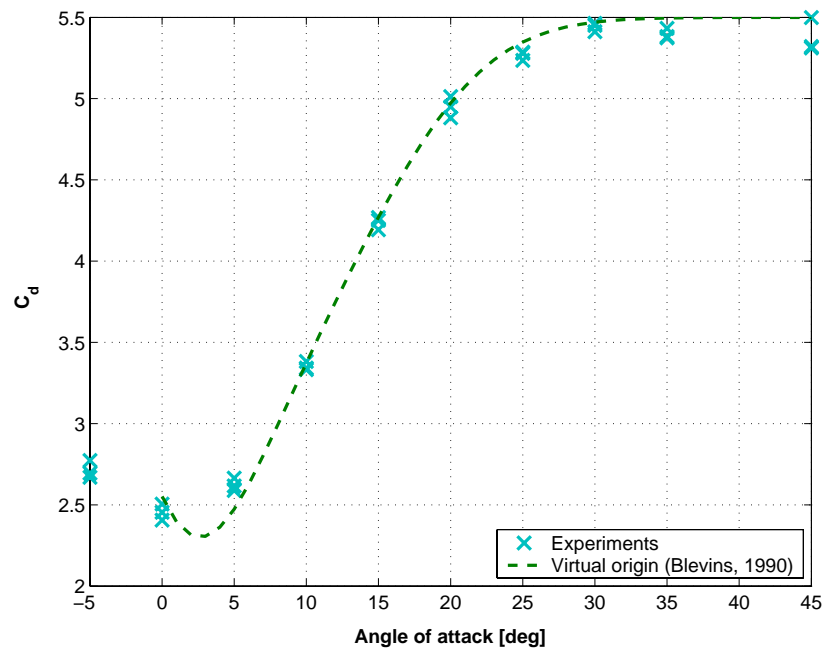


Figure 3.31: Drag coefficient for five cylinders in a row as a function of angle of attack. $s = 5d$ and the Reynolds number $Rn = 4.4 \times 10^5$. The numerical results (“Virtual origin”) account for the width of the cylinder.

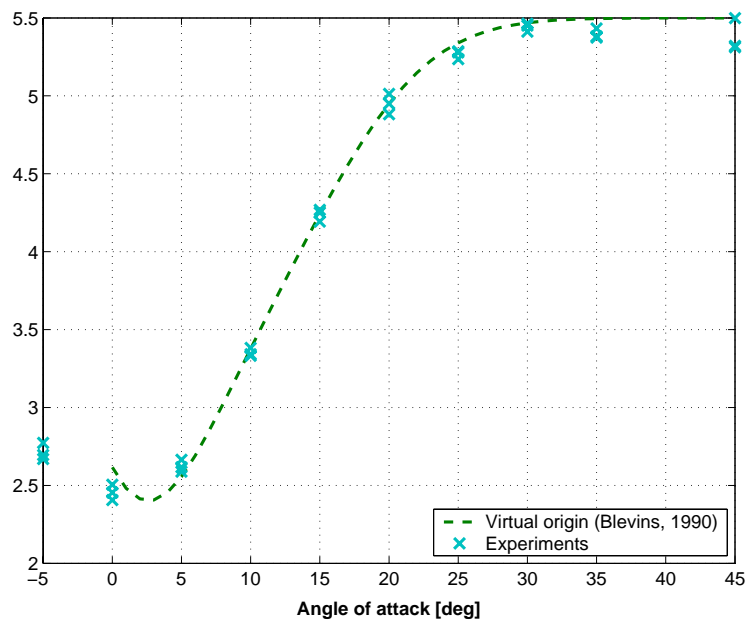


Figure 3.32: Drag coefficient for five cylinders in a row as a function of angle of attack. $s = 5d$ and the Reynolds number $Rn = 4.4 \times 10^5$. The numerical results (“Virtual origin”) account for the width of the cylinder and for three-dimensional effect by assuming only 90% effective height of the wake.

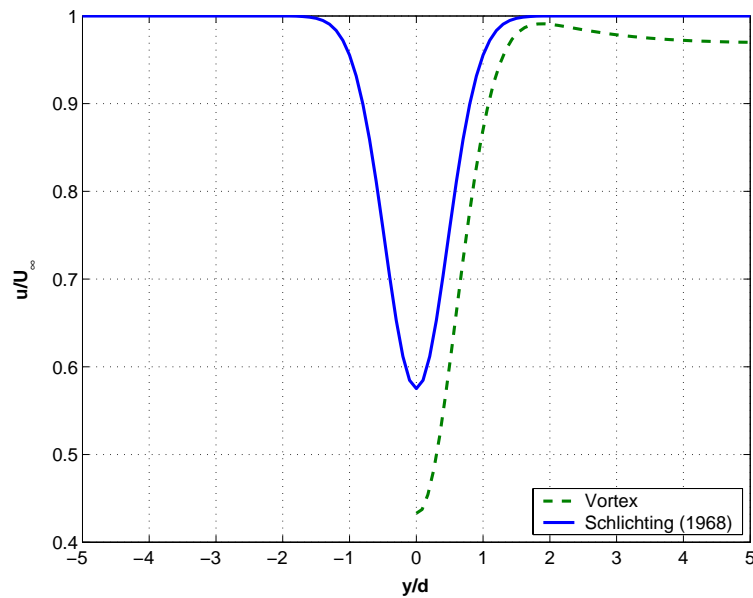


Figure 3.33: The velocity profile calculated directly from the circulation around the shedded vortices. Diameter of cylinder = 0.1 [m], uniform velocity = 1.0 [m/s], Strouhal number = 0.18 and the ratio between transversal and longitudinal vortex spacing (h_v/l_v) = 0.2

Vortex shedding

The transversal variation in the velocity behind the cylinder leads us to look for a possible explanation in the velocity variation in the wake due the generation of vortices. The velocity has been calculated directly from the circulation around the vortices, and averaged over one vortex shedding period. There is a number of uncertainties involved using this method, like the eddy shedding frequency and the ratio between the transversal and longitudinal vortex spacing, (h_v/l_v). In the near-field the h_v/l_v ratio is difficult to determine. Sarpkaya (1979) presents a figure with the longitudinal and transversal vortex spacing as a function x/d ratios. But for x/d ratios as low as in our case, the values are strongly uncertain.

Numerical results for the velocity behind a single cylinder, calculated as an average value directly from the circulation around shed vortices, are presented in Figure 3.33. The tendency of velocity profile is equivalent with the one calculated using the far wake mean velocity deficit model by Schlichting (Equation (3.10)), but the reduction in velocity is even larger and the width of the wake do not increase.

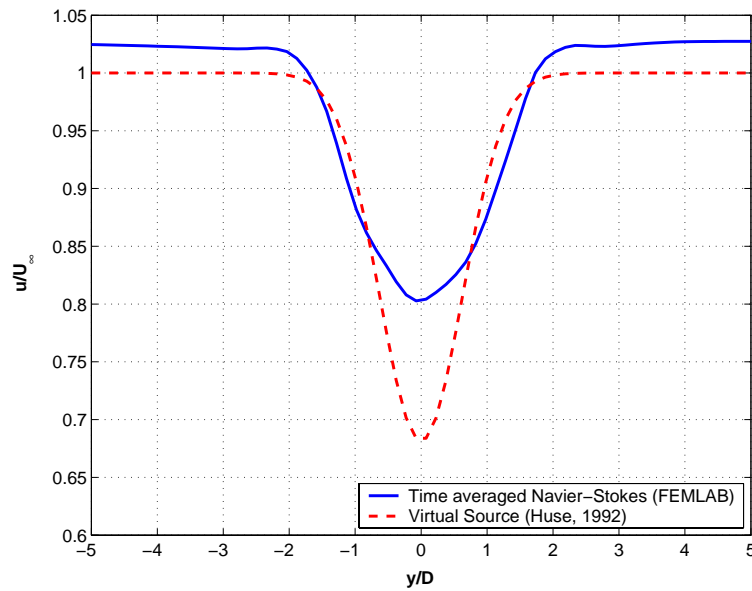


Figure 3.34: The time averaged velocity profile calculated using a Navier-Stokes solution (FEMLAB (COMSOL 2000)) and the mean wake velocity deficit model “Virtual source positions”. Reynolds number equal to 20000 and diameter equal to 1.0 [m].

CFD code

Finally the velocity deficit model is compared with results from a two-dimensional Navier-Stokes based commercial CFD code (FEMLAB (COMSOL 2000)) at $x/d = 5$. Results are presented in Figure 3.34. The discrepancy between the velocity profile calculated using the mean velocity deficit models and the time averaged velocity from the CFD code for $y/d > \approx 0.5$ is relatively small, but for $y/d = 0$, directly behind the cylinder, the difference is large.

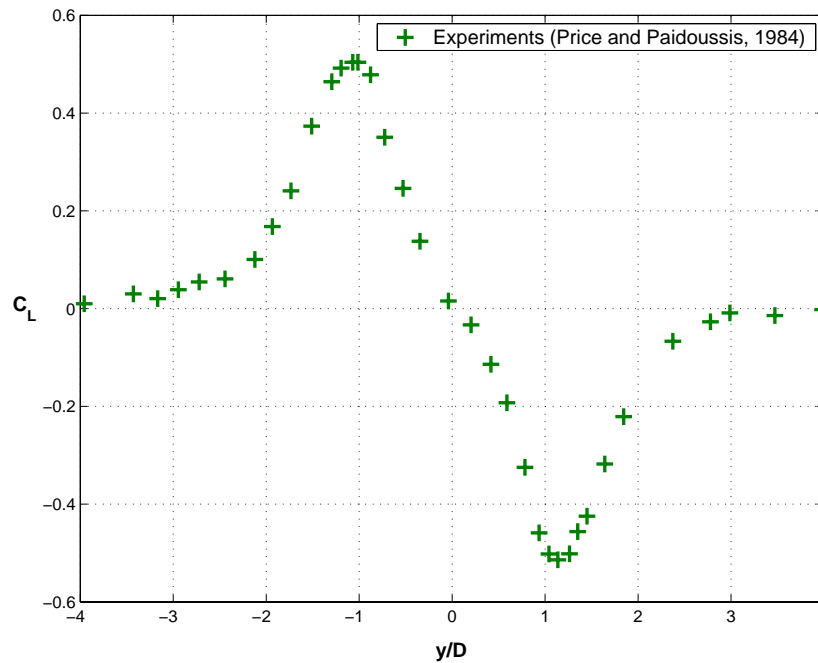


Figure 3.35: Mean lift coefficient for a cylinder in the wake of another cylinder. $x/d = 5$. $Re = 5.3 \times 10^4$.

3.5 Lift on Multiple Cylinders

3.5.1 Introduction

Price & Paidoussis (1984) carried out experiments measuring the lift force on a cylinder in the wake of another cylinder. Results are shown in Figure 3.35. As seen from the figure, the results show a large y -component, i.e. lift, of the mean force for a certain range of y/d . For positive y/d the mean lift coefficient is negative, resulting in a lift direction towards the wake axis, i.e. a negative mean lift force. This negative lift force can not be explained by the shear flow associated with the mean wake flow. For instance when a pipe is in a boundary layer flow near the sea bottom, the pipe sees a similar shear flow as the downstream cylinder experiences, but the pipe will experiences a positive lift force.

The dynamics of the wake behind the upstream cylinder has to be studied to find an explanation. The unsteadiness due to turbulence can effect the separation points of the downstream cylinder in a certain Reynolds range as earlier described. However, the negative lift force is likely to mainly be associated with the shed large scale vortices. To support qualitative explanations, a simple experiment to visualize the flow pattern around two cylinders in uniform flow was carried out.

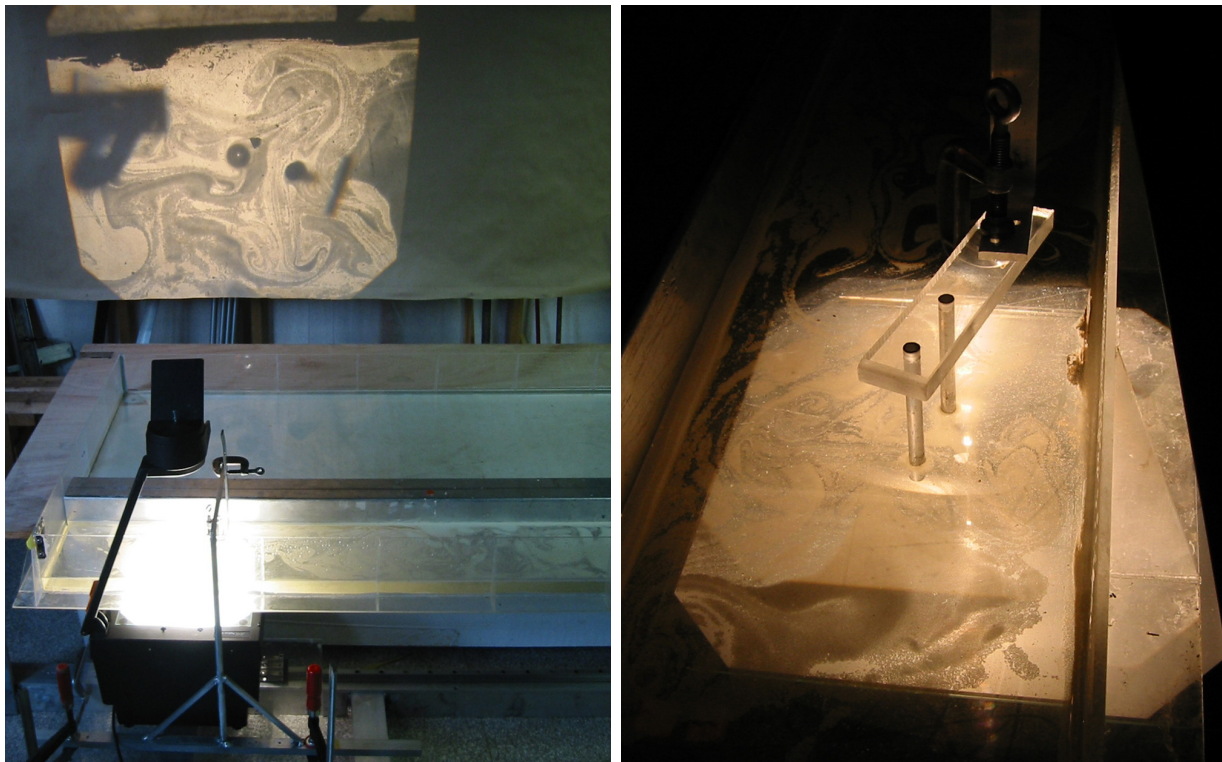


Figure 3.36: Pictures of set-up used for visualization of flow around two cylinders in a staggered arrangement.

3.5.2 Flow visualization

To visualize the flow around two cylinders in free flow, a simple set-up was made. Two plastic tubes, connected to a transparent plate were attached to a carrier. For visualization reflective particles were added to the water. An overhead projector was used to illuminate and display the view on the wall. On the carrier a standard video camera were mounted and used to film the display on the wall. The carrier was pulled by an electric motor. The set-up is shown in Figure 3.36. Due to the set-up and placement of the projector lamp, the thickness of the cylinders in the pictures from the experiment is not clear. But both the cylinders have a vertical cylinder axis. The diameter of the cylinders were 2[cm]. The available distance to move the carriage was limited, so there were some problems getting adequate pictures.

3.5.3 Results

In Figure 3.37 and 3.38 a series of pictures of the flow pattern for two different y/d ratios is shown. The pictures show two distinct occurrences. First the vortex shed from the

upstream cylinder on the same side as the downstream cylinder is placed, always goes on the side towards the wake axis (“inside”) of the downstream cylinder even for small y/d . Secondly the vortex shed on “outside” of the downstream cylinder is smaller than the vortex shed on the “inside”. The positions of the separation points are also affected.

The only known effort to explain this effect is by Zdravkovich (1985), where it is stated that the lift force is produced by the displacement of the fully formed wake of the upstream (first) cylinder, by the downstream (second) cylinder. This is believed not to be an adequate explanation of the phenomena.

The negative lift force will be sought explained in terms of the shed vortices from the upstream cylinder. The center of the downstream cylinder is assumed to have a positive y/d -value such that the vortex shed from the upper side of the upstream cylinder is incident to the downstream cylinder. The flow around the downstream cylinder is at first simplified to consist of three parts. Part 1 is the incident vortex with an image vortex inside the cylinder in order to satisfy the body boundary conditions (Milne-Thomson 1968). The vortex strength can be approximated as $2.5U_\infty d$. Part 2 is an incident mean flow associated with the mean wake flow of the upstream cylinder, evaluated at the downstream cylinder origo. Part 3 is a source in the center of the downstream cylinder to represent its own wake. The source strength is by Lagally’s theorem equal to $C_d U d$ where U is the incident mean flow velocity. The image vortex causes an anti-clockwise angular velocity of the vortex around the downstream cylinder. The result is that the vortex will get a path below the downstream cylinder. How close the vortex comes to the lower surface part and hence how strong it will affect the lift depends on the ambient vortex position relative to the downstream cylinder as well as the three flow components. This simplified analysis neglects the influence of the vortex shed from the lower side of the upstream cylinder and assumes implicitly that the y/d -values of the center of the downstream cylinder is not small. But a small y/d -values would cause nearly the same strength of the shed vortices on the upper and the lower side of the downstream cylinder, i.e. an oscillatory lift force with nearly zero mean value. The vertical force due to the vortex will change with time, but will in average be negative. Further this vortex causes an increased strength of the shed vortex from the lower side of the downstream cylinder. This adds to the negative lift. The total lift on the downstream cylinder will be oscillatory, but with a mean negative lift. With an assumption of a negative y/d -value for the center of the downstream cylinder, the arguments would be similar. The calculations explain qualitatively the y/d -dependence of the lift force.

Our analysis suggests that the y/d dependence of C_L for other x/d -values is related to the ambient path of shed vortices from the upstream cylinder. Blevins (1990), Figure 5-18 of positions of maximum absolute value of lift, supports this.

Figure 3.39 shows our experimental results for the mean lift force on 5 cylinders as function of angle of attack, α . Further, there is a similarity between the results in Figure 3.35

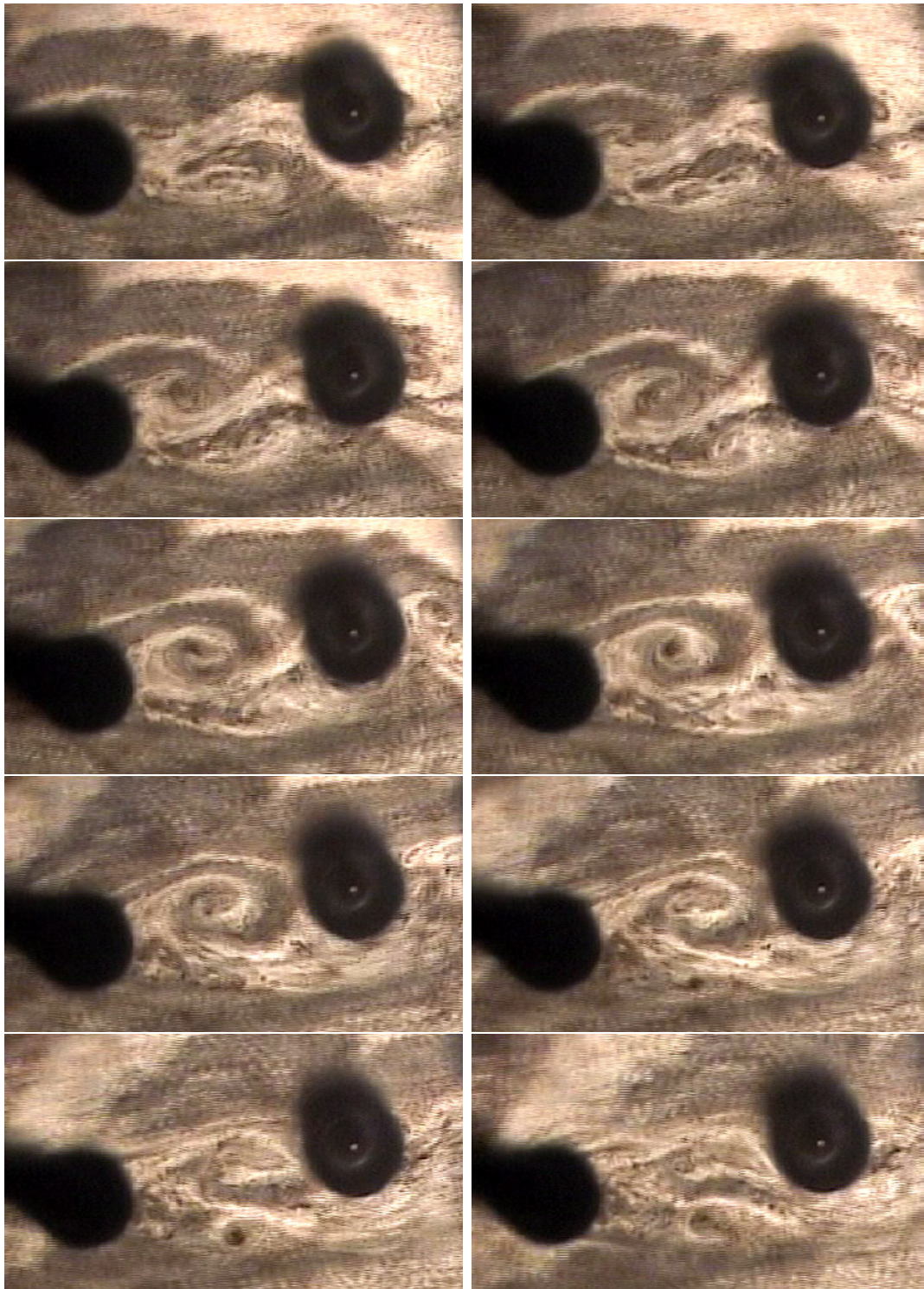


Figure 3.37: Visualization of the flow around and between two cylinders in a staggered arrangement. Flow from left to right. $y/d = 0.625$ and $Re \sim 500$.

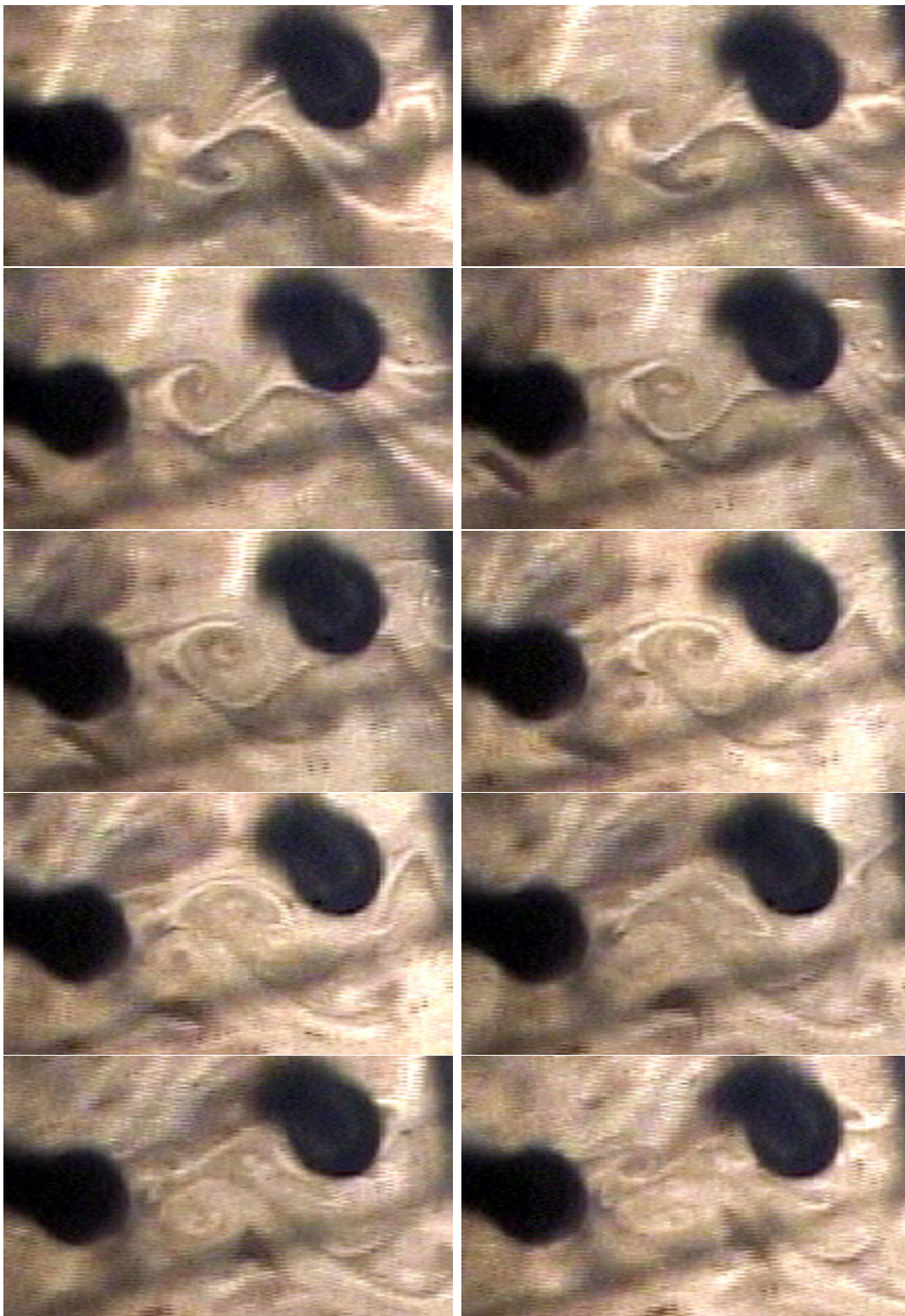


Figure 3.38: Visualization of the flow around and between two cylinders in a staggered arrangement. Flow from left to right. $y/d = 1.2$ and $Re \sim 500$.

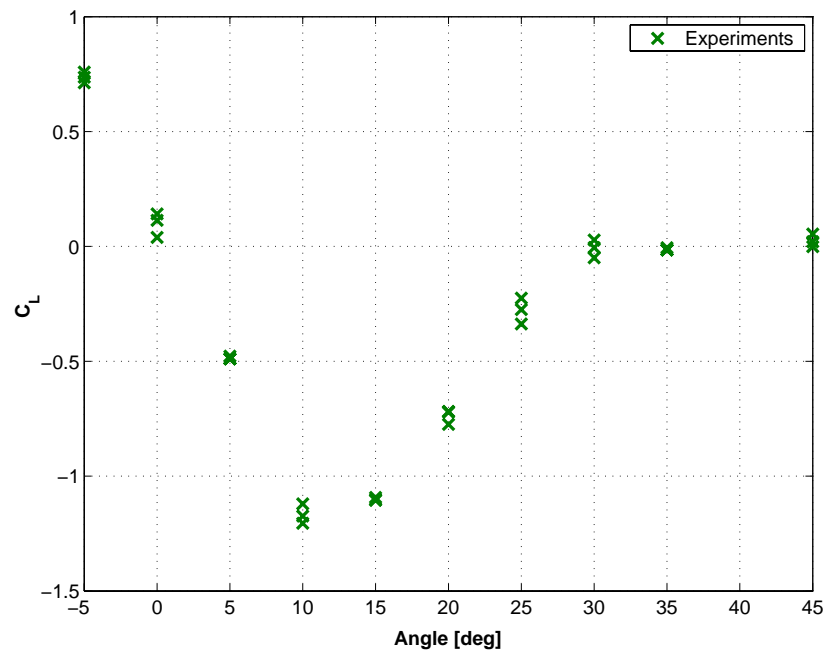


Figure 3.39: Mean lift on five cylinders in a row as a function of angle of attack, α . Same conditions as in Figure 3.28.

and 3.39, i.e. the two cylinder results can be used to explain the results for multiple cylinders.

Since the shape of a trawl is an important issue regarding fishing efficiency, and also the selectivity performance of the trawl, the investigated lift effect on cylinders in staggered arrangement becomes an important aspect when modeling a trawl. Blevins (1990) pointed out that large amplitude galloping motion can occur for a cylinder in the wake of another cylinder. This is associated with both the negative mean lift as well as the effect of the wake on the drag on the downstream cylinder. The relevance of this for a net structure has to be clarified.

Three Dimensional Net Structures

4.1 Modeling of complete structures

4.1.1 Introduction

The drag force on a three-dimensional net structure is dependent on at least three parameters, the Solidity ratio, the Reynolds number and the projected area of the net, in addition to surface and twisting of the twine material (see Figure 1.4 and 1.4). The Solidity ratio is a function of the physical dimensions of the net structure, including the diameter of the twine and knots. The Reynolds number is dependent of the diameter of the twines and knots and on the inflow velocity. The projected area of the three-dimensional net structure is either a function of the physical shape of the net structure or the angle of attack for a plane net.

But the relation is more complex than this, considering an interaction between the physical dimensions of the net structure and the flow field, and a change in the three-dimensional net structure. And not only the physical dimensions of the net structure, but also the shape and orientation between the different parts of the net will have an influence on the flow field.

The different parameters have effect on the results in two manners, as a direct influence on the calculation of the drag force and indirectly by affecting the inflow velocity. And

further the parameters have an effect on the upstream flow and the downstream flow to a different degree and magnitude. Thus the resulting flow field and the net drag force are both depending on the physical dimensions of the net structure and the fluid velocity it self.

In this chapter the different methods and models previously presented in Chapter 2 and Chapter 3 will be sought combined, together with an structural analysis to account for changes in geometry, to study flow interaction with three-dimensional net structures.

In the combined analysis, the two cases are handled separately. First a new geometry due to a uniform flow is calculated. Secondly the interaction between the net elements due to the physical generation of a wake flow behind each individual element of the net, is calculated using the “Virtual origin” model by Blevins (1990). And thirdly the influence from the net on the fluid flow is calculated by representing the wake generated by each element as source distributions along the structural element, based on the new inflow velocity calculated in step two. These three steps can then be repeated, with a corrected inflow velocity in step one. And further, the analysis can be run by any combination of the mentioned steps, for instance to only study the downstream effect or the change in geometry.

As previously stated, it is assumed that the total drag on a trawl or net structure can be calculated by adding up the drag on sub parts or elements of the net structure. And further, for constant Reynolds number, keeping the Solidity ratio constant, the total drag on the net structure will be independent on the actual diameter and mesh opening of the net. Based on this it is assumed that it is possible to model the complete three-dimensional net structure, using an “equivalent” net with larger diameter of the twine and mesh opening.

4.1.2 General modeling

The three-dimensional net structure is divided into discrete elements. The twines are modeled as separate cylinders between knots, with two-dimensional properties, allowing the interaction between them to be three-dimensional. The knots are modeled as separate spheres, with full three-dimensional properties. The modeling is illustrated in Figure 1.12. Each of the twine elements between knots can further, but do not have to, be divided into sub elements.

The inflow velocity vector will be transformed into a plane orthogonal to the cylinder axis for calculation of the drag on each individual twine elements. The cross-flow principle (Hoerner 1965) is assumed. In a three-dimensional net structure some of the twine elements will be at a low angle of attack to the incoming flow, thus the cross-flow principle is no longer valid in this cases. This is not accounted for in the present method, and will thus be a source of error in the analysis.

The total drag on the net will then become a sum of the drag of each of the individual elements, transformed back into a global coordinate system. The drag on each element is calculated as the drag on a single circular cylinder in a two-dimensional free flow, which can be expressed as $\mathbf{F}_c = 1/2\rho C_D dL|\mathbf{U}|\mathbf{U}$. \mathbf{U} is the inflow velocity vector in a plane orthogonal to the cylinder axis, $|\mathbf{U}|$ is the magnitude of the inflow velocity, C_d is the drag coefficient for the cylinder, d is the diameter and L is the length of the cylinder. The expression for the drag on a sphere in three-dimensional free flow will in a similar fashion become $\mathbf{F}_s = \pi d^2/8\rho C_d|\mathbf{U}_{3D}|\mathbf{U}_{3D}$, where $\pi d^2/4$ is the projected area of the sphere.

In the combined model, the drag coefficients and the diameter of the twines and knots, are given as input. In this manner it is possible to control both the Reynolds number of the elements and the Solidity ratio of the net structure, and even independently parts of the net structure. It is then possible to account for some of the previously discussed issues of flow interaction by controlling the drag coefficient and diameter of the twines and knots.

When calculating the interaction between the net elements due to the physical generation of a wake flow behind each individual element of the net, the direction of the downstream wake of one twine element is assumed to be in the direction of the incoming three-dimensional flow. To check if a downstream cylinder is in the wake of an upstream cylinder, the coordinates of the center point of the element is used. If the center-point of the downstream cylinder, say (x_{dc}, y_{dc}, z_{dc}) , is between the edges of the upstream cylinder, defined by the coordinates (x_{u1}, y_{u1}, z_{u1}) and (x_{u2}, y_{u2}, z_{u2}) , in the flow direction, a velocity deficit is calculated. This also imply that a velocity deficit could be calculated when only part of the downstream cylinder is in then wake of a upstream cylinder. And similarly that no velocity deficit is calculated, even though some part of the cylinder could actually be in an upstream wake. This will also be a source for error in the calculations.

For calculation of the influence from the net on the fluid flow represented by the the source distributions along the structural element, solely the distance between the center of the elements is considered.

4.1.3 Structural modeling

A straight forward structural model has been used to calculate the geometry of the net due to the incoming flow, allowing for a fluid-structure interaction. The structural model is based on a FEM formulation, using truss elements to model the twines between knots. In addition to the input required for hydrodynamical analysis, the axial stiffness and weight of the material for the net structure is given. The length of the elements is calculated as the distance between nodes, thus no geometrical elasticity due to excess length of twines is included. Geometrical elasticity can be accounted for by changing the material stiffness.

Each of the elements in the hydrodynamical model, including any sub-elements (see Section 1.4), can further be divided into structural sub-elements, allowing for the elements in the net structure not to take compression. The extra node introduced in this case is not treated as a knot, and no extra loading is calculated. The calculated load on each element is distributed with evenly between the two nodes associated to the element. External loads include calculated drag force as described, weight of the net structure and any given load.

A structural description and analysis of the net allow for calculating a new geometry of the net due to the incoming flow. Based on this new geometry, a new correction of the inflow can be calculated and it is possible to continue on until a specified convergence criteria is met. The criteria is that the relative difference in the geometry between two steps should be smaller than a given number, typically say 1.0×10^{-5} . Bearing in mind that both the part involving calculating the new inflow and the calculation of the new geometry involves solving non-linear equations, this ends up being a time consuming task.

The numerical model of a net structure will, as described, consist of fewer elements or twines than the real net structure. This implies that one twine in the numerical model represent a number of twines in the real net structure. To calculate the axial stiffness for the numerical model, the principle that the axial stiffness (the E -modulus times the area of the element) for the numerical twine is equal to the sum of the axial stiffness for the represented twines, is used. Thus, the axial stiffness of one numerical twine is equal to the axial stiffness of a number of twines. Using the prefix m for the numerical model and f for the properties of the real net structure (full scale), the axial stiffness of the numerical twines can be expressed as follows:

$$(EA)_m = n_f/n_m(EA)_f \quad (4.1)$$

where E is the modulus of elasticity for the material, n_m and n_f is the number of twines that represent the same part of the net structure in the numerical and in the real net structure and A is the cross sectional area of one single twine. The cross sectional area of one single twine is proportional to the square of the diameter of the twine, but at the same time the hydrodynamical load on the twine (or element) is dependent on the diameter of the twine. Thus using the diameter of the twine to both calculate the cross sectional area for stiffness properties and for load calculations, will give modeling difficulties. Therefore is the axial stiffness EA of the twine given directly as an input, allowing for a independent handling of dimensions between the hydrodynamical and structural model. Based on the relation between model an full scale as described in Equation (4.1), it is then the E -modulus of the numerical model which is altered. The relation between the E -modulus for full scale and the numerical model can be expressed as:

$$E_m = E_f n_{tf}/n_{tm} d_{tf}^2/d_{tm}^2 \quad (4.2)$$

where m denoted model scale, f full scale and d_t is the diameter of the twine.

What E -modulus to use for the full scale net structure or rather how to account for the effect that a twine is not a solid piece of material, but is made of filaments by either twisting or braiding, is not clear. The manufacturing of the net and twine will introduce a slack in the twine. When elongated, the excess slack will be “taken out” and the knots will be tightened. In addition is the material in it self highly non-linear for large elongation. Nets and ropes are often made of polypropylene or nylon. The E -modulus for this material is also varying due to manufacturing and material compositions, but is often assumed to be in the range of 1000 - 1500 [MPa]. But experiments performed by simply measuring the elongation of part of a net as a function of force, indicate that this is a too high value to use (Slaattelid 1993). An E -modulus in the range of 50 - 400 [MPa] as a function of the elongation, is likely to be more correct. Then the special properties and effect of the manufacturing of the net is accounted for.

4.2 Plane nets with elasticity

As previously described, geometrical elasticity of the net and net structure is important. A contribution to the geometrical elasticity is also the tightening of the knots, in a net structure after submergement in water and loading. This will contribute to an increase in the length of the twine between the knots. It will not be possible during experiments to avoid some deformation of the net itself, which again will not only have an influence on inflow of the net and thereby the resulting drag force, but also on the “effective” angle of attack α . Due to this it is important to include elasticity and the ability to calculate geometrical changes due to the load, as a part of a model to calculate load and changes in the flow field due to a net structure. Decreases diameter of the twine element due to elongation, is not accounted for in the calculations. It is believed that this effect has much less influence on the total drag force than the change in geometry due to the elasticity.

To illustrate the effect of elasticity, a simple plane net is used. The drag is calculated at different angles of attack and elasticities. A net used by Rudi et al. (1988) (see Section 1.3) is used as the real net structure to be modeled. The plane net has square mesh structure, side length of 1.5 times 1.5 [m], Solidity ratio of 0.243, $d_t = 1.830$ [mm] and a half mesh size $\lambda = 15.5$ [mm]. With $\lambda = 15.5$ [mm], a 1.5 [m] wide net will have approximately 97 twines along one side. In the numerical model the net is modeled using 21 twines along one side. Thus, to keep the Solidity ratio at 0.243, a diameter of the twine $d_{tm} = 9.1$ [mm] (m prefix for model) is used. Assuming an E -modulus for the twine of 1200 [MPa], will by Equation (4.2) give an equivalent axial stiffness for each of the modeled twines equal to 1.45×10^4 . And similarly if an E -modulus of 150 [MPa] is assumed, this corresponds to an axial stiffness of only 1.83×10^3 . A drag coefficient of 1.2 and 2.0 is used for the twine and knot respectively.

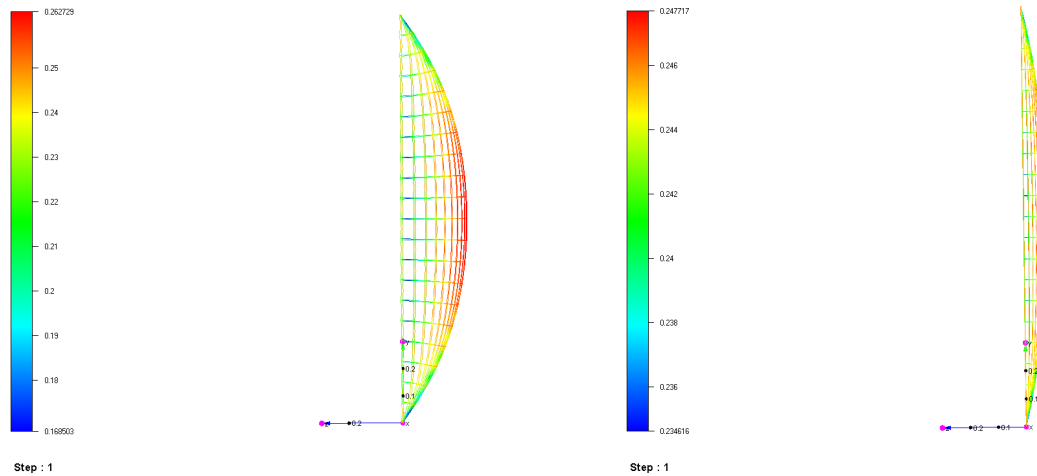


Figure 4.1: Resulting geometry seen from the side for two plane nets, attached along all sides, with an axial stiffness of 1.83×10^3 and 1.45×10^4 for the net to the left and right, respectively. The nets are situated at a 90 [deg] angle of attack to the incoming flow of 1.0 [m/s], from left to right. Both nets have a Solidity ratio of 0.243 and have a side length of 1.5 times 1.5 [m].

Figure 4.1 show the final geometry for the plane net with two different axial stiffnesses and it is clearly seen that the final geometry is highly dependent on the stiffness. The displaced area to the incoming flow is directly linked to the geometry. The total drag of the structure is then a function of the resulting geometry and further is thus a function of the axial stiffness.

In Figure 4.2 results for the net drag coefficient, C_d , at three different angles of attack, is presented as a function of the axial stiffness of the individual twines. Effects of downstream flow correction, but not upstream correction, is included. At the two highest angles of attack, 60 and 90 [deg], there is a distinct relation between the axial stiffness and the calculated net drag coefficient. The relation is not that strong for the angle of attack of 30 [deg] when the flow is more in plane with the net panel, and the drag coefficient is actually decreasing with increasing axial stiffness. When the stiffness of the net is low the net get a different geometry such that a larger part of the net will be inclined to the inflow and since the model include a correction for the downstream influence, a larger part will be subject to decreased flow.

Another interesting observation is the difference in “response pattern” related to the attachment of the plan nets and orientation of the meshes. A net panel with a diamond mesh structures is also analyzed, with same main properties as the net panel with square meshes, but with twice as many meshes. To keep the solidity ratio at 0.243 , the diameter of the twine is set equal to 6.1 [mm].

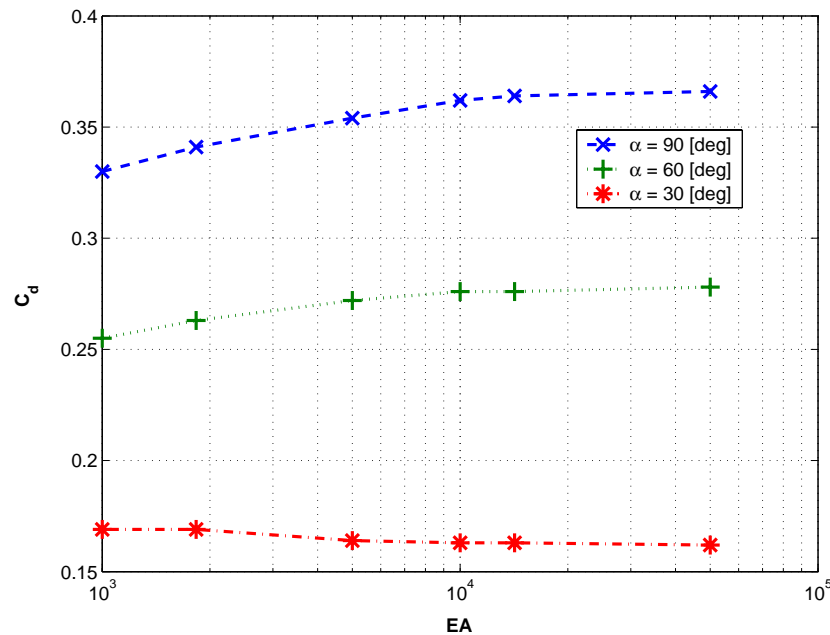


Figure 4.2: The drag coefficient of a plane net with a Solidity ratio of 0.243 and a side length of 1.5 times 1.5 [m], as a function of axial stiffness of a single twine at different angles of attack. $U_\infty = 1.0$ [m/s]. Logarithmic x-axis.

It is evident when looking at the resulting geometry for the plane net with diamond mesh structure in Figure 4.3, that it is less influenced by the elasticity of the material and twine, than the plan net with square mesh structure, due to the diagonal twines from corner to corner which is restraining the plane net from deflecting.

These results show that it is important to include elasticity in the model and to be able to account for the changes in geometry, but also indicate that it is difficult to, in detail, compare numerical and experimental results for flexible net structures, even as simple as a flat panel, since the elasticity of the setup in the experiments or full scale always will be an important source for uncertainties. This also illustrate some of the difficulties involved in modeling a net structure, that the load and response is both linked with the properties of the net, the geometry, but also how the net panel is attached, in corners or along sides.

4.3 Net cages

To further investigate the effect of elasticity, other factors and to verify the program, numerical analysis of net cages has been carried out. Two circular cages have been used, one with a diameter of 5 [m] and 5 [m] depth and one with a diameter of 1.435 [m] and

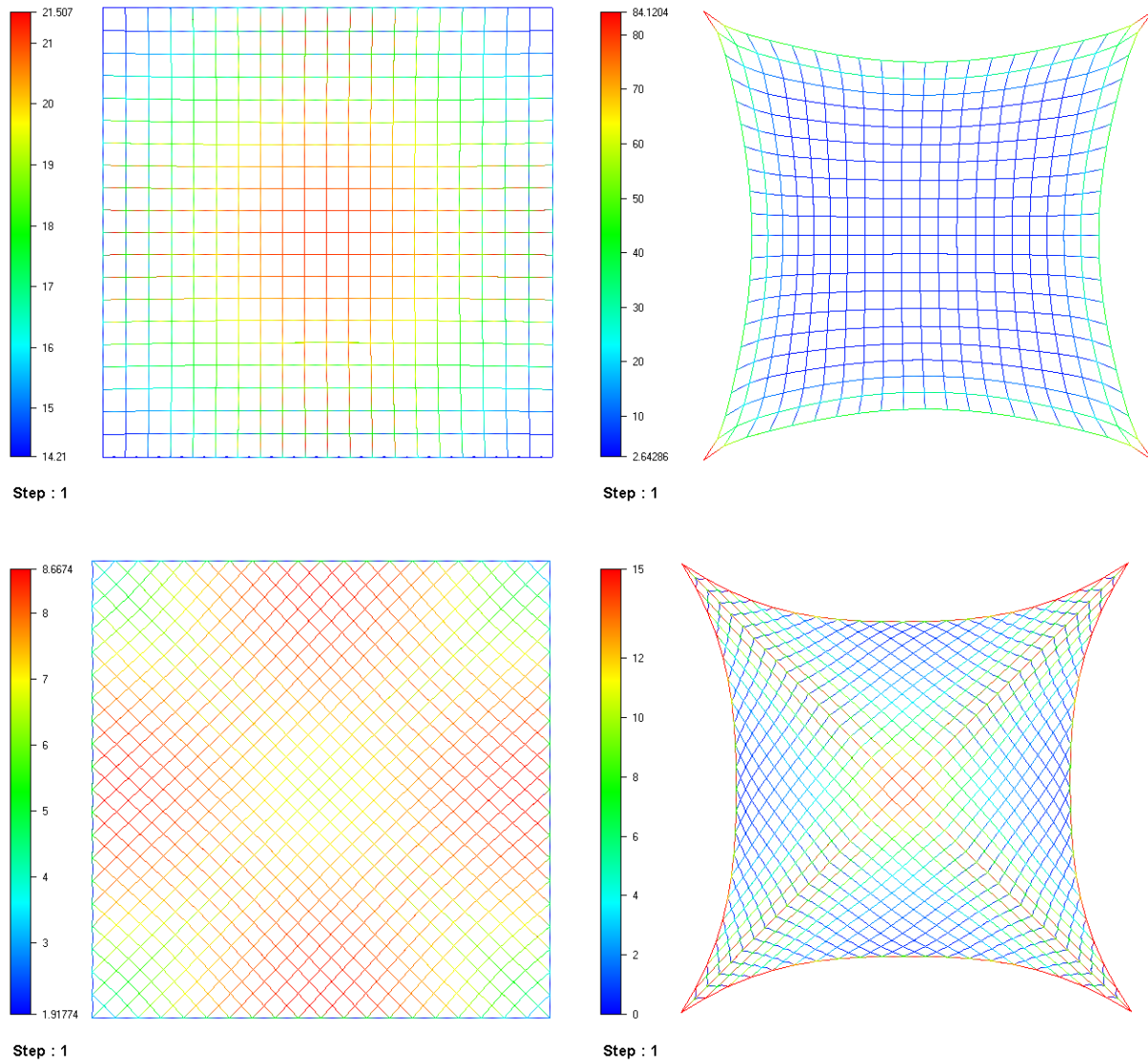


Figure 4.3: Resulting geometry seen from the side for two plane nets with different attachments. Both nets have a Solidity ratio of 0.243 and has a side length of 1.5 times 1.5 [m]. $U_\infty = 1.0$ [m/s]. Colors indicate tension in the twines as [N]. Note different color scale.

Table 4.1: Properties for the net cages used for numerical analysis. $d_{t/k}$ and $Cd_{t/k}$ diameter and drag coefficient of twine and knot.

Cage no.	Diam. [m]	Circum. [m]	Depth [m]	Sn	d_t [mm]	Cd_t	d_k [mm]	Cd_k	No. of twines	
									circ.	height
1	5.0	15.7	5.0	0.25	62.5	1.4	62.5	2.0	32	10
2	1.435	4.5	1.435	0.225	16.1	1.15	24.2	1.0	30	10

similarly 1.435 [m] depth. The properties of the last net cage is chosen to be equal to the properties of a net cage tested at the North Sea Center Flume Tank in Hirtshals (Enerhaug 2004). The flume tank is described in Appendix B. The model used for the experiments was composed of a hoop (or ring), a net and a number of weights attached to the net. The top of the net was mounted on the hoop, which was kept in a fixed position during each test. The weights were suspended around the bottom opening of the net, in order to stretch the net and maintain its shape under the influence of water flow. The total number of meshes in circumferential direction was 252 and 81 meshes high. The netting is knotless with a mesh size of 32 [mm] and twine thickness of 1.8 [mm]. When this netting was mounted on the hoop as square meshes, the solidity ratio of the netting became 0.225. Three different sizes of weights were tested, with a total bottom weight of 4.9, 7.3 and 9.8 [kg] in water. The results are presented as total drag force, and are not non-dimensionalized. The reason for this is that there is no obvious dimension to use for non-dimensionalizing and the discussion is not limited due to this.

Further are results for both net cages verified against results from the computer program *Notdrag* (Aarsnes & Rudi 1989b, Aarsnes & Rudi 1989a), which are a computer program for calculating the drag force on net cages or a system of net cages, including the effect of deformation of the net cages and reduction in water flow due to preceding net panels. *Notdrag* is using an empirically developed method based on the work by among others, Rudi et al. (1988), Aarsnes et al. (1990) and Løland (1991).

The properties of the net cages are presented in Table 4.1 and an illustration of the two net cages are shown in Figure 4.4. The bottom of the net cage is not modeled.

4.3.1 Net cage elasticity and bottom weight

Net cage no. 1 has been analyzed giving the numerical model different properties, like axial stiffness and bottom weight. Bottom weight is weights attached to the bottom of the net cage, which is a necessity when using net cages for fish farming to avoid deformation and reduction of the available space for the fish. The three different weights used for the analysis can comparatively be seen as low, normal and high weight distribution along the

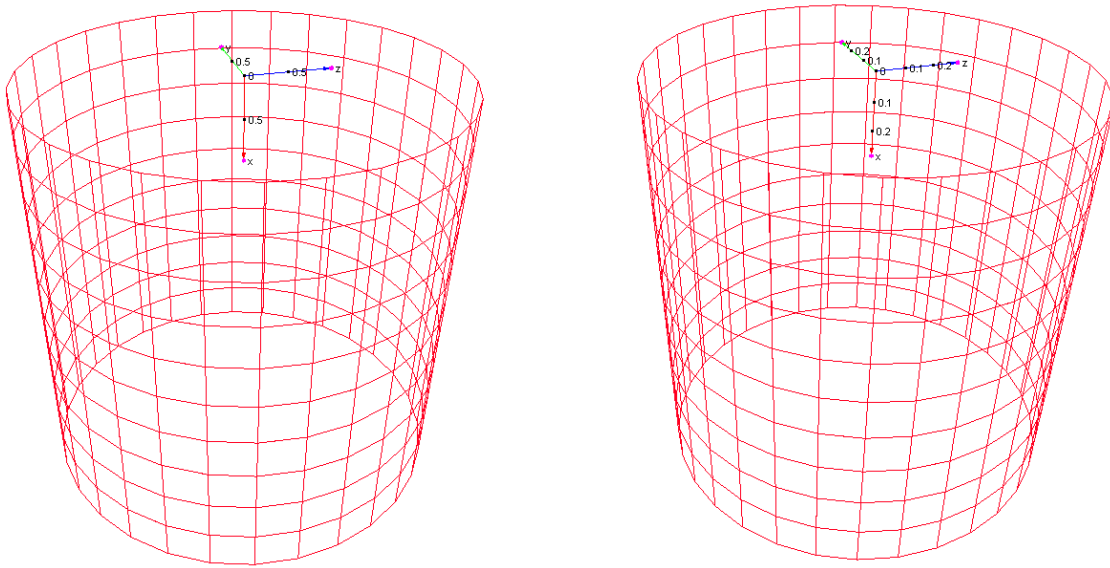


Figure 4.4: Illustration of the net cages used for numerical analysis. Net cage no. 1 to the left with a diameter of 5 [m] and net cage no. 2 to the right with a diameter of 1.435 [m]. Further properties in Table 4.1.

circumference of the net cage relative to what is used for net cages in open water fish farming. Results are presented in Table 4.2 and Figure 4.5. The numerical analysis has been carried out with different methods and corrections, which are described in the table.

The following trends can be interpreted from the results:

- There is a good agreement between the calculated drag force using the presented method and the drag force calculated using the computer program *Notdrag*.
- Inclusion of an elastic model reduces the calculated drag force.
- Inclusion of a downstream flow correction, allowing for a flow reduction, also reduces the calculated drag force.
- Increasing weight distribution increases the calculated drag force.
- The difference in absolute axial stiffness of the net cage only to a small degree influence the calculated drag force.
- There is only a small difference in the calculated drag force for the case “Stiff with wake” and the case “Elastic with wake” and a bottom weight of 100 [kg].

Since the computer program *Notdrag* uses an empirically developed method based on experimental results, the results can be assumed to be fairly accurate. The agreement achieved is

Table 4.2: Drag force [N] on a circular net cage with different properties and models. Circumference 15.7 [m], depth 5.0 [m], solidity factor 0.25 and uniform velocity 0.25 [m/s].

Case	Bottom weight [kg]			Description
	30	50	100	
Stiff no wake	673.6	673.6	673.6	No structural analysis is included and no flow correction is applied.
Stiff with wake	531.0	531.0	531.0	No structural analysis is included, but downstream flow correction is applied.
Elastic no wake	447.2			Structural analysis allowing for a change in the shape of the net cages is included, but no flow correction is applied.
Elastic with wake, EA = 3.1×10^3 [N]	404.8		551.1	Structural analysis allowing for a change in the shape of the net cages is included and downstream flow correction is applied.
Elastic with wake, EA = 2.5×10^4 [N]	402.4	466.2	531.8	
Elastic with wake, EA = 1.0×10^5 [N]	402.5		519.8	
<i>Notdrag</i>	400.8	457.7	504.0	Results calculated using the computer program <i>Notdrag</i> .
Ratio of elastic with wake/ <i>Notdrag</i>	1.00	1.02	1.06	Ratio between numerical with EA = 2.5×10^4 [N] and results obtained by <i>Notdrag</i> .

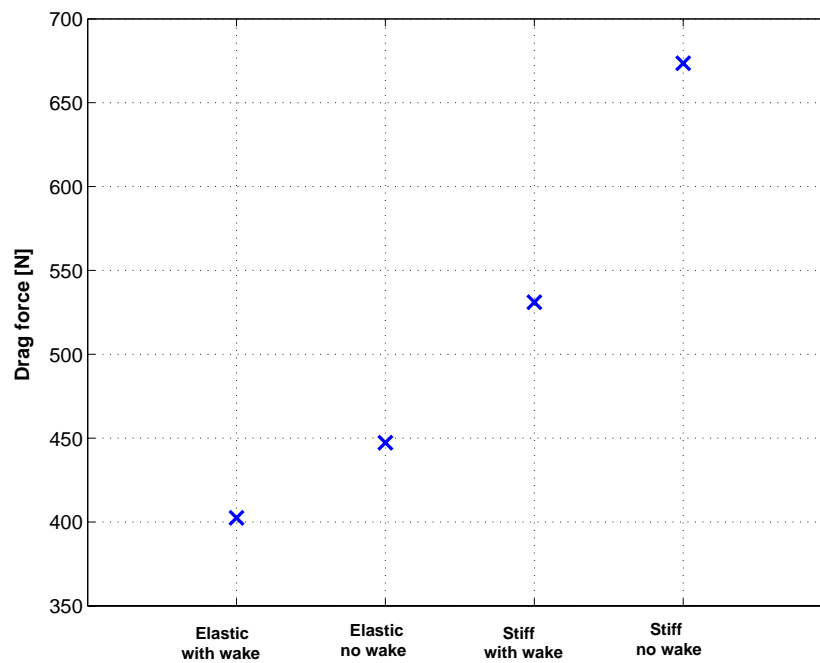


Figure 4.5: Total drag for net cage with a circumference 15.7 [m], depth 5.0 [m], solidity factor of 0.25, bottom weight of 30 [kg] and uniform velocity 0.25 [m/s] for different analysis cases.

promising and considered acceptable. And the agreement for the net cage it is better than what previously have been achieved for single net panel (Section 2.8), where mainly the upstream effects were important and considered. Based on the satisfactory agreement, it is assumed suitable to discuss other aspects obtained only by numerical analysis using the presented method.

The conclusion from the obtained results is that both inclusion of an elastic model (structural analysis) and a correction for downstream flow effects are important. Any flow through a net with a certain solidity ratio will be reduced in magnitude. A net downstream of another net will then encounter a flow of less velocity. Thus the aft or downstream part of the net cage relative to the flow direction will see a lower flow velocity than the front part and then the total drag force for the net cage will be reduced. This effect will increase with increasing number of net cages in-line, and is actually an important effect to consider when locating a fish farm to assure enough flow of oxygen and clean water. The elastic model is accounting for the effect that when the net cage is exposed to current, the net will deflect horizontally and thus elevate vertically. The result is that the effective exposed area of the net cage is reduced and thus the drag force is reduced.

Both these effects are illustrated in Figure 4.6 where the four different cases are presented with the net cages seen from above. In the figure the resulting shape after analysis and color coding representing the inflow on each of the elements are shown. The results are

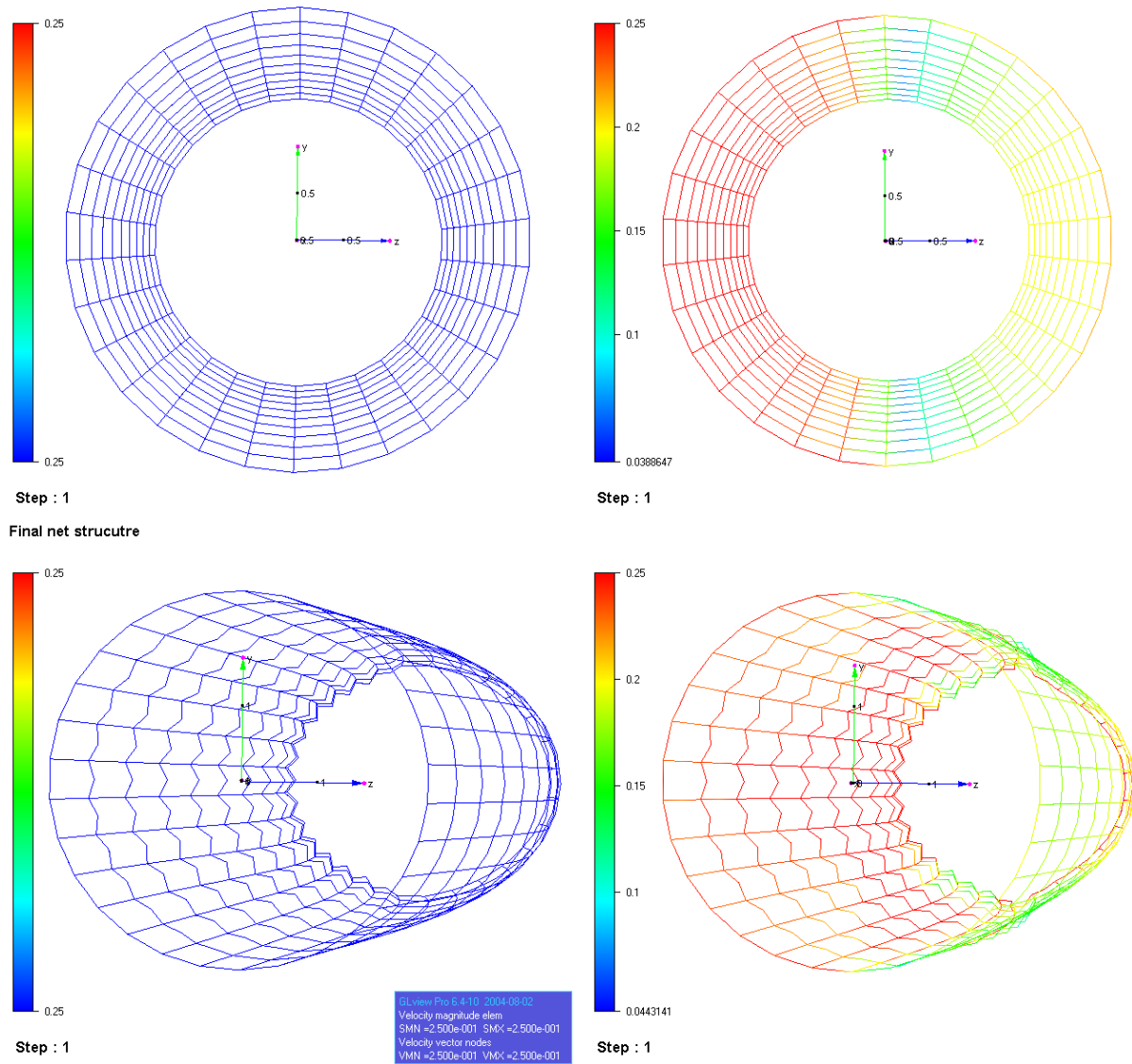


Figure 4.6: Illustration of resulting geometry and color coding of inflow velocity ([m/s]) on each element for a net cage. Circumference 15.7 [m], depth 5.0 [m], $S_n = 0.25$, $U_\infty = 0.25$ [m/s] (from left) and $EA = 2.5 \times 10^4$ [N]. Results for four different cases are shown, “Stiff with no wake” upper left, “Stiff with wake” upper right, “Elastic with no wake” lower left and “Elastic with wake” lower right.

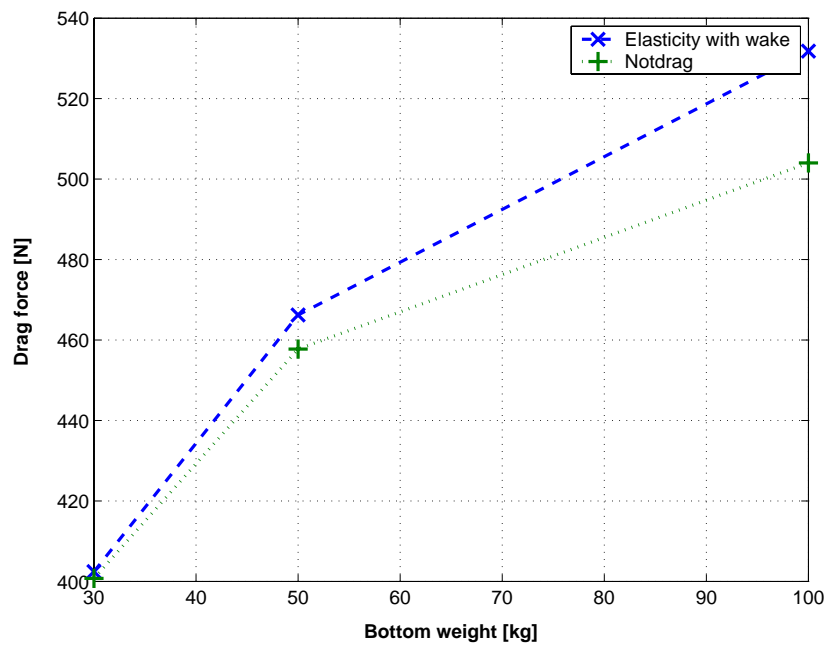


Figure 4.7: Total drag on a net cage as a function of bottom weights. Circumference 15.7 [m], depth 5.0 [m], $S_n = 0.25$, $U_\infty = 0.25$ [m/s] and $EA = 2.5 \times 10^4$ [N].

obtained with a total bottom weight of 30 [kg]. In the figures, the flow is in the positive z-direction, from left to right. It is clear from the figure that there is large deformation of the geometry, as well that the inflow velocity on each of the elements is highly influenced by any preceding elements.

At the same time, when looking at the results for different bottom weights, it is evident that the amount of bottom weight attached to the net cage also has a large influence on the total drag force. The total drag force as a function of the bottom weight are shown in Figure 4.7. There is an increase in total drag on the net, dependent on the elasticity of the net, of approximately 30% from the lowest bottom weight to the highest. The reason for this is of course that with increasing bottom weight, the deflection of the net becomes smaller. Increasing bottom weight will also tend to stretch the net, making the net cage deeper, which also contribute to a larger area of the net and thus drag force. This is further illustrated in Figure 4.8, where resulting geometry for the net cage with a total bottom weight of 30 and 100 [kg] are presented.

The result for drag force on a single net panel, especially at a angle of attack of 90 [deg], displayed a relative high dependency on the elasticity, with an increasing drag force with increasing axial stiffness. When the net is arranged as a net cage, this is no longer the situation. Total drag on the net cage for two different bottom weights, as function of the axial stiffness in the net is presented in Figure 4.9. This effect is it not possible to recreate using the computer program *Notdrag*, because the elasticity in the net structure is not

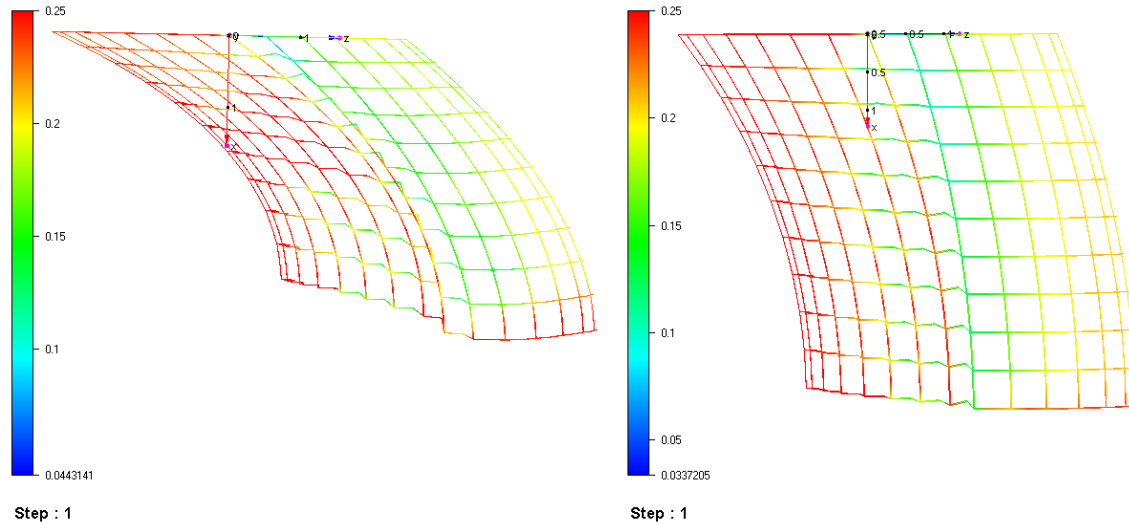


Figure 4.8: Illustrations of resulting geometry for two different total bottom weights, 30 [kg] to the left and 100 [kg] to the right. Circumference 15.7 [m], depth 5.0 [m], $S_n = 0.25$, $U_\infty = 0.25$ [m/s] and $EA = 2.5 \times 10^4$ [N].

included in the model, only the deflection of a plane net.

For the lowest bottom weight the drag force is approximately independent of the axial stiffness, but with a total bottom weight of 100 [kg], the total drag on the net cage is actually increasing with decreasing stiffness. The likely explanation for this is that for decreasing stiffness, the net becomes more flexible and the elongation will be larger than for a more stiff net. Thus for decreasing axial stiffness, the exposed area of the net cage increases because the bottom becomes deeper, and then the total drag force increases. And this effect will have larger significance with increasing bottom weight, i.e. an explanation to the difference between the results for 30 and 100 [kg] bottom weight.

4.3.2 Experimental results

Net cage no 2 (Table 4.1) has been analyzed as means to verify the drag force on the net and the resulting geometry. Drag force as a function of flow velocity, amount of bottom weights, bottom weight configuration as well as pictures of the net cage under load, has been available from the experiments (Enerhaug 2004). An other drag coefficient has been used for this net cage compared to the previous one. The argument for this is that the net used in the experiments where of the “knotless” type, with a structure like the net to the right in Figure 1.4, while the net used in the experiments which are the basis for the computer program *Notdrag* where of the type to the left in the figure, with knots and

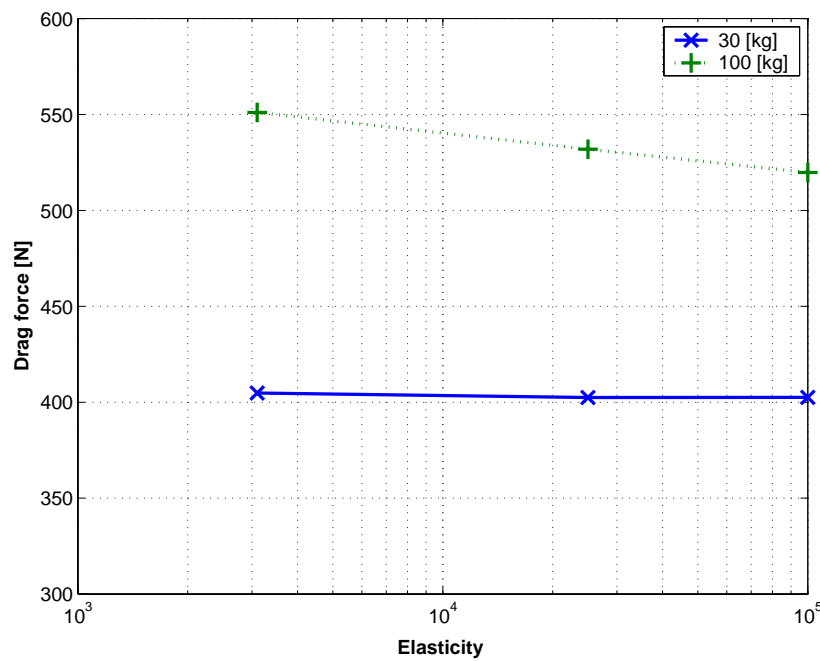


Figure 4.9: Total drag on a net cage as a function of axial stiffness and different bottom weights. Circumference 15.7 [m], depth 5.0 [m], $S_n = 0.25$, $U_\infty = 0.25$ [m/s].

different plating of the twines. The experiments, as well as the numerical results do not include a bottom in the net cage. The presented experimental results (Enerhaug 2004) for the net cage is corrected for the drag on the hoop and the bottom weights. Only numerical results including both elasticity and downstream flow correction is presented. Results for two different flow velocities, bottom weights and axial stiffness in the model, are presented in Table 4.3. In the experimental setup there were used 16 bottom weights. This is simulated in the numerical model by applying a downward force at every second twine around the bottom. With the properties of the numerical model as described in Table 4.1 the two values for axial stiffness, 1000 and 8000, correspond to a axial stiffness of the net cage used in the experiments of approximately 50 [MPa] and 400 [MPa] respectively. Thus some geometrical elasticity is assumed.

There is a satisfactory agreement between the numerical results for total drag force and the results from experiments, especially for the lower velocity. For this case also, results with two different stiffnesses are presented to illustrate the importance and difficulties relegated to this parameter. Refer to earlier discussions in Section 4.1.3. For all combinations of total bottom weight and uniform flow, the effect of numerical elasticity is small, with a maximum difference of approximately 5%. For the case with a uniform flow of 0.25 [m/s], both for the experiments and the numerical results, there is small differences in total drag force as a function of bottom weight and the difference is highest for the case with lowest stiffness. In the experiments, there is actually measured a decrease in the total drag force

Table 4.3: Drag force [N] on a circular net cage (net cage no 2) compared to experiments (Enerhaug 2004). Circumference 4.5 [m], depth 1.435 [m], solidity factor 0.225.

Flow velocity [m/s]	0.25		0.33	
Bottom weight [kg]	4.9	9.8	4.9	9.8
Elastic with wake, EA = 1000 [N]	34.2	37.2	52.6	62.2
Elastic with wake, EA = 8000 [N]	34.4	35.7	51.7	59.2
Notdrag		37.8		63.0
Experiments	34.9	33.3	50.2	54.4
Ratio of elastic with wake. EA = 8000/ Experiments	0.99	1.07	1.03	1.09

on the net cage. This could be due to slightly different inflow conditions for the two cases in the experiments. For the higher uniform flow, the functionality with total bottom weight is more apparent and is also higher in the numerical than in the experimental results. It is also interesting to note that calculated drag from the computer program *Notdrag* is 63 [N] for this configuration. But this result also include the added resistance due to the bottom, which is not the included in the experiments or the numerical analysis.

Figure 4.10 show a picture of the net cage during the experiments in the flume tank and an illustration of the resulting geometry from the numerical analysis with equal properties. The picture is not taken perpendicular to the net cage and some optical distortion will occur in the picture. Measuring the horizontal distance at the top, which should be equal to 1.435 [m] and using this as the scale to calculate the height at front and aft of the net cage when loaded, the result from the experiments are 1.32 [m] and 1.39 [m], respectively. Corresponding depths from the numerical analysis are 1.28 [m] at the front and 1.38 [m] at the aft. This is regarded as a good agreement. In Figure 4.11 the numerical results are imposed on top of the picture from the experiments. Some of the characteristics of the shape is recreated by the numerical analysis, and the folding of the net between the attachment points for the bottom weights can be seen.

Even though the drag on the bottom weights from the experiments are removed from the presented total drag results, they will influence the geometry of the net cage in the picture. Further is the bottom weights in the experiments connected in 16 discrete points, which makes the net get vertical folds. It is likely that this also will have an effect on the total drag force. For the numerical model the bottom weights are modeled as a downward force at every knot at the bottom part of the net cage, which it is 32 of in the model. Thus the numerical model do not to the same degree has the ability to account for this folding between the vertical twines.

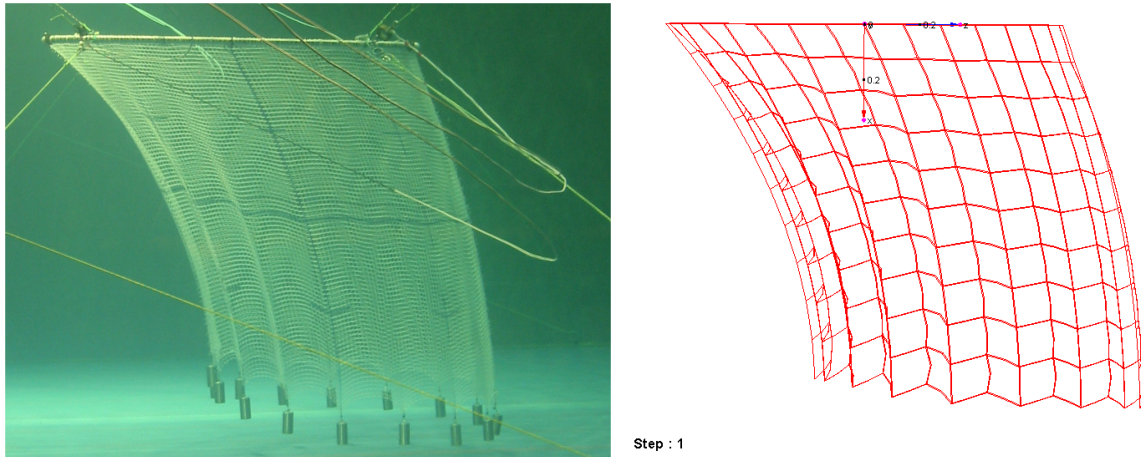


Figure 4.10: Picture of net cage during experiment (Enerhaug 2004) with a flow velocity of 0.33 [m/s] to the left and an illustration of the resulting geometry of the numerical analysis to the right. Colors indicate inflow velocity ([m/s]) on each element. Circumference 4.5 [m], depth 1.435 [m], solidity factor 0.225 and $EA = 8000$ [N] for the numerical model.

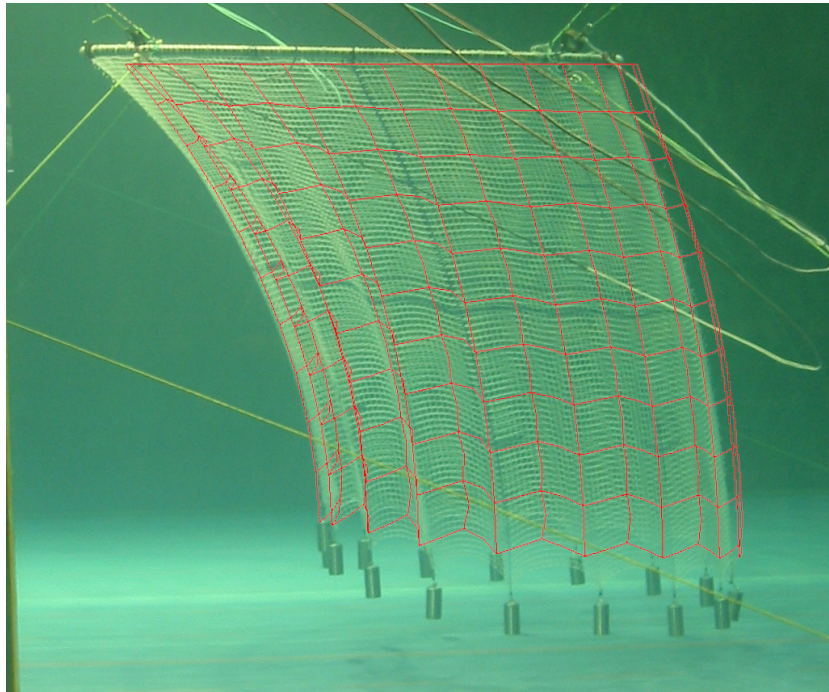


Figure 4.11: Picture of net cage during experiment (Enerhaug 2004) with a flow velocity of 0.33 [m/s] with an illustration of the resulting geometry of the numerical analysis imposed on top. Circumference 4.5 [m], depth 1.435 [m], solidity factor 0.225 and $EA = 8000$ [N] for the numerical model.

Table 4.4: Properties for the different section of the conical structure. Section 1 is the front and section 4 the aft of the cone.

Sec. no.	Diameter opening [m]	Length [m]	d_t [mm]	Cd_t	d_k [mm]	Cd_k	No. circum.	No. long.	EA [N]
1	0.704	1.0	16.1	1.2	22.5	2.0	40	10	27642
2	0.408	1.0	11.6	1.2	22.5	2.0	40	10	23295
3	0.260	0.5	13.5	1.2	22.5	2.0	20	5	38824
4	0.130	0.44	14.6	1.2	22.5	2.0	10	5	54043

4.4 Cone structures

Numerical calculations have been carried out for a cone of 2.94 [m] length, a circular front opening with a diameter of 1.0 [m] and an aft opening of 0.13 [m].

The cone was modeled, using diamond type of meshes, and divided into 4 sections with different parameters. The properties for the different section is presented in Tab. 4.4 and the model is illustrated in Figure 4.12. For each of the sections, the Solidity ratio was kept equal to 0.58 at the middle of the section by controlling the number of meshes, the size of the meshes and the diameter of the twines. Section number 1 is the section at the front of the cone, upstream towards the flow. The undisturbed current flow was equal to 1.0 at the front of the cone. Due to the change in diameter of the twines to keep the Solidity ratio constant, the Reynolds number is changing along the cone surface from $1.0 - 1.4 \times 10^3$. Since the solidity ratio is higher for the cone than for the plane net, a higher stiffness is chosen. Using Equation (4.2), the axial stiffness of the numerical model should be about 8.6 times higher than the elasticity of the real cone. Using an E -modulus of 150 [MPa], a twine diameter for the real cone of 1.3 [mm], then gives an EA for the model of 3544 [N]. An E -modulus of 1170 [MPa] will similarly give an EA of 27642 [N].

4.4.1 Structural analysis and end force

A trawl will normally consist of three main parts, the front part, middle part and the cod-end. The cod-end is the aft part of a trawl and is cylindrical in shape. The end of the cod-end is blocked with net and it is where the catch is collected. The catch will impose a large drag force and due to this has a large impact on the shape of the rest of the trawl, especially the cod-end and the middle part. A cone net structure without this horizontal force will obtain a different final geometry than a net cone without. This is illustrated in Figure 4.13.

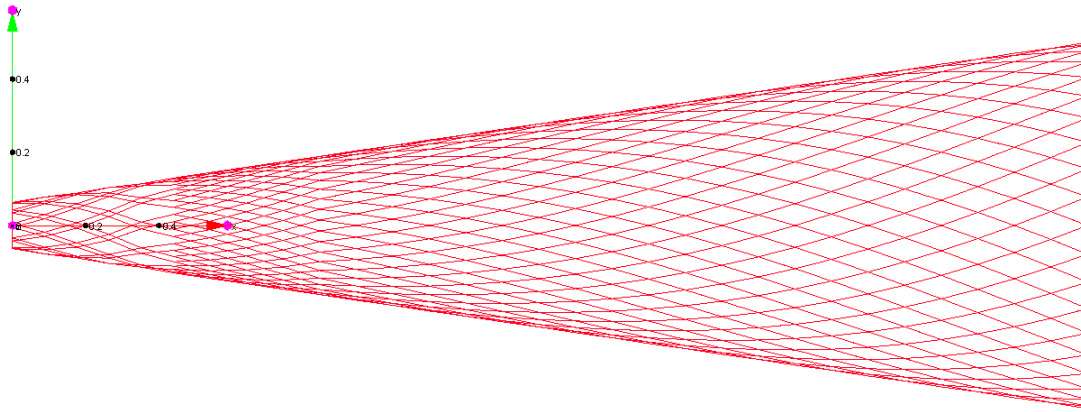


Figure 4.12: Illustration of the conical net structure used for numerical analysis.

When no horizontal force is applied at the aft, a three-dimensional elastic cone of net will obtain a balloon type of final shape as seen in the top figure. This is due to an outward force of the net, a lift force perpendicular to the uniform flow direction. The balloon shape is also slightly apparent when a horizontal force is applied, as can be seen as the part of the cone above the straight line in the lower figure. The effect of the lift force is in this case restrained by the horizontal force at the aft.

4.4.2 Drag force

Figure 4.14 presents total drag on a cone as described in Table 4.4 with five different cases for elasticity and flow correction. Again the results are presented as total drag force in lack of a proper dimension to use for creating non-dimensional values. For the case, “Fixed cone” no correction of the geometry due to the load is included, “Fixed. Downstream flow correction” includes a downstream flow correction, “Elastic” includes a change in the geometry but no flow correction due to the structure, “Elastic. Downstream flow correction” includes both a structural analysis and a downstream flow correction and finally “Elastic. Flow correction” includes a structural analysis and both an upstream and a downstream flow correction. Except for the case with only the fixed cone, an illustration of the resulting geometry is shown in Figure 4.15. The difference in results between the four cases is evidently small, with a maximum difference of only 3.2%. And the change is apparently mainly due to inclusion of flow correction, while a change in the shape of the structure, when a horizontal force is applied at the aft, do only to a small degree influence the total drag force.

The difference in result when both upstream and downstream correction is included, com-

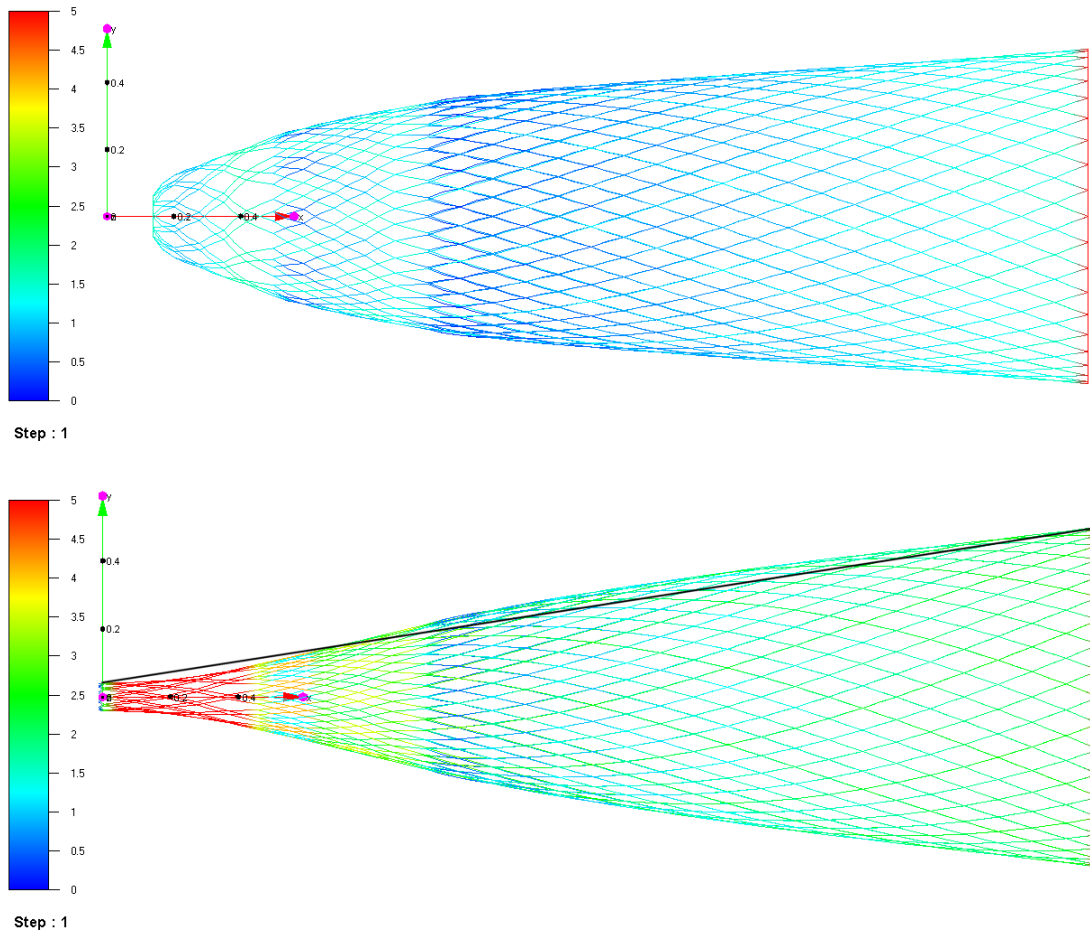


Figure 4.13: The geometry of the cone with no horizontal force at the aft (top) and with a 100 [N] horizontal force at the aft (bottom). Colors indicate tension ([N]) in individual elements. Constant $EA = 3.5 \times 10^5$ [N] along cone.

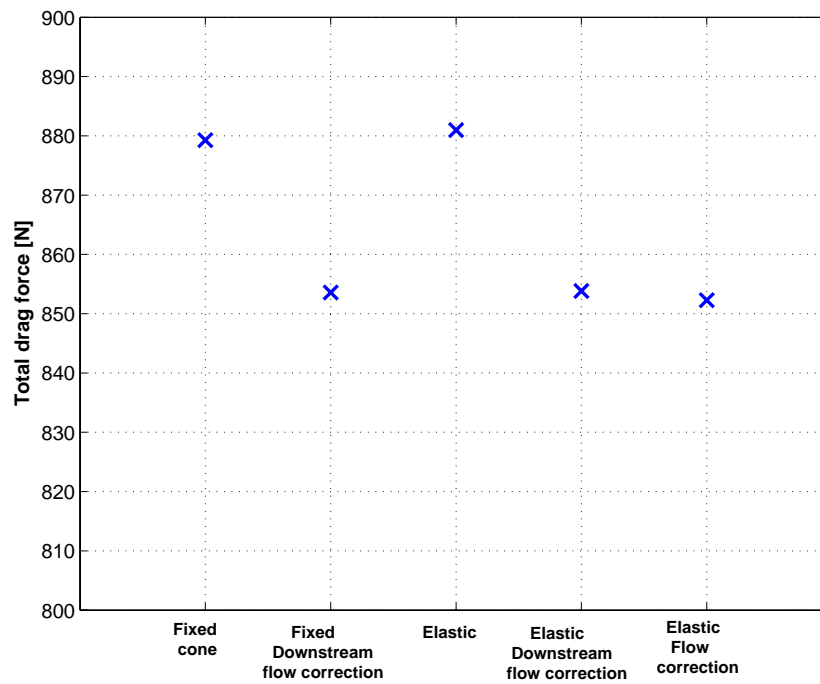


Figure 4.14: Total drag force of a cone with properties listed in Table 4.4 for different cases of analysis and with an horizontal force of 100 [N] at aft.

pared to only downstream is also neglect-able. Thus the model does not predict any changes in the upstream flow condition due to the net structure that has any impact on the total drag force. This is in contrast to the results for plane nets as discussed in Section 2.8, where an increase in the calculated drag force seen when upstream flow correction was included. It is no apparent that here is any changes in the inflow condition upstream that is of a magnitude that will be important with regard to the total drag force. Changes in the flow field due to the presence of net structure are further discussed in the next section.

4.4.3 Fluid velocity inside a three-dimensional net structure

As described in Section 1.1, one of the motivations for this work was to analyze the velocity field within a trawl or a three-dimensional net structure to be able to study the flow conditions inside a trawl or a three-dimensional net structure. In Figure 4.16 numerical results for the velocity along the center line of the cone, compared to experimental results by Enerhuag & Gjøsend (2001) and Enerhaug (2003), are presented. The results are presented as non-dimensional flow velocity in x-direction with respect to uniform flow U_∞ as a function of non-dimensional distance from the front of the cone with respect to the length of the cone L_{cone} . Uniform flow direction is from the right to the left in the figure, and the front of the cone is at $x/L_{cone} = 1.0$ and the aft at $x/L_{cone} = 0.0$. The experiments

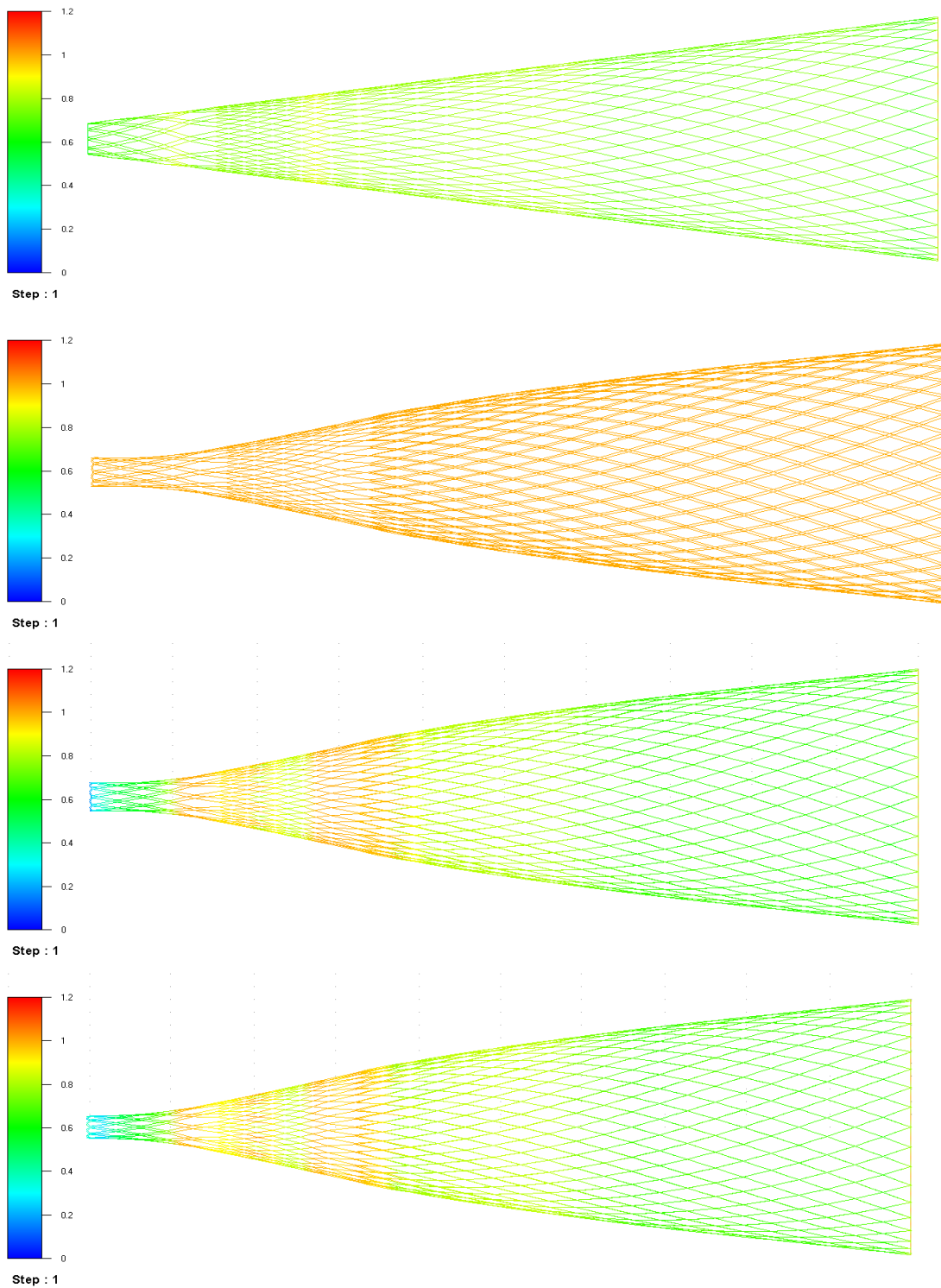


Figure 4.15: Illustration of results for different cases of numerical analysis. Stiff with downstream flow correction (top), elastic without wake correction, elastic with downstream flow correction and elastic with upstream and downstream flow correction (bottom). Colors indicate inflow velocity ([m/s]) on each element.

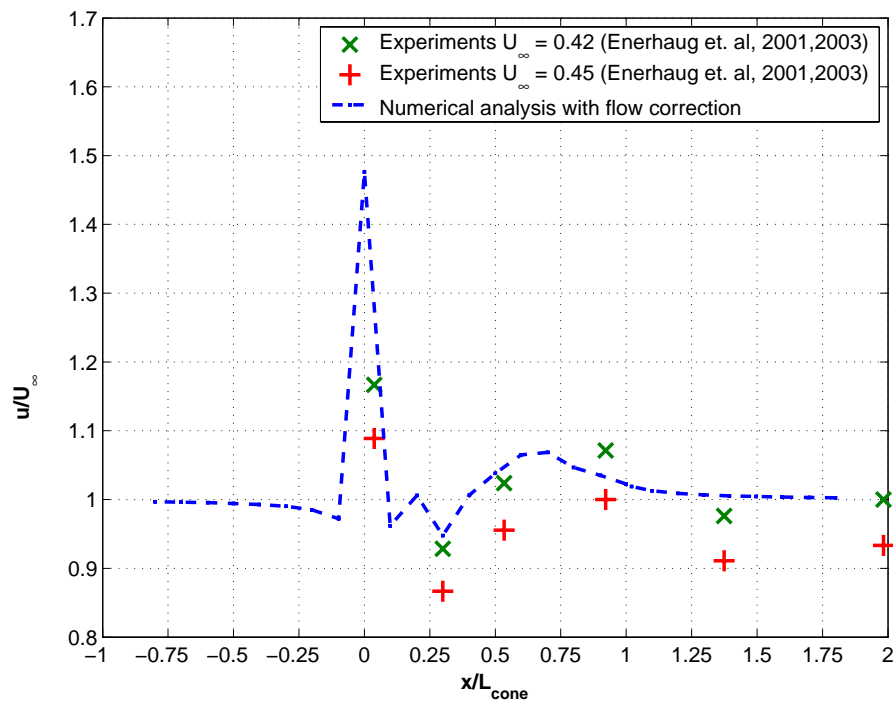


Figure 4.16: Non-dimensional velocity profile along center line of the cone, with respect to uniform flow from the right to the left of the figure. The numerical results are based on a cone with properties listed in Table 4.4. The aft end of the cone is situated at $x/L_{cone} = 0.0$ and the front part at $x/L_{cone} = 1.0$, where L_{cone} is the length of the cone.

are carried out with a cone with the same main dimensions as the one used for our numerical analysis and with a twine diameter, $d_t = 1.3 [mm]$ and a mesh size $l_m = 22.0 [mm]$. In the experiments, the Solidity ratio was kept constant along the cone at $Sn = 0.58$ by reducing number of meshes along the cone. In the numerical analysis the solidity ratio was kept constant, equal to 0.58, at the middle part of each section by changing the diameter of the twine and number of meshes for each section. Thus some variation of the solidity across one section will occur in the numerical model.

There are uncertainties related to which inflow velocity to use for the experimental results by Enerhuag & Gjørsund (2001) and Enerhuag (2003), thus the presentation of the experimental results with both an uniform velocity $U_{\infty} = 0.42 [m/s]$ and $U_{\infty} = 0.45 [m/s]$. Looking at the measurements in front of the cone, in what should be undisturbed water, there is a velocity profile ranging from $0.4 [m/s]$ at the bottom, up to $0.5 [m/s]$ close to the surface of the measurement tank. This of course could give rise to inaccuracy in the experimental results.

As seen in the figure, the agreement between the numerical and experimental results is

reasonably good. Quantitatively the results do not match exactly, but the characteristics of the flow are recreated. Some observations of the results:

- The asymptotic value of the upstream non-dimensional velocity for the numerical results are equal to 1.0. If it is assumed that U_∞ for the experiments is equal to 0.42 [m/s], then the non-dimensional velocity from the experiments at $x/L_{cone} = 2.0$, which corresponds to a position equal to the length of the cone upstream, is also equal to 1.0.
- There seem to be a slight increase in the flow velocity at the inlet of the cone. This is seen clearly in the numerical result and in the experimental results as an increase in the non-dimensional velocity between $x/L \approx 1.33$ and $x/L_{cone} \approx 0.9$.
- The numerical results show an increase in the velocity down to approximately $x/L_{cone} = 0.63$, when the velocity start to decrease and continue to decrease until $x/L_{cone} \approx 0.3$. For the experimental results there is an reduction in the velocity from $x/L_{cone} \approx 0.9$ to $x/L_{cone} \approx 0.5$ and further to $x/L_{cone} \approx 0.3$.
- There is a relatively large decrease in velocity at $x/L_{cone} \approx 0.3$ in the experimental results, which is also recreated by the numerical results.
- The increased outflow velocity at the aft of the cone noted in the experimental results is also evident in the numerical results. But the value from the numerical results is considerably higher.

For decreasing x/L_{cone} , the more narrow becomes the passage of the cone, thus a higher restriction of the flow is expected. If the cone was made of solid material, not as a mesh structure, it is expected that the flow velocity would increase, since the cross sectional area of the cone for the water to flow through becomes smaller. But due to the possibility of flow of water through the meshes, the resulting flow field becomes more complex, as seen from Figure 4.16.

The shape of the cone will influence the opening of the meshes at the different cross-sections along the cone. Similarly will differences in the Solidity ratio along the cone influence the opening of the meshes and the local geometry. For the numerical model the cone is modeled such that the Solidity ratio is constant at the middle of each of the four sections (see Table 4.4) and for the experimental model meshes are “taken off”, which will introduce local changes in flexibility and geometry, as well as small changes in Solidity ratio. This variation in Solidity ratio and geometry along the cone, can partly explain the variation in the flow velocity along the center line of the cone, when a local increase in Solidity ratio could contribute to an increasing flow resistance and thus a decrease or increase in flow velocity.

It is also difficult to quantify the exact resulting shape and geometry of the experimental cone. The shape will change as a function of the loads on the cone. This is also shown by numerical analysis and is illustrated in Figure 4.13. In the experiments a horizontal force is applied at the aft of the cone to counteract the effect that the net structure will contract lengthwise.

At the outlet of the cone it is expected a distinct increase in flow velocity, due to a larger inlet than outlet. This is also seen in both the experimental and numerical results and is likely to be due to the conservation of momentum. But from a conservation of momentum perspective it is difficult to explain the increase in flow velocity at the inlet. It is assumed that a cone net structure, due to the resistance of the twines and knots, partly will have an effect as a bucket exposed to flow, but then it would be expected that the flow velocity at the inlet should be decreased. Enerhuag & Gjørund (2001) argues that the increased flow at the outlet can be caused by a low pressure behind the cone due to vortices shed from an attachment ring and the front of the cone and an increased flow velocity outside and behind the cone. This effect will not be captured by the present numerical model.

4.4.4 Pressure field in front of a three-dimensional net structure

Another motivation for this work was to be able to study the pressure field in front of the trawl. In Figure 4.17 a contour plot of the calculated relative pressure gradients in front of the cone is shown. As seen from the figure, the change in pressure is limited and it is not apparent if this change is large enough for the fish to sense. By compare this pressure difference due to the change in velocity to a vertical change in position of a fish in the water column, an understanding of the magnitude and influence of the pressure difference might be obtained. Say $\rho g \delta h = \delta p_{velocity}$, where δh is the vertical change in position and $\delta p_{velocity}$ is the change in pressure due to the change in velocity field. Then the maximum change in pressure corresponds to a vertical change in position of $\delta h = 1.83[mm]$. A normal sized fish could have a length of 50 - 100 [cm] and a height of 10 - 0 [cm]. Then the calculated comparable vertical change in position corresponds to two orders of magnitude less than the height of the fish. Thus it seems not likely that the fish is able to detect such a small change in vertical position, and thus are not able to feel the presence of the net structure due to changes in velocity in front of the trawl.

Another interesting aspect is the possibility of the fish to hear the sound of the fishing gear. To get an idea of the possibility of this, the properties of a human ear might be used as a reference. The human ear is able to detect changes in pressure as low as 2.0×10^{-5} [Pa], while the upper limit of comfort is 200 [Pa]. Thus an ear has a wide range of pressure sensing capability. But for an ear to sense a pressure difference, the pressure has to vibrate at a certain frequency range. A human ear can sense vibrations between 20 and 20 000 [Hz]. At what frequencies the ear of a fish is working is unclear and at the same time is

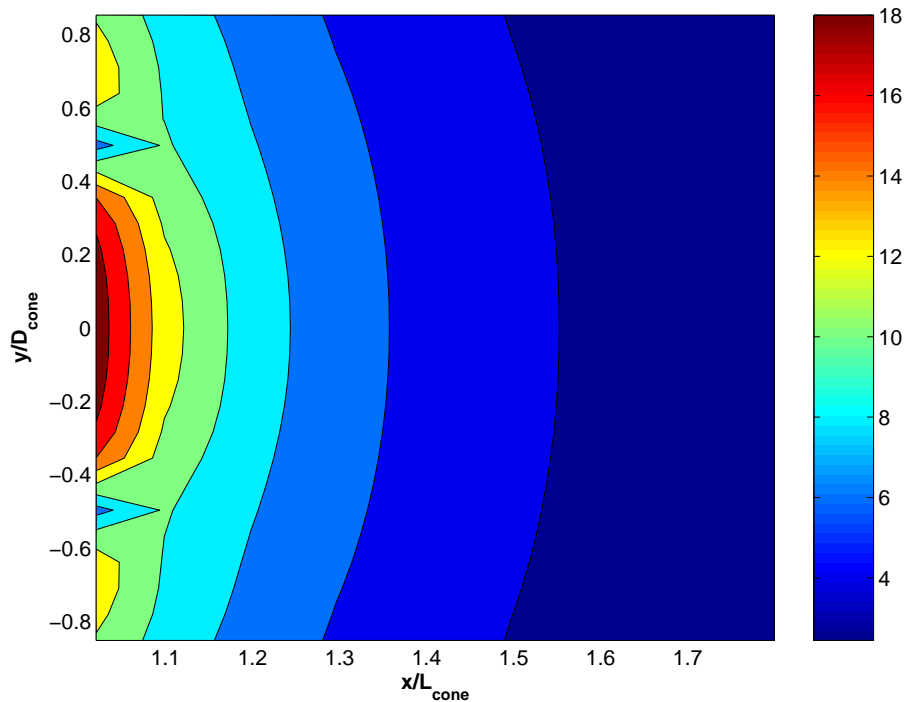


Figure 4.17: Relative pressure gradients in front of the cone, due to the calculated change in velocity caused by the cone. The numerical results are based on the cone with properties listed in Table 4.4. D_{cone} is the diameter of the front opening of the cone.

it not evident that the pressure field in front of a trawl due to the presence of a trawl is vibrating. The numerical model only predicts a steady state situation, thus no vibration is present and no sound is generated in the numerical result. There will be vortices shed from parts of trawl, like the gear, warp lines and also possibly from the twines. A Strouhal number, St , of 0.2 and a diameter of a member of the trawl of 1 [cm], will give a shedding frequency of 20 [Hz] with a towing speed of 1 [m/s]. Thus it is likely that there could be shed vortices from the trawl that are in the hearing range of a fish ear. But it is not likely that the generated energy due to these small vortices are large enough for the sound to travel ahead of the trawl at that speed.

Thus the final conclusion is that it is not likely that the fish will sense the trawl due to the effect the trawl has on the flow field. Kim & Wardle (2003) also state that it is likely that the most important method for the fish to sense a trawl is to detect it by visual means.

4.4.5 Other aspects related to net structures

The shape of the trawl and parts of the trawl is an important factor related to fishing efficiency and the selectivity performance of the trawl (Kim & Wardle 2003). Thus the investigated lift effect on cylinders in staggered arrangement in Section 3.5 could become an important aspect when modeling a trawl. A net structure is highly flexible with low structural damping. In addition to the uncertainties related to the previously discussed issues, there is a clear possibility of hydro-elastic effects related to fluttering or galloping. Blevins (1990) pointed out that large amplitude galloping motion can occur for a cylinder in the wake of another cylinder. This is associated with both the negative mean lift as well as the effect of the wake on the drag on the downstream cylinder. The possibility of galloping could be due to the non-circular shape of the twines and knots or that one twine could be situated in the wake of another twine. The relevance of this for a net structure has to be clarified.

It is expected that the effect on the twines in a real trawl is not that great, due to the nature of how the twine is constructed, such that the separation point will be triggered by the uneven arrangement of the strains. At the same time both vibration of the twines and part of the net, as well as geometrical effects in the middle section of the trawl, is known to be important factors for fishing efficiency and how the trawl behaves when towed. In addition, it is possible that the problem should be investigated as a large scale net structure problem, rather than as a possible small scale, single element phenomena.

CHAPTER 5

Conclusions and Further work

The complexity of the flow around a fishing net or trawl, makes CFD calculations presently impossible. Simple physically based load models are needed. Our focus has been on the flow around the twine elements of the fishing net, when a twine element is in the wake of another element.

An examination of numerical results for the drag force on plane net structure demonstrates a strong dependency of the drag force on a net structure with both the geometry, in terms of Solidity ratio, and the Reynolds number. And in particular a non-uniform relation between the drag force and the Solidity ratio. The dependency is partly due to the change in the drag coefficient for the individual elements which make up a net structure, such as the twine and the knot. Further it is evident that for increasing Solidity ratios, flow interaction will become increasingly significant. The physical design of the knot part contributes largely to this flow interaction, and has an increasing importance as the Solidity ratio increases and the relative area of the knot part compared to the total projected area of the net increases.

A method has been presented to calculate the drag force on net structures with high solidity. The method uses appropriate drag coefficients related to the geometry of the twines and the knots and account for the change in the inflow due to the presence of the net structure and at the same time changes the geometry of the net structure due to the load. The near-field wake model of the mean flow by Blevins (1990) can be used to calculate the drag force on a downstream cylinder. The results has been validated by experiments at Reynolds numbers from 2.0×10^4 to 6.0×10^4 . The drag force on the downstream cylinder is

sensitive to the turbulence intensity of the incident flow. However this is a minor problem for the Reynolds number range of practical interest, $1.0 - 5.0 \times 10^3$. Further, the method has been verified against experiments, as means of calculating the drag on plane nets as a function of Reynolds number, Solidity ratio and angle of attack and gives reasonable good agreement.

The downstream cylinder can in certain staggered arrangements experience a significant mean negative lift force, acting towards the mean wake axis. This has been explained by experiments and simple theory as interaction between vortices shed from the upstream cylinder and the flow around the downstream cylinder.

Results for three-dimensional net structures, such as net panels with elasticity, net cages and cone structure, show that the elasticity of the net structure has a direct influence on the geometry of the net structure when exposed to external force and will thus have an effect on the experienced drag force. The difficulty in accurate modeling of axial stiffness of the twines, due to both model reduction and the physical properties of the twine, has been described and illustrated with numerical results.

The numerical results for net cages have been compared to experimental results. In the numerical analysis, the downstream effects and change in geometry were included, but not the upstream effects. Good agreement between the numerical results and the experimental result has been shown. Also the resulting geometry from the experimental results was recreated satisfactory using the presented method. Further, the results illustrate the importance of both including a structural model with elasticity and a correction for downstream flow effects. Any flow through a net with a certain solidity ratio will be reduced in magnitude and a net downstream of another net will then encounter a flow of less velocity.

For three-dimensional cone shaped net structures, in contrast to net panels and net cages, the presented numerical results do not indicate a large influence on the drag force due to different flow models or changes in geometry. The largest effect is seen when a model of the downstream flow effect is included, while an upstream correction in this case do not have any significant influence. The influence and significance of the different corrections will off course be a function of the physical properties and shape of the cone structure.

Agreement between numerical and experimental results for fluid velocity in front and inside of a three-dimensional net structure, compared to experimental results, has been shown to be reasonably good. Quantitatively the results do not match exactly, but the characteristics of the flow are recreated.

Based on the numerical results for fluid velocity, pressure field in front of a cone is presented. The relative pressure gradient is shown to be small, and it is not likely than any fish will detect this change in pressure filed either by direct pressure sensing or by any sound created due to shed vortices.

The shape of the trawl and parts of the trawl is an important factor related to fishing efficiency and the selectivity performance of the trawl. A net structure is highly flexible with low structural damping and there is a clear possibility of hydro-elastic effects related to fluttering or galloping. The relevance of this for a net structure should be clarified. In addition, it is possible that the problem should be investigated as a large scale net structure problem, rather than as a possible small scale, single element phenomena.

To further understand the drag force dependency of the Solidity ratio and Reynolds number and to be able to calculate it in an improved manner, it is necessary to understand the physics of the flow around the knot part of the net. Thus further investigation and experimental studies should be carried out, to get a better insight of the flow in the vicinity and around the knot part of the net.

Bibliography

- Aarsnes, J. V., Løland, G. & Rudi, H. (1990), Current forces on cages, net deflection, *in* ‘Engineering for fish farming’, Glasgow, United Kingdom.
- Aarsnes, J. V. & Rudi, H. (1989*a*), Notdrag - theory manual, Technical Report MT40 F89-0137, MARINTEK.
- Aarsnes, J. V. & Rudi, H. (1989*b*), Notdrag - user manual, Technical Report MT40 F89-0138, MARINTEK.
- Bessonneau, J. S. & Marichal, D. (1998), ‘Study of the dynamics of submerged supple nets (application to trawls)’, *Journal of Ocean Engineering* **7**, 563–583.
- Blevins, R. D. (1990), *Flow-Induced Vibration*, Van Nostrand Reinhold.
- COMSOL (2000), *FEMLAB 2.0 Reference Manual*, COMSOL AB, SWEDEN.
- Dret, H. L., Priour, D. & Chagneau, F. (2004), ‘Numerical simulation of a cod end net. part 1: Equilibrium in a uniform flow (in press)’, *Journal of Elasticity* .
- Enerhaug, B. (2003), Current flow through and around conical structures, Technical Report STF80 A033035, SINTEF Fisheries and Aquaculture. (In Norwegian).
- Enerhaug, B. (2004), Model tests of net structures, SINTEF Report STF80 A034007, SINTEF Fisheries and Aquaculture.
- Enerhaug, B. & Gjørund, S. H. (2001), Experimental, numerical and analytical studies of flow through reticulate and solid cones, *in* ‘Methods for the Development and Evaluation of Maritime Technologies’, University of Rostock, Germany.
- Fridman, A. L. (1992), *Calculations for fishing gear design*, Fishing News Books Ltd.

- Herfjord, K., Holmås, T., Leira, B., Bryndum, M. & Hanson, T. (2002), Computation of interaction between deepwater risers. collision statistics and stress analysis, OMAE, Oslo, Norway.
- Hoerner, S. F. (1965), *Fluid-dynamic Drag*, Hoerner Fluid Dynamics.
- Huse, E. (1992), Current forces on individual elements of riser arrays, in 'Proceedings of the Second International Offshore and Polar engineering Conference'.
- Kim, Y.-H. & Wardle, C. S. (2003), 'Optomotor response and erratic response: quantitative analysis of fish reaction to towed fishing gears', *Fisheries Research* **60**, 455–470.
- Koo, J.-K. & James, D. F. (1973), 'Fluid flow around and through a screen', *Journal of Fluid Mechanics* **60**, 515–538.
- Koritzky, H. H. (1974), Beitrag zur Bestimmung von Widerstand und Auftrieb ebener Netztücher, PhD thesis, University of Rostock, Rostock, Germany. (In German).
- Kreyszig, E. (1993), *Advanced Engineering Mathematics*, 7th edn, John Wiley & Sons, Inc.
- Lader, P. F., Enerhaug, B., Fredheim, A. & Krokstad, J. R. (2003), A full 3d model of net structures exposed to waves and current, in 'The 3rd International Conference on Hydroelasticity in Marine Technology', Oxford, UK.
- Løland, G. (1991), Current forces on and flow through fish farms, PhD thesis, Dept. of Marine Hydrodynamics, Norwegian Institute of Technology.
- Maniar, H. (1995), A three dimensional higher order panel method based on B-splines, PhD thesis, The Massachusetts Institute of Technology.
- Milne, P. H. (1970), 'Fish farming: A guide to the design and construction of net enclosures', *Department of Agriculture and fisheries for Scotland, Marine Research* **1**.
- Milne-Thomson, L. M. (1968), *Theoretical Hydrodynamics*, MacMillian & Co. Ltd.
- Newman, J. N. (1977), *Marine Hydrodynamics*, MIT Press.
- Niedzwiedz, G. (2001), Model specification and further applications of the calculation of rope systems, in 'Proc. of the 5th International Workshop "DEMaT 01"', Rostock, Germany.
- Okajima, A. (1979), 'Flows around two tandem cylinders at very high reynolds numbers', *Bulletin of the ISME* **22**(166).
- O'Neill, F. G. (1997), 'Differential equation governing the geometry of a diamond mesh cod-end of a trawl net', *Journal of Applied Mechanics* **64**, 7–14.

- O'Neill, F. G. & O'Donoghue, T. (1997), The fluid dynamic loading on catch and the geometry of trawl cod-ends, *in* 'Proc. of The Royal Society London Annual', Vol. 453, pp. 1631–1648.
- Paschen, M. & Winkel, H.-J. (1999), Flow investigations of net cones, *in* 'Proc. of the 4th International Workshop "DEMaT 99"', Rostock, Germany.
- Pfeil, H. & Eifler, J. (1975), 'Messungen im turbulenten nachlauf des einzelzylinders', *Forshung im Ingenieurwesen* **41**(5), 137–138.
- Price, S. J. & Paidoussis, M. P. (1984), 'The aerodynamic forces acting on groups of two and three circular cylinders when subject to cross-flow', *Wind Eng. and Ind. Aerodyn.* (17), 329–347.
- Prior, D. (1998), Estimation of net mesh opening in the cod - end by using a numerical model, *in* 'Fishing Technology and Fish Behavior Working Group', International Council for the Exploration of the Sea, La Goruna, Spain.
- Rogers, D. F. & Adams, J. A. (1990), *Mathematical Elements for Computer Graphics*, 2nd edn, McGraw-Hill.
- Rudi, H., Løland, G. & Furunes, I. (1988), Experiemnts with nets; forces on and flow trough net panels and cage systems, Technical Report MT 51 F88-0215, MARINTEK, Trondheim, Norway. (In Norwegian).
- Sarpkaya, T. (1979), A discrete-vortex analysis of flow about stationary and transversely oscillating circular cylinders, Technical report, Naval postgraduate school, Monterey California.
- Schlichting, H. (1968), *Boundary-Layer Theory*, McGraw-Hill.
- Slaattelid, O. H. (1993), Materialdata og egenskaper for notlin og tau (in norwegian), Technical Report MT40 F93-0021, MARINTEK, Trondheim, Norway.
- Sumer, B. M. & Fredsøe, J. (1997), *Hydrodynamics Around Cylindrical Structures*, World Scientific.
- Taylor, G. I. (1944), 'Air resistance of a flat plate of very porous material', *Aeronautical Research Council Reports and Memoranda* (2236).
- Taylor, G. I. & Davies, R. M. (1944), 'The aerodynamics of porous sheets', *Aeronautical Research Council Reports and Memoranda* (2237).
- Theret, F. (1994), A mathematical model for the determination of the shape and tension of a trawl placed in a uniform current, *in* 'Fish Capture Committee', International Council for the Exploration of the Sea.

- Treshchev, A. I. (1974), *Nauchnue osnovi selektivnogo rybolovstva (Scientific principles of selective fishing)*, Pishchepromizdat, Moscow.
- Tronstad, H. (2000), Nonlinear hydroelastic analysis and design of cable net structures like fishing gear based on the finite element method, PhD thesis, The Norwegian University of Science and Technology, Trondheim, Norway.
- Vincent, B. (1999), A new generation of tools for trawls- dynamic numerical simulation, *in* 'Proc. of the 4th International Workshop DEMaT'99', DEMaT '99, Rostock, Germany.
- Vincent, B. & Marichal, D. (1996), Computation of the flow in the codend, *in* 'Fishing Technology and Fish Behavior Working Group', International Council for the Exploration of the Sea.
- Winkel, H.-J. & Paschen, M. (2001), Wind tunnel test for fishing gear development - methods and limits, *in* 'Proc. of the 5th International Workshop "DEMaT 01"', Rostock, Germany.
- Zdravkovich, M. M. (1985), Forces on pipe clusters, *in* 'Proc. Conf. Sep. Flow around Marine Structures.', Norwegian Institute of Technology, Trondheim.
- Zdravkovich, M. M. (1997), *Flow around circular cylinders*, Vol. 1, Oxford Sc. Pub.

APPENDIX A

Additional results from wake experiments

The results are presented as non-dimensionalized force coefficients, here denoted grid force coefficients by dividing the forces by $1/2\rho dhU^2N$, where ρ is the water density, d is the cylinder diameter, h is the submerged height of the cylinder, N is number of cylinders and U the towing speed. The drag force is the force in the towing direction and the lift force is perpendicular to it. All presented results are averaged values from several runs.

In addition to the figures, the averaged results are presented in different tables one for each spacing s . Within each table the results are sorted after angle to the inflow and velocity.

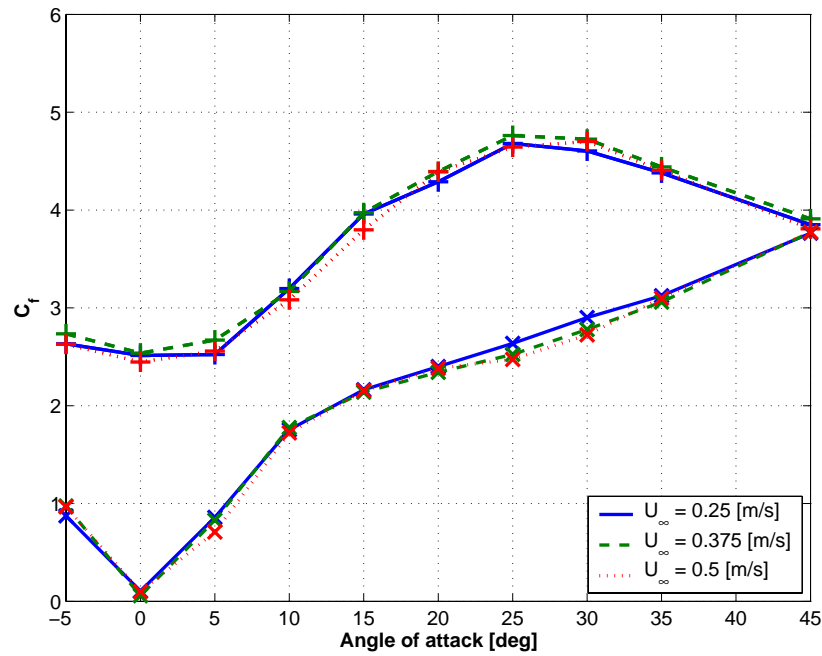


Figure A.1: Force coefficients from the experiments in inline (+) and perpendicular (x) direction as a function of angle of attack, α at different velocities. Five cylinders in a row with spacing $s = 5d$.

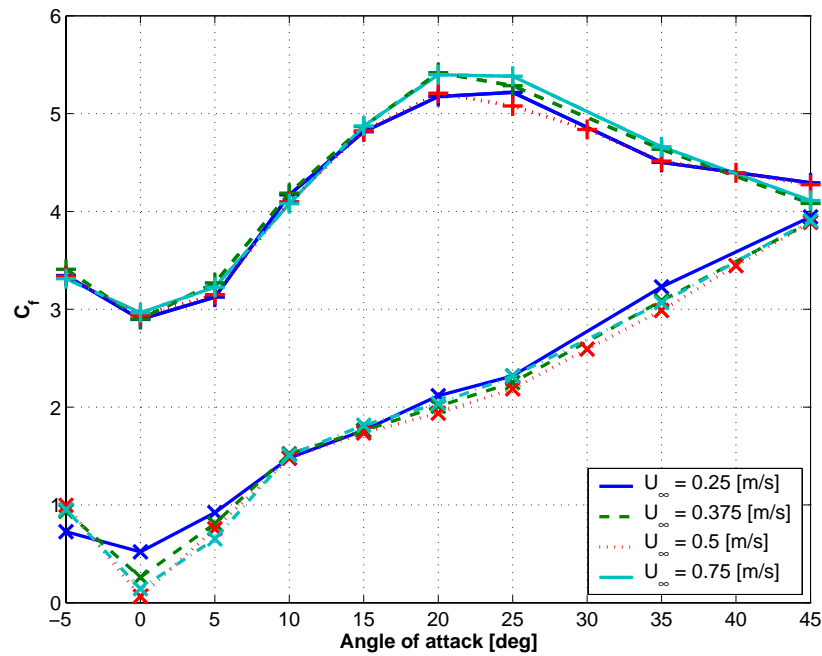


Figure A.2: Force coefficients from the experiments in inline (+) and perpendicular (x) direction as a function of angle of attack, α at different velocities. Five cylinders in a row with spacing $s = 7.5d$.

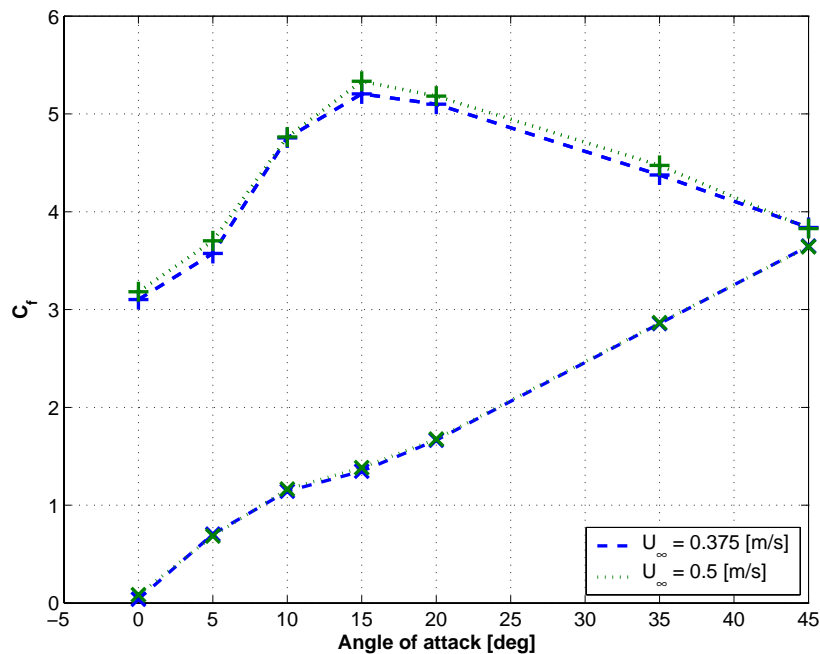


Figure A.3: Force coefficients from the experiments in inline (+) and perpendicular (\times) direction as a function of angle of attack, α at different velocities. Five cylinders in a row with spacing $s = 10d$.

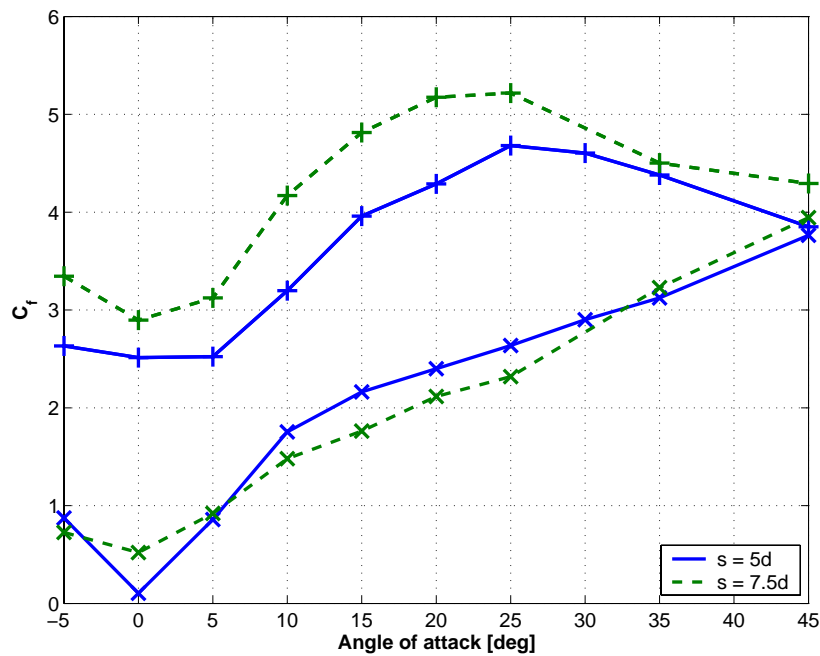


Figure A.4: Force coefficients from the experiments in inline (+) and perpendicular (\times) direction as a function of angle of attack, α at different spacings, s . Five cylinders in a row with $U_\infty = 0.25$ [m/s].

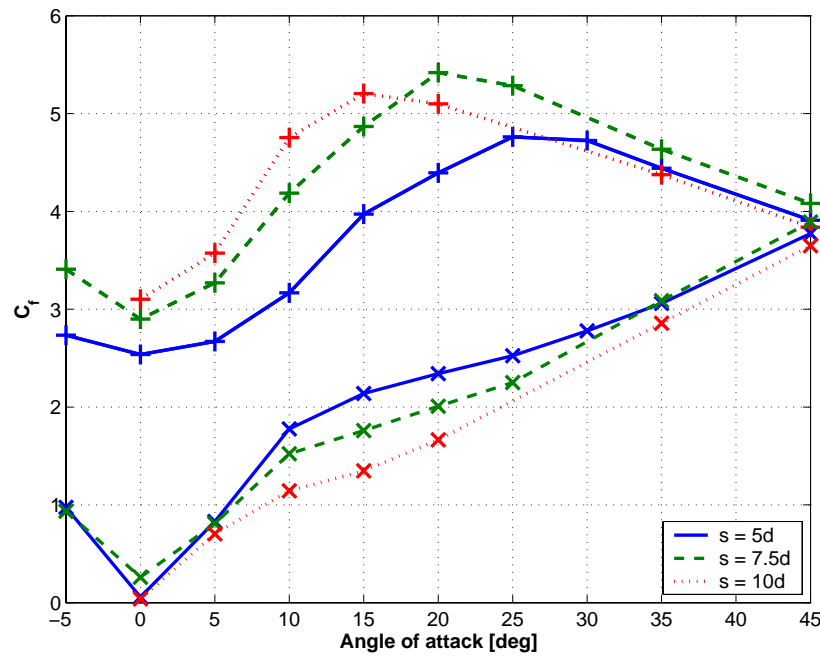


Figure A.5: Force coefficients from the experiments in inline (+) and perpendicular (x) direction as a function of angle of attack, α at different spacings, s . Five cylinders in a row with with $U_\infty = 0.375$ [m/s].

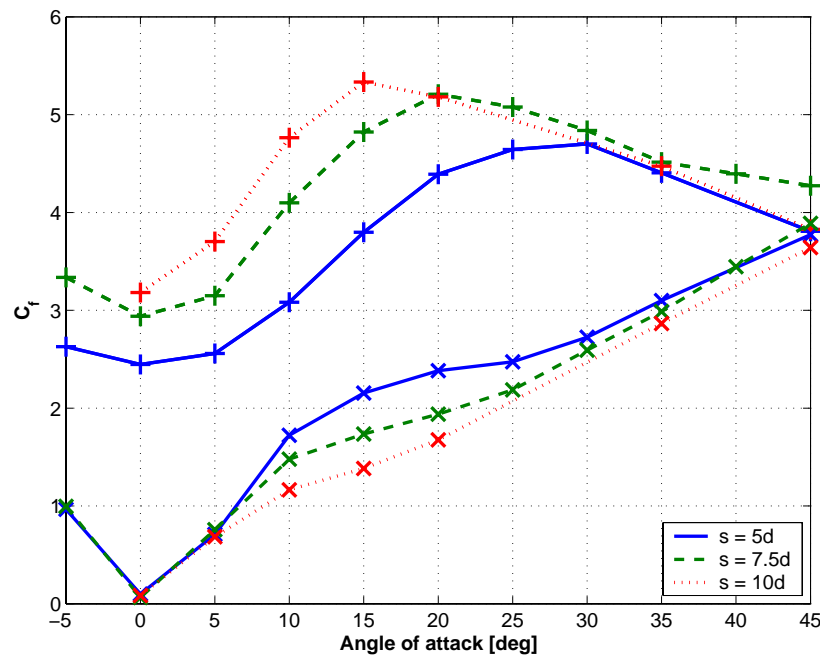


Figure A.6: Force coefficients from the experiments in inline (+) and perpendicular (x) direction as a function of angle of attack, α at different spacings, s . Five cylinders in a row with with $U_\infty = 0.5$ [m/s].

Table A.1: Average grid force coefficient from experiments, $\lambda = 5D$

Angle [deg]	Velocity [m/s]	Inline	Perpendicular	Drag	Lift
-5	0.25	2.632	0.873	2.698	1.099
	0.375	2.735	0.974	2.766	1.208
	0.5	2.628	0.966	2.702	1.191
0	0.25	2.513	0.104	2.513	0.104
	0.375	2.537	0.057	2.537	0.057
	0.5	2.446	0.098	2.446	0.098
5	0.25	2.523	0.858	2.589	1.075
	0.375	2.670	0.830	2.732	1.060
	0.5	2.558	0.709	2.610	0.929
10	0.25	3.198	1.754	3.454	2.283
	0.375	3.167	1.776	3.427	2.299
	0.5	3.082	1.722	3.334	2.231
15	0.25	3.961	2.162	4.385	3.114
	0.375	3.972	2.138	4.390	3.093
	0.5	3.798	2.154	4.227	3.064
20	0.25	4.288	2.400	4.851	3.721
	0.375	4.394	2.342	4.930	3.703
	0.5	4.391	2.382	4.941	3.740
25	0.25	4.681	2.636	5.356	4.367
	0.375	4.761	2.524	5.381	4.300
	0.5	4.644	2.473	5.254	4.204
30	0.25	4.604	2.901	5.438	4.814
	0.375	4.725	2.778	5.481	4.769
	0.5	4.700	2.724	5.432	4.709
35	0.25	4.379	3.124	5.379	5.071
	0.375	4.441	3.060	5.393	5.053
	0.5	4.405	3.099	5.385	5.065
45	0.25	3.850	3.763	5.383	5.383
	0.375	3.910	3.773	5.433	5.433
	0.5	3.808	3.774	5.362	5.362
90	0.25	0.091	5.521	5.521	0.091
	0.375	0.139	5.738	5.738	0.139

Table A.2: Average grid force coefficient from experiments, $\lambda = 7.5D$

Angle [deg]	Velocity [m/s]	Inline	Perpendicular	Drag	Lift
-5	0.375	3.409	0.935	3.477	1.229
	0.25	3.345	0.726	3.395	1.015
	0.5	3.336	0.996	3.411	1.283
	0.75	3.312	0.952	3.383	1.237
0	0.25	2.896	0.520	2.896	0.520
	0.375	2.899	0.260	2.899	0.260
	0.5	2.939	0.065	2.939	0.65
	0.75	2.964	0.143	2.964	0.143
5	0.25	3.123	0.920	3.191	1.189
	0.375	3.269	0.810	3.327	1.092
	0.5	3.149	0.757	3.203	1.029
	0.75	3.226	0.652	3.271	0.930
10	0.25	4.170	1.480	4.364	2.181
	0.375	4.186	1.522	4.387	2.226
	0.5	4.099	1.479	4.294	2.168
	0.75	4.079	1.508	4.279	2.194
15	0.25	4.814	1.762	5.106	2.948
	0.375	4.868	1.760	5.158	2.960
	0.5	4.822	1.735	5.106	2.923
	0.75	4.874	1.815	5.178	3.014
20	0.25	5.174	2.115	5.306	3.757
	0.375	5.419	2.008	5.490	3.741
	0.5	5.209	1.938	5.558	3.603
	0.75	5.398	2.036	5.480	3.759
25	0.25	5.217	2.319	5.423	4.307
	0.375	5.286	2.251	5.455	4.274
	0.5	5.078	2.186	5.526	4.127
	0.75	5.382	2.317	5.565	4.375
30	0.5	4.838	2.592	5.486	4.664
35	0.25	4.502	3.228	5.262	5.226
	0.375	4.635	3.087	5.289	5.187
	0.5	4.515	2.987	5.412	5.036
	0.75	4.661	3.067	5.298	5.186
40	0.5	4.395	3.445	5.581	5.464
45	0.25	4.293	3.944	5.533	5.825
	0.375	4.082	3.892	5.356	5.638
	0.5	4.273	3.889	5.772	5.772
	0.75	4.112	3.906	5.386	5.670
90	0.25	0.186	5.620	5.339	0.186
	0.375	0.151	6.003	5.703	0.151
	0.5	0.800	6.535	6.535	0.800
	0.75	0.234	6.255	5.942	0.234

Table A.3: Average grid force coefficient from experiments, $\lambda = 10D$

Angle [deg]	Velocity [m/s]	Inline	Perpendicular	Drag	Lift
0	0.375	3.102	0.039	3.102	0.039
	0.5	3.181	0.085	3.181	0.085
5	0.375	3.574	0.703	3.621	1.012
	0.5	3.702	0.685	3.748	1.005
10	0.375	4.754	1.144	4.881	1.952
	0.5	4.764	1.165	4.894	1.975
15	0.375	5.205	1.348	5.377	2.650
	0.5	5.333	1.383	5.509	2.716
20	0.375	5.099	1.665	5.361	3.309
	0.5	5.182	1.675	5.442	3.346
35	0.375	4.375	2.857	5.222	4.849
	0.5	4.474	2.865	5.308	4.913
45	0.375	3.839	3.649	5.294	5.294
	0.5	3.827	3.642	5.282	5.282
90	0.375	0.157	5.830	5.830	0.157
	0.5	0.138	5.925	5.925	0.138

Table A.4: Average grid force coefficient from experiments, $\lambda = 20D$

Angle [deg]	Velocity [m/s]	Inline	Perpendicular	Drag	Lift
0	0.375	2.568	0.013	2.568	0.013
0	0.375	2.502	0.059	2.502	0.059
5	0.375	2.879	0.308	2.895	0.557
5	0.375	2.792	0.277	2.805	0.519
10	0.375	3.241	0.543	3.286	1.098
10	0.375	3.215	0.495	3.252	1.046
15	0.375	3.151	0.766	3.242	1.556
15	0.375	3.222	0.742	3.304	1.551
20	0.375	3.119	1.045	3.288	2.048
20	0.375	3.266	1.047	3.428	2.101
45	0.375	2.497	2.361	3.435	3.435

APPENDIX B

Description of North Sea Centre Flume Tank

The North Sea Centre Flume Tank in Hirtshals, Denmark is the second largest flume tank in the world and is filled with fresh water.

Dimensions

Length:	30 [m]	Height:	6 [m]	Width:	8 [m]
Measuring section:	21.3 x 2.7 x 8 [m]				
Volume of water:	1200 m ³ .				
Windows:	L: 20 m	H:	3 m		

Propulsion and velocity

Four propellers and motors of 64 KW generate the flow.

Maximum water speed:	1 m/s
Maximum simulated towing speed in scale	1:5:4,5 knots
Maximum simulated towing speed in scale	1:20:12 knots

Artificial bottom

Conveyer belt type made of nylon. Speed adjustable, can be locked with water speed.



Figure B.1: The North Sea Centre Flume Tank.

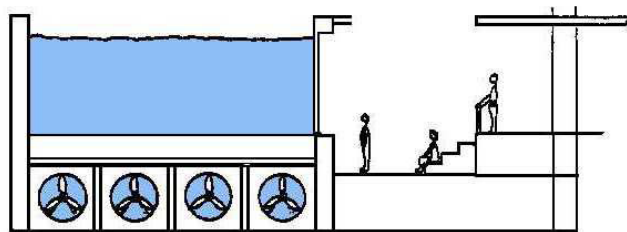
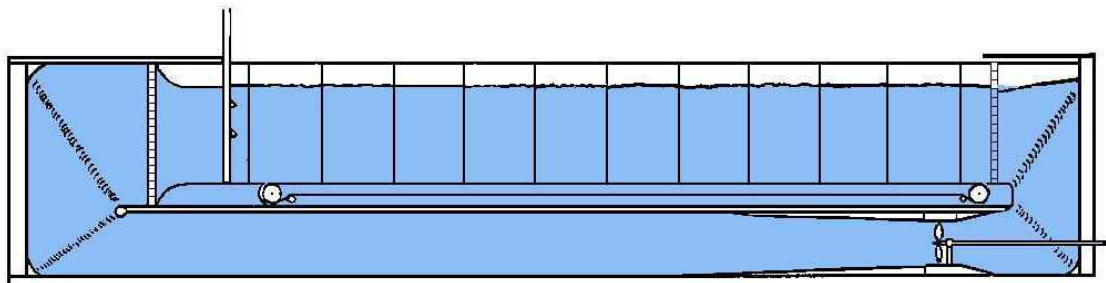


Figure B.2: Sketch of The North Sea Centre Flume Tank.